Development of a 3D *in vitro* model of cancer progression

Tarig Magdeldin

Submitted in partial fulfillment of the requirements for the degree of Doctor of Philosophy

Division of Surgery and Interventional Science
University College London

April 2016

I, Tarig Magdeldin, confirm that the work presented in this thesis is my own.

Where information has been derived from other sources, I confirm that this has been indicated in the thesis.

Signed ……

Acknowledgements

I would like to express my most sincere gratitude to my supervisors, Dr. Umber Cheema and Professor Marilena Loizidou for their endless support, guidance and friendship over the duration of this work. You were always there to offer words of encouragement and a little dose of optimism when I needed it most. Your stimulating suggestions have always taught me to think outside the box and for that I am eternally thankful.

I am grateful to TAP Biosystems for their financial contributions to this project, which without this research would not have been possible. I would also like to thank Dr. Rosemary Drake, Dr. Grant Cameron and Dr. Cécile Villemant for their overwhelming support and thoughtful discussions from the outset of my PhD and throughout.

I would also like to thank all of my friends and colleagues at the Institute of Orthopeadics and the Royal Free Hospital for their support, expertise and friendship, Ms. Rebecca Porter, Ms. Claire Walsh, Dr. Katerina Stamati, Dr. Noah Tan, Dr. Hazel Welch, Dr. Kate Ricketts, Dr. Bala Ramesh and Ms. Stephanie Bogan. A special thanks to Dr. Víctor López-Dávila who taught me the importance of laughter and sanity when it seemed all hope was lost.

I owe a great deal of thanks to Cheryl Teoh, whom without this thesis would not have been possible. You always believed in me and helped me realize the best in my abilities. Thank you for your kindness, support, patience and care.

Most of all, I would like to thank my family for the endless love, support and motivation through this journey. Your confidence and belief in me is the main reason for all of my achievements. Your sacrifices have brought me to this point and this PhD belongs to you as much as it does to me. Thank you for everything.

Abstract

The hallmark of cancer is the ability of cancer cells to disseminate and invade to distant organs. Metastasis accounts for over 90% of cancer related deaths and therefore requires a better understanding of the metastatic cascade to develop better therapeutic regimens. The metastatic process is heavily influenced by the extracellular matrix (ECM) density and composition of the surrounding tumour microenvironment. These microenvironmental cues also regulate the angiogenic processes within a tumour, facilitating the spread of cancer cells. The aim of this thesis was to develop a biomimetic 3D *in vitro* model of colorectal cancer with controllable matrix parameters that regulate cancer invasion, the formation of a primitive vascular network and response to targeted drug treatment.

A novel 3D *in vitro* cancer model was established based on the removal of interstitial fluid in collagen type I hydrogels. Colorectal cancer cells cultured in dense collagen gels formed well-defined cellular aggregates mimicking avascular micrometastases observed *in vivo*. Cancer cells invaded from the artificial cancer mass (ACM) into the stromal surround in cell specific patterns, either as spherical aggregates or cell sheets. Invasion into a denser collagen matrix altered the migration pattern predominantly to cell sheets. Laminin was found to enhance the invasion profile of colorectal cancer cells independent of stromal matrix density. The pro-invasive and epithelial-mesenchymal transition (EMT) markers MMP7 and vimentin were upregulated in 3D cultures in comparison to 2D monolayers.

Stromal cultures containing fibroblasts and endothelial cells formed highly branched end-to-end vascular networks in the presence of laminin. The addition of cancer cells produces significantly longer but substantially less interconnected vascular networks mimicking *in vivo* ‘leaky’ tumour vasculature. The loss of CK20 by invading cancer

cells significantly correlated with the overall distance of invasion into the stromal surround. Although the expression of the biomarker EGFR was upregulated in 3D, targeted treatment using cetuximab lead to a greater inhibition profile in 2D monolayers than in 3D cultures. Drug resistance in 3D cultures corresponded with the presence of cancer stem cells.

These findings signify the importance of 3D *in vitro* cancer models as important tools to study the effect of microenvironmental conditions on tumour malignancy.

Table of Contents

Publications and presentations

Journal articles

1. **Magdeldin T**, López-Dávila V, Villemant C, Cameron G, Drake R, Cheema U, Loizidou M. The efficacy of cetuximab in a tissue-engineered three-dimensional *in vitro* model of colorectal cancer. J Tissue Eng. 2014 Jul 23;5: 1–9.

2. Ricketts K, Cheema U, Nyga A, Castoldi A, Guazzoni C, **Magdeldin T**, Emberton M, Gibson A, Royle G, Loizidou M. A 3D *in vitro* cancer model as a platform for nanoparticle uptake and imaging investigations. Small. 2014 Jul 2;10: 3954-3961.

3. Bandula S*, **Magdeldin T***, Stevens N, Yeung J, Moon JC, Taylor SA, Cheema U, Punwani S. Initial validation of equilibrium contrast imaging for extracellular volume quantification using a three-dimensional engineered tissue model. Journal of Magnetic Resonance Imaging. 2015. Oct 19. DOI: 10.1002/jmri.25066

4. López-Dávila V, **Magdeldin T**, Welch H, Dwek M, Uchegbu I, Loizidou M. Efficacy of DOPE/DC-cholesterol liposomes and GCPQ micelles as AZD6244 nanocarriers in a 3D colorectal cancer *in vitro* model. Nanomedicine 2016; doi:10.2217/nm.15.2016.

5. **Magdeldin T**, López-Dávila V, Cameron G, Emberton M, Loizidou M, Cheema U. Engineering a vascularized 3D *in vitro* model of cancer progression. Manuscript in preparation.

Conference presentations

1. **Magdeldin T**, Loizidou M, Cheema U. Tissue engineering a physiologically and spatially relevant 3D *in vitro* model of colorectal cancer. TERMIS 2013, Istanbul, Turkey.

2. Ricketts K, Nyga A, Guazzoni, C, Castoldi A, **Magdeldin T**, Montemurro G, Welch H, Cheema U, Royle G, Loizidou M. Imaging gold nanoparticles in a novel tissue engineered 3D *in vitro* cancer model. AACR 2012, Dublin, Ireland.

3. **Magdeldin T**, Loizidou M, Cheema U. Tissue engineering a physiologically relevant 3D *in vitro* model of colorectal cancer. TCES 2014, Newcastle, UK.

4. **Magdeldin T**, López-Dávila V, Cameron G, Emberton M, Loizidou M, Cheema U. Engineering a vascularized 3D *in vitro* model of cancer progression. AACR 2016, New Orleans, United States.

List of Figures

List of Tables

Abbreviations

2D	Two-dimensional
3D	Three-dimensional
ACM	Artificial cancer mass
ANOVA	Analysis of variance
bFGF	Basic fibroblast growth factor
BM	Basement membrane
BSA	Bovine serum albumin
CAF	Cancer associated fibroblasts
CRC	Colorectal cancer
ECM	Extracellular matrix
EGFR	Epidermal growth factor receptor
EMT	Epithelial – mesenchymal transition
FBS	Fetal bovine serum
GAG	Glycosaminoglycans
H&E	Haematoxylin and Eosin
HA	Hyaluronic acid
HCT116	Human colon carcinoma cell line
HDF	Human dermal fibroblasts
HIF	Hypoxia inducible factor
HT29	Human colon adenocarcinoma cell line
HUVEC	Human umbilical vein endothelial cells
IGF	Insulin growth factor
MAPK	Mitogen activated protein kinase
MEM	Minimal essential medium

MMP	Matrix metalloproteinase
mRNA	Messenger RNA
P/S	Penicillin/streptomycin
PBS	Phosphate buffered saline
PC	Plastic compression
PCL	Poly (ε-caprolactone)
PDGF	Platelet derived growth factor
PEG	Polyethylene glycol
PLA	Poly (lactic acid)
PLG	Poly (lactide-co-glycolide)
PVA	Poly vinyl alcohol
qRT-PCR	Quantitative reverse transcriptase polymerase chain reaction
RGD	Arginine-Glycine-Aspartic Acid Sequence
SD	Standard deviation
SDS-PAGE	Sodium dodecyl sulfate polyacrylamide gel electrophoresis
TGFβ	Transforming growth factor beta
TNFα	Tumour necrosis factor alpha
TX-100	Triton X-100
VEGF	Vascular endothelial growth factor
VEGFR-1/2	Vascular endothelial growth factor receptor 1/2

Chapter One

Literature Review

1 Introduction

Colorectal cancer (CRC) is the third most common diagnosed cancer and is responsible for around 12% of all cancer related deaths annually worldwide[1]. The incidence rate of CRC varies enormously with the highest reported cases occurring in more developed regions such as North America, Europe and Oceania[2]. High risk factors in these regions are mainly attributed to a bad diet (high in animal fat, low in fibre), a lack of physical activity, obesity and smoking[3]. Cancer outcomes would be more successful with improved imaging techniques, which would both accurately define the extent of disease progression at primary detection and follow up progress after treatment; and secondly, better therapeutic regimens to be used when the disease cannot be managed by surgical resection alone. The majority of current cancer models used for developing novel therapeutics at the pre-clinical stage

involve either two-dimensional (2D) *in vitro* reductionist cell culture or injecting cancer cells into genetically engineered severe combined immunodeficiency (SCID) animal models. Underlying mechanistic investigations are not always easy in these models due to the absence of extracellular matrix (ECM) interactions associated with the local tumour microenvironment or the biological complexity of *in vivo* animal models. The ECM is vital to cancer initiation and progression as it provides cells with physical, chemical and biomechanical cues that regulate the growth of a tumour. During the growth of a tumour, the ECM becomes highly deregulated and promotes the migration of cancer cells to distinct regions through the disorganized tumour vascular supply. In order to understand the growth of CRC, an understanding of the molecular basis of CRC initiation and progression and the role of the tumour microenvironment is required.

1.1 The pathogenesis of colorectal cancer

The majority of CRC cases are adenocarcinomas that originate from colonic epithelial cells. In addition to the significant lifestyle and environmental risk factors, there has been considerable progress in pinpointing specific genetic mutations that contribute to or underlie the progression of CRC. Structurally, the colon contains columnar and mucinous cells (glands/crypts) that are approximately 40-60 cells deep. In healthy colonic tissue, proliferation of epithelial cells is restricted to the lower portions of the glands and cells migrate toward the upper mucosal surface[4]. During the initiation of tumourigenesis, epithelial cells become incapable of implementing the normal cellular apoptotic signal during migration from the base to the glands and develop an increased proliferative profile[5]. This cellular dysfunction

begins with complications in cell division and subsequently differentiation that leads to the progression of morphologic lesions such as adenomas, aberrant crypt foci (ACF), polyps and ultimately tumours.

The development of CRC occurs through a sequence of well characterized histopathological changes from adenoma to carcinoma (Figure 1.1) caused by an accumulation of genetic and epigenetic mutations[6].

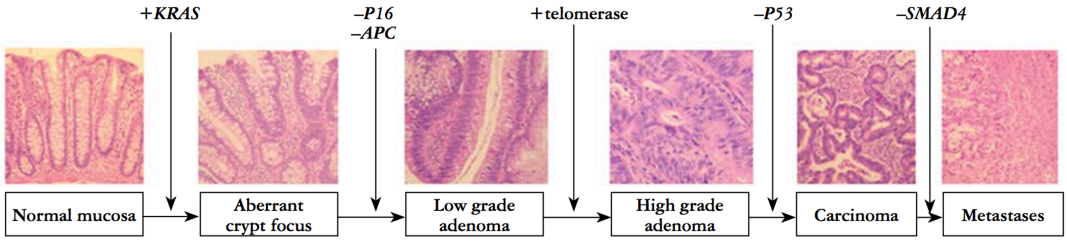

Figure 1.1: The adenoma – carcinoma sequence during CRC development. Histological panels that show the morphological characteristics of lesions at each step. (Image adopted from [7])

Sporadic CRC makes up ~85% cases and contain an abnormal molecular profile including chromosomal imbalances in chromosomes 5q, 8p, 17p and 18q which contain important oncogenes and tumour suppressor genes that contribute to carcinogenesis[8]. On the other hand, genetic cases (~15% cases) are usually linked with syndromes such as familial adenomatous polyposis (FAP) and Lynch syndrome (LS), which carry a significant increased risk of the development of CRC. FAP is an inherited disorder that involves the presence of numerous adenomatous polyps scattered through the intestinal mucosa[9]. Although these polyps are initially benign, without treatment they are highly likely to become malignant and are recognized as major predispositions to CRC initiation. Many of the key genes involved in colorectal carcinogenesis include the oncogene *KRAS* and the tumour suppressor

genes *P53*, *SMAD4* and *APC*[10]. Mutations in the *APC* gene are the most common prerequisite for CRC development and the risk by the age of 40 years for carriers of the mutated version is almost 100%[11]. APC mutations are found in the earliest stages of the adenoma to carcinoma sequence and help to form ACF, which are precursors to the development of colonic polyps. *APC* is an important regulator and binding partner of the cellular adhesion molecule β-catenin[12]. When mutated, APC cannot bind to β-catenin, which leads to the accumulation of intracellular β-catenin levels. This rise in β-catenin levels constitutively activates the *Wnt* signaling pathway, a key signal transduction pathway involved in the homeostasis of the colonic epithelium[13]. Wnt signaling molecules have been implicated in tumours of the breast, prostate, brain and colon[14]. More recently it has been implicated in critical aspects of normal cellular function such as cell proliferation, migration, polarity and organogenesis during embryonic development[15]. Due to its critical function in embryonic development, defects in the *Wnt* pathway are characteristically associated with many cancers.

In LS (also known as hereditary nonpolyposis CRC, HNPCC) the molecular mechanisms vary slightly, with a high occurrence of frameshift mutations and base pair substitutions that appear in microsatellites. Microsatellites are repeating sequences of DNA, largely between 1-6 base pairs in length and occur throughout the genome. This microsatellite instability (MSI) is mainly characterized by mutations involved in mismatch repair (MMR) proteins that initiate repair of nucleotide errors during DNA replication such as MLH1, MSH2, MSH6 and PMS2[16,17]. Mutations in MLH1 are also responsible for ~12% of sporadic CRC. This is due to hypermethylation of the CpG islands in the promoter region of MLH1, which prevents MLH1 transcription ultimately leading to deficient MMR and high

levels of microsatellite instability (MSI-H)[17].

1.1.1 The EGFR pathway in colorectal cancer

EGFR is a 170-kDa growth factor receptor tyrosine kinase (RTK) that belongs to the ErbB family of cell membrane receptors. Its main autocrine ligands are EGF and transforming growth factor-alpha (TGF-α), which have been shown to be activators of cell proliferation in CRC[18]. Ligand binding of EGF induces dimerization of EGFR leading to autophosphorylation of intracellular tyrosine kinases. This initiates two main pathways known as the mitogen-activated protein kinase (MAPK) pathway and the phosphatidylinositol 3-kinase (PI3K) pathway (Figure 1.2). The activation of downstream transcription factors results in increased cell proliferation, adhesion, migration and angiogenesis[19].

EGFR is commonly overexpressed in a number of cancers including ovarian, cervical and bladder carcinomas with a strong association between overexpression and poor patient outcome[20]. In CRC, the clinical significance of EGFR is not as clear. Some studies have found a strong correlation between EGFR overexpression and poor survival[21] while other studies have reported conflicting findings[22]. Due to the pro-tumourogenic properties of EGFR, therapies targeting this receptor have gained significant attention in recent years[23,24].

While the use of cetuximab has led to great success in the treatment of CRC, the exact molecular mechanism underlying the clinical response remains largely unknown. Mutations within the EGFR pathway affect the response of this targeted therapy and it remains largely ineffective in a subset of *KRAS* and *BRAF* mutant

tumours[25,26]. This is typically due to constitutive activation of both the RAS and RAF proteins downstream of EGFR.

Approximately 40% of all CRC patients carry a *KRAS* mutation, where 90% of these mutations occur in codons 12 and 13[27]. Mutations in these codons lead to continuous activation of the MAPK pathway regardless of upstream EGFR signaling. There have been several studies in recent years which have shown that KRAS mutations are significantly associated to anti-EGFR therapy resistance and poor overall patient survival[7,26,27].

On the other hand, *BRAF* mutations occur in around 5-10% of all CRC cases and V600E mutations represent 90% of all *BRAF* mutations[28]. While mutations in *KRAS* occur more specifically in CRC, *BRAF* mutations occur in a variety of different cancers including ovarian, thyroid and particularly melanomas[29]. While *BRAF* mutations have been associated with poor patient outcome, the therapeutic efficacy of anti-EGFR treatment on *BRAF* mutant tumours has been contradictory[30]. It is routinely accepted that *KRAS* and *BRAF* mutation status should be tested as prognostic biomarkers instead of EGFR expression levels[27].

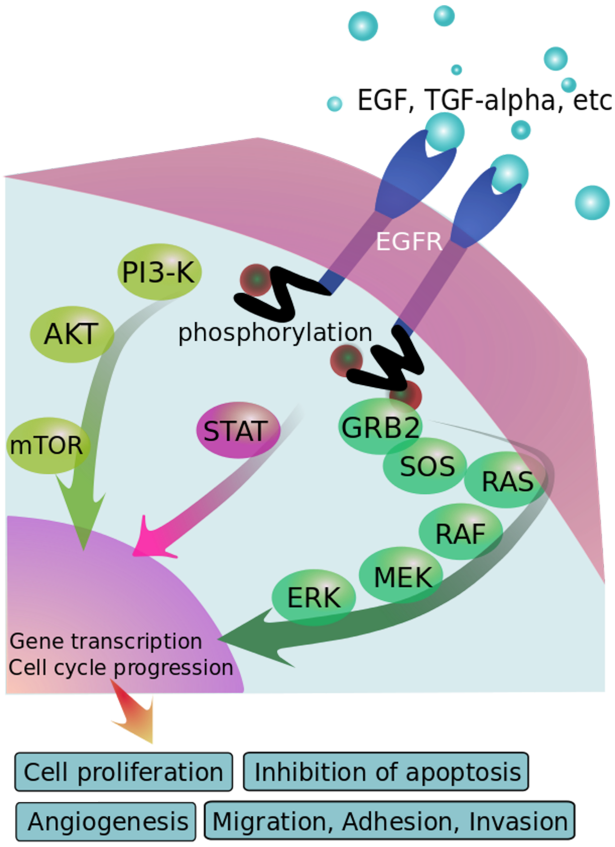

Figure 1.2: The EGFR signaling pathway. Binding of the extracellular ligands to EGFR stimulates downstream signaling to regulate cell proliferation, migration and survival via the MAPK signaling pathway.

1.1.2 The tumour microenvironment

The tumour microenvironment consists of a variety of cell types including fibroblasts, endothelial cells (ECs) and immune cells such as macrophages and lymphocytes. Other non-cellular components include the ECM, which is a large assortment of proteins, glycoproteins and polysaccharides, ECM remodeling proteins such as MMPs, soluble growth factors such as growth factors (VEGF, PDGF and FGF) and cytokines (TGFβ, TNFα and IL-6 and 10)[31,32]. The ECM not only provides structural support for cells but also directs their proliferation, differentiation

and migration through a series of chemical and biomechanical cues via integrins and discoidin domain receptors[33].

In healthy colonic tissue, the local microenvironment acts as a physical barrier against carcinogenesis and promotes normal tissue function and homeostasis[34]. In CRC, the sequence of adenoma to invasive carcinoma is mediated via the surrounding tumour microenvironment. Neoplastic epithelial cells modulate the expression of ECM remodeling proteins, which are mainly produced by adjacent stromal cells to promote their own growth, survival and invasion. Initially, these stromal cells are not tumour-promoting cells, and it has been shown before that they may confer anti-tumourogenic properties[35]. However, as a tumour grows the cancer cells exploit the stromal cells function to remodel the ECM to stimulate a pro-tumourogenic environment. This deregulation of the surrounding ECM extensively modifies the structure, composition and stiffness of the microenvironment and is understood as a necessary event for the dissemination of cancer cells to distant sites[36]. The increase in ECM stiffness is due to increased cross-linking of collagen that alters the biomechanical properties, which cells respond to by exerting markedly different forces in response[37]. Changes in the stiffness alter gene expression profiles through mechanotrasnduction pathways and directly impacts how migratory cancer cells interact with the surrounding ECM[38].

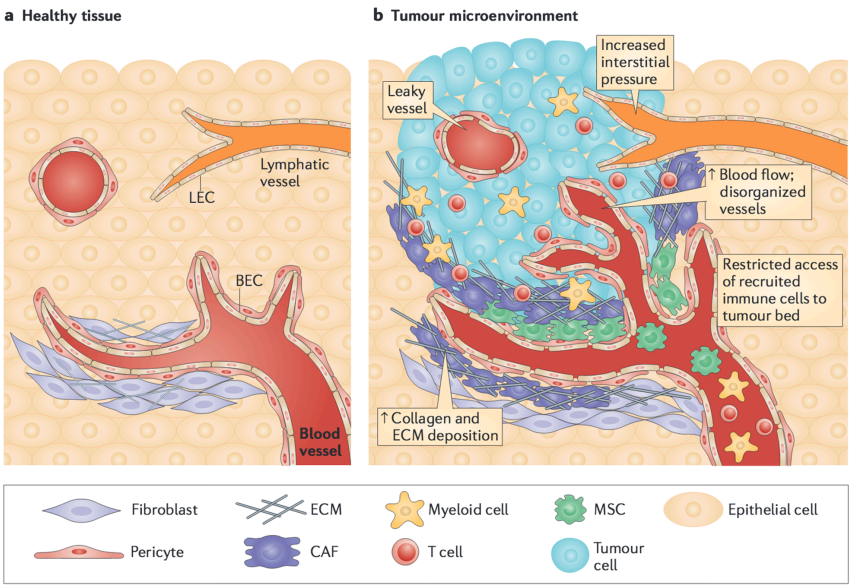

Figure 1.3: Structural differences between healthy tissue and the tumour microenvironment. The tumour microenvironment contains increased ECM deposition, disorganized blood vessels and chronic inflammation that leads to the recruitment of immune cells. (Image adopted from [39]).

1.1.3 Mechanisms of cancer cell invasion

Despite the advances in treatment modalities, metastasis, the spread of cancer cells from the primary tumour site to distant organs, remains the foremost cause of cancer related mortality[40]. The transformation of cancer epithelial cells is plays a vital role in the development of secondary tumour sites[41]. This highly conserved process, known as the epithelial to mesenchymal transition (EMT) governs a variety of normal cellular processes in embryonic development and tissue repair[42]. In carcinomas, the EMT process leads to a shift in cell phenotype resulting in the loss of cell-cell adhesion, apico-basal polarity and active remodeling of the actin cytoskeleton required for motility. Simultaneously, the increased expression of the mesenchymal marker vimentin and deceased expression of the epithelial marker e-cadherin gives rise to the elongated spindle-like morphology that is often associated

with increased migration and invasiveness[43].

Cell migration is a highly complex and coordinated process which involves an intricate series of interactions between tumour cells and the tumour microenvironment that facilitate both breakdown of the surrounding ECM and subsequent invasion. There are three described mechanisms by which tumour cells invade. Tumour cells can migrate either in a mesenchymal or collective type of invasion and an amoeboid type of movement[44].

One example of cancer cell invasion which occurs within the gastrointestinal tract gives rise to small clusters of cancer foci are often seen at the invasive front of carcinomas[45]. This process of tumour budding can often be quantified on histological samples and is routinely used in the clinic to assess tumour aggressiveness[46]. The migration of tumour buds is thought to be largely mediated by activation of signalling cascades controlled by integrins; adhesion molecules that facilitate cell-cell and cell-matrix interactions, combined with the action of matrix metalloproteinases (MMPs) to enable basement membrane penetration. This mechanism of invasion is suggested to be representitive of the EMT process in carcinomas and is associated with higher tumour grade and lymph node metastases[47].

Another pattern of migration exhibited by cancer cells is the movement of whole cell sheets. In cancer, this mechanism of migration is exclusive to carcinomas and is thought to be, at least in part controlled by the active proteolysis of the basement membrane barrier by MMPs[48,49] followed by collective migration. Cells maintain their cell-cell junctions in order to move as a cohesive unit. Although, the precise molecular pathways are not well understood it is likely they would mimic epithelial cell sheet migration during embryonic development[50]. One member of the MMP

family which is expressed by epithelial cells and has been implicated in colorectal cancer invasion is MMP7[51]. MMP7 is involved in the degradation of a range of ECM proteins including collagens and laminin and is often expressed solely by tumour cells whereas most MMPs are expressed by adjacent stromal cells[52].

While tumour budding and collective migration follow a mesenchymal pattern, the migration of single cells follows an amoeboid mechanism[53]. This type of migration is thought to be the fastest mechanism of cancer cell migration with reported speeds of up to 4µm/min observed *in vivo*[54]. Amoeboid migration is utilized by leukocytes and it is thought invasive cancer cells can hijack the same mechanism to metastasize[55]. Recent studies have shown that amoeboid migration is independent of the activity of proteases and cells migrate by squeezing through gaps within the fibrillar collagen network[53]. The activation of chemoattractant receptors on the membranes of cells triggers actin polymerization and the formation of pseudopods. Contraction of the cortical actin networks driven by Rho-ROCK signaling promotes the remodelling of the cell cortex ultimately generating an irregular morphology characteristic of amoeboid migration[56]. Mesenchymal and amoeboid mechanisms of cancer are mutually interchangable highlighting the plasticity and complexity of tumour invasion mechanisms[57].

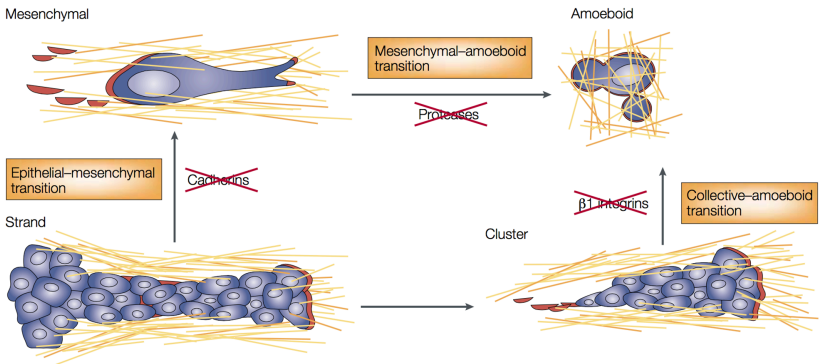

Figure 1.4: The plasticity of tumour invasion mechanisms. Cancer cells can undergo changes in motility in response to their environment. (Image adopted from [57])

1.2 Neovascularization

The development of an adequate blood supply is essential to a growing tumour as it provides nutrients, oxygen and aids in the removal of waste products[58]. The process of developing new blood vessels is known as neovascularization and occurs mainly by three main mechanisms; vasculogenesis, arteriogenesis and angiogenesis. This section will focus mainly on vasculogenesis and angiogenesis, as these are the most well understood processes in both embryonic and adult blood vessel development and in the development of diseases such as cancer.

1.2.1 Vasculogenesis

Vasculogenesis is the formation of new blood vessels by a de novo production of endothelial cells (ECs). Typically, vasculogenesis occurs during development of the mammalian embryo where angioblasts differentiate into ECs that assemble into vascular networks (Figure 1.5a)[58]. There are five main processes that occur during vasculogenesis; the birth of angioblasts, the end to end aggregation of angioblasts, angioblast elongation and the assembly of cord-like structures, the amalgamation of individual vascular networks to form capillary-like networks and finally the endothelialization and lumenization of these networks[59]. Both cytokine-mediated interactions and a sophisticated series of cell-cell and cell matrix interactions regulate these processes. These growth factors include vascular endothelial growth factor (VEGF) and its receptor VEGFR-2, which regulate differentiation of mesenchymal progenitors down an endothelial lineage, CD31 and CD34 which establish strong cell-cell interactions, VEGFR-1 involved in lumen formation,

angiopoietin-1 (Ang-1) and its receptor Tie2 involved in blood vessel maturation and integrins that are essential in regulating cell shape and migration[59,60]. The importance of these molecules have been implicated in gene knockout studies in mice[61–64].

1.2.2 Angiogenesis

On the other hand, angiogenesis is the sprouting of new blood vessels from pre-existing vasculature (Figure 1.5b). It is the best understood of all the neovascularization processes due to its presence of in a variety of diseases such as ischemia, wound healing, cancer and inflammatory disorders[65]. Angiogenesis begins with vasodilation in pre-existing blood vessels, a process that involves nitric oxide[66]. The upregulation of VEGF in the local microenvironment by ECs and stromal cells leads to an increase in vascular permeability. This permeability coupled with MMP degradation of the basement membrane recruits pericytes and smooth muscle cell migration. Strict regulation of this proteolytic degradation is fundamental as excessive degradation of the ECM leaves behind too little matrix support for the new branches to sprout. Pro-angiogenic molecules such as VEGF and basic fibroblast growth factor (bFGF) are further released through paracrine signaling pathways by stromal cells. The increase of pro-angiogenic stimuli guides EC migration that occurs through tip and stalk cells[65]. Tip and stalk migration is regulated through Notch signaling which plays a key role in directing EC behaviour during vessel patterning[67]. Microenvironmental cues then regulate the position of tip cells and drive them to migrate to the new blood vessel where they fuse to extend the vascular network[58]. The final step of blood vessel maturation requires the

autocrine production of platelet derived growth factor (PDGF) by ECs that recruits pericytes and smooth muscle cells to coat the vessel wall[68].

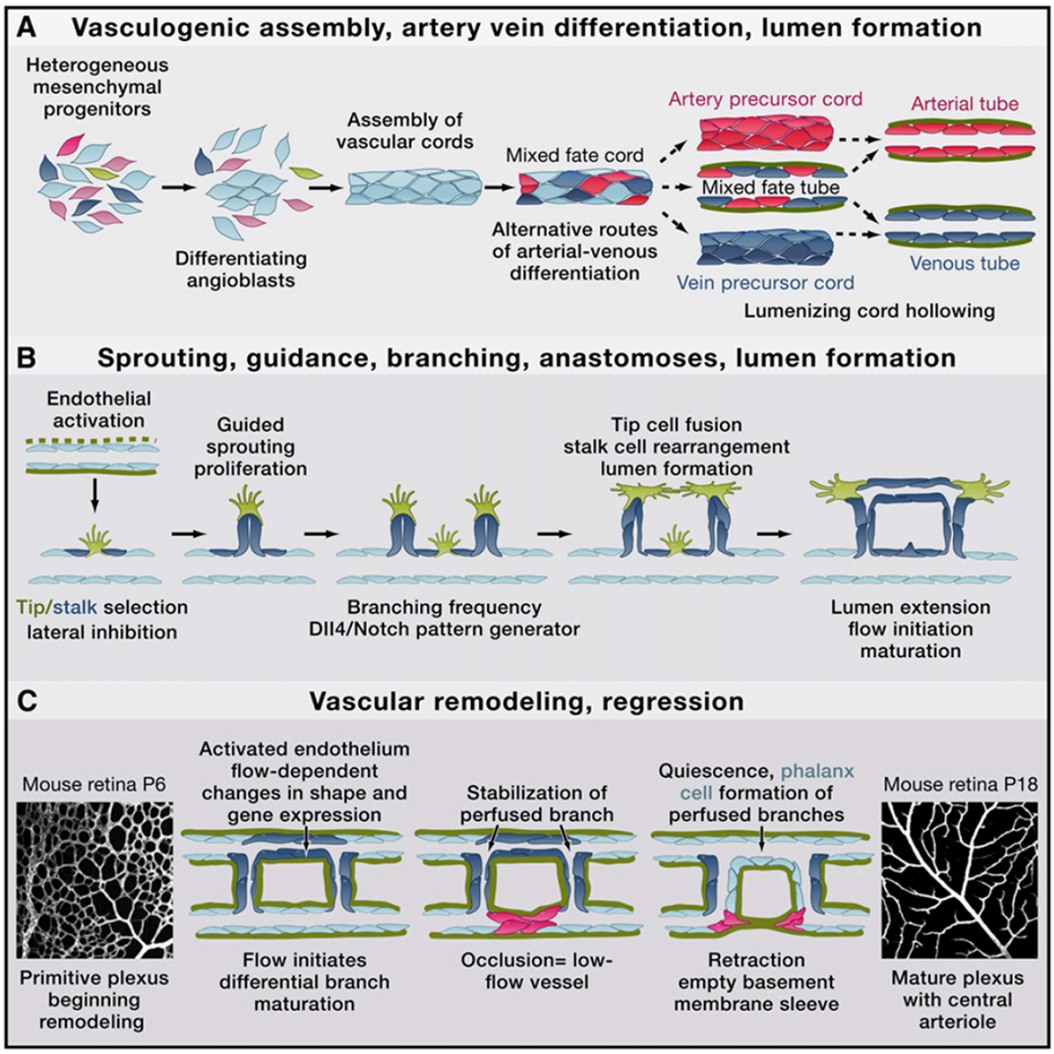

Figure 1.5: Hallmarks of blood vessel formation. A schematic diagram depicting (a) the vasculogenic process during blood vessel formation where angioblasts differentiate into ECs, form vascular cords and acquire a lumen, (b) the angiogenic process depicting vessel sprouting, tip cell migration and fusion followed with lumen formation, (c) the sequential steps involved in vascular remodeling of blood vessels. (Image adopted from [65])

1.2.3 Tumour induced angiogenesis

As described in Section 1.2, angiogenesis is a highly regulated process that involves VEGF, angiopoietins, Notch and the integrin family of receptors. During normal embryonic development there is a delicate balance between these pro-angiogenic and anti-angiogenic factors that creates healthy functional blood vessels. During normal embryonic development, there is a temporary shift towards pro-angiogenic signaling this is kept in check by inhibitory mechanisms such as endostatins and angiostatins[69,70]. During the growth of a tumour, this balance is lost resulting in a range of morphological and functional differences between normal and tumour vasculature.

Tumour vasculature is made up of a highly disorganized, hyperpermeable, immature blood vessel network consisting of abnormal vessel dynamics (figure 1.6)[71]. There is a loss of the vascular hierarchy whereby capillaries, arterioles and venules are indistinguishable from one another by immunohistochemical analysis[72]. Furthermore, the diameters of blood vessels is often irregular and are an inconsistent shape with the endothelial layer containing spaces that contribute to the leakiness of blood vessels[73]. Adjacent proliferating tumour cells cause compression of the vascular walls of the blood vessels increasing the interstitial pressure[74]. This disorganization of the vascular supply surrounding a tumour results in an inability to supply oxygen and remove waste products efficiently leading to hypoxia and acidosis in the local microenvironment[75,76]. Understanding some of the molecular mechanisms involved in how the tumour vasculature is disorganized is essential to developing novel strategies to improve the delivery of anti-cancer therapies. For example, micro-regional hypoxia is associated with resistance to both chemotherapy and radiotherapy[77,78]. Hypoxia inducible factor -1 (HIF-1) is an important regulator

of the hypoxic response in a tumour. Under hypoxic conditions, HIF-1α dimerizes with HIF-1β, creating a dimer complex which then translocates to the nucleus leading to increased VEGF transcription[79].

Of all the molecular markers involved in angiogenesis, none have gained more attention than the VEGF family and their receptors (Figure 1.6). However, the role of VEGF is not only limited to angiogenesis and vascular permeability and has been shown to regulate the function of cancer cells[80]. For example, there have been significant amounts of VEGFR found on cancer cells of the breast and colon[81,82]. It is thought that overexpression of VEGF in response to the local hypoxic environment may stimulate the production of VEGFR on cancer cells which respond to other VEGF ligands to support tumour growth. Therefore, the overexpression of VEGF in a variety of tumours implies the presence of an autocrine VEGF/VEGFR signaling loop. This has been demonstrated in subgroups of leukemia whereby disrupted VEGF/VEGFR2 autocrine loops induce cancer cell apoptosis and inhibit cancer cell migration[83]. Recent studies have shown in a model of colorectal cancer that VEGFR1 activation by the VEGF-A or VEGF-B ligands lead to activation of the MAPK pathway ultimately stimulating cell proliferation, migration and invasion[84]. It is postulated that VEGF may promote growth by directly acting on receptors via an EC independent manner opening up a new avenue of anti-cancer therapies that target VEGFR on cancer cells.

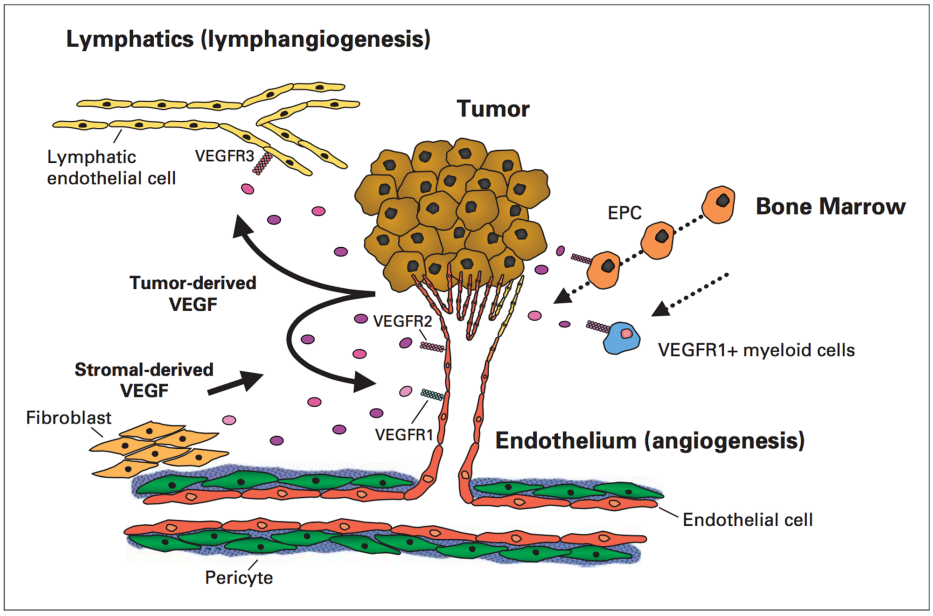

Figure 1.6: The role of VEGF in tumour induced angiogenesis. VEGF ligands expressed by cancer and stromal cells stimulate VEGFR expression by lymphendothelial, endothelial or hematopoietic cells. The presence of VEGF enhances the proliferation, survival, and migration of cells in the tumour microenvironment. (Image adopted from [85])

1.3 Three dimensional *in vitro* models of cancer

Until recently, the gold standard for *in vitro* pharmacological testing of anti-cancer drugs has been reductionist 2D cell culture. Classical 2D monolayer studies have proven invaluable for dissecting cancer cell behaviour to a certain degree. However, a large body of evidence demonstrates that 2D cell culture does not accurately reflect the 3D *in vivo* tumour microenvironment[86–88]. This is particularly relevant for oxygen and nutrient gradients, drug pharmacokinetics and gene expression profiles. The lack of a clear understanding of how cell-cell and cell-matrix interactions influence the progression of a tumour has prompted development of novel 3D *in vitro* cancer models to address this issue. Another incentive to develop 3D *in vitro* models is to replace, reduce and refine the use of animal models in research in line with the NC3R initiative.

Many recent studies have demonstrated that the unnatural flat 2D surface which basic cancer research is carried out may be inadequate for accurate drug testing[89]. Therefore, a wide generation of new sophisticated organotypic 3D cell culture systems have been adopted to improve efficacy outcomes of new therapeutics. The use of these *in vitro* 3D culture models helps bridge the gap between conventional 2D cell culture studies and animal models, improving the pre-clinical selection process of new chemotherapeutics while simultaneously lowering the development costs. Development of these models is essential in constructing physiologically relevant models to study the underlying mechanisms of cancer progression.

The tumour stroma has also been identified as an important regulator of tumourigenesis[90]. This includes stromal cells such as fibroblasts, endothelial cells and immune cells that often interact close to and around tumours *in vivo*. The tumour vasculature, which is often leaky for example, can influence the distribution of a

pharmaceutical agent, as it needs to penetrate vessel walls before it can permeate sufficiently through the tumour tissue. In comparison to normal healthy tissues the tumour stroma, consists of a distorted ECM and an increased number of stromal cells that release MMPs that facilitate tumour progression[91]. As tumours are heterogeneous in nature[92], drug distribution throughout them is often also thought to be heterogeneous. Within the tumour microenvironment, differing regions of hypoxia and pH in addition to the increases in the interstitial fluid pressure can all affect the macromolecular penetration of drug through the tissue.[93] Therefore, improving drug bioavailability and delivery is essential to sustaining adequate exposure of cancer cells to toxic agents.

Cell growth and function lies within a continuous intricacy of cell-cell and cell-matrix interactions facilitated by the ECM - a heterogeneous collection of interlocking macromolecules of collagens, proteoglycans, polysaccharides and various other soluble matrix proteins[94]. The ECM mediates many cellular functions through focal adhesions found on the cell membranes of cells. These focal adhesion points are composed of cytoplasmic proteins and cell membrane receptors that interact with the cell cytoskeleton to activate mechanotransduction pathways to regulate gene expression[38]. Biomaterials aim to mimic these functions of the ECM. From a scaffold perspective, fundamental design principles include good mechanical properties that support and maintain cellular function, biocompatibility to support cell viability (of cancerous and stromal cells) and biodegradability to be able to mimic cancer invasion and ECM degradation[95].

Although tumours are disorganized organs, there is still an inherent level of 3D structure due to tumour cells interacting with the surrounding ECM. One of the most striking differences between 2D and 3D cultures is the morphological differences

caused by the presence of the ECM. Cells in monolayer culture adhere and spread on flat surfaces in 2D dimensions, i.e. only in the horizontal plane. For example, the absence of movement in the vertical plane forces apical-basal polarity which may be important for cell types such as epithelial cells but not for others such as fibroblasts, which prefer a front to rear polarized shape necessary for cell migration[96]. For example, these interactions define cell polarity and geometry, which are critical for normal cellular function. Weaver and colleagues have demonstrated that the formation of polarized 3D structures by both normal and malignant epithelial cells, protected cells against apoptosis whereas non-polarized cells remained sensitive to apoptosis[97]. Apart from the mechanical support, the ECM also regulates the distribution of nutrients, cytokines and gases such as oxygen and carbon dioxide, which are all necessary for processes such as angiogenic sprouting and wound healing[98]. In monolayer cultures, nutrients and soluble factors diffuse freely throughout the culture medium and it is difficult to replicate the gradients that are present in tissues. Due to the structural organization present in 3D cultures, this can act to hinder the penetration of soluble factors, creating an oxygen or nutrient gradient that can regulate long-term morphogenetic events such as the presence of hypoxia[99].

The following section aims to discuss some of the 3D *in vitro* cancer models used in recent years. They are classified broadly into two categories; scaffold free and scaffold based culture systems. Scaffold free approaches include the use of multicellular spheroids and scaffolds based approaches aim to mimic the macromolecular structure of the ECM and fall under two main categories: natural scaffolds and synthetic polymers.

More complex *in vitro* tumour modelling has prompted the use of biomaterial-based

approaches for tissue engineering. This has prompted the use of both natural and synthetic matrices with customizable properties to mimic the 3D microenvironment *in vivo*. Although many of these materials were initially intended for *in vivo* tissue engineering and regenerative medicine, many have recently been applied to cancer research as established 3D cell culture models.

1.3.1 Multicellular tumour spheroids

Scaffold free 3D *in vitro* cancer models mainly includes multicellular tumour spheroids, which are three-dimensional assemblies of cancer cells[100]. They are the most widespread 3D *in vitro* models used for drug testing. These are aggregates of cancer cells, and due to their cellular organization have been shown to mimic the phenotype and gene expression profile of tumours *in vivo*[101]. They comprise of actively proliferating surface exposed cells with nutrient deprived hypoxic quiescent cells in the inner region of the spheroid (Figure 1.7). Multicellular spheroids can be formed using a variety of different techniques. These include the hanging drop method, spinner flask cultures and culturing cells on non-adherent surfaces such as those pre-coated with agar[100]. The hanging drop method is the most common method used and involves pipetting cells in small volumes of media on the inner side of a petri dish lid and inverting the lid upside down. Under the force of gravity, this causes cells to aggregate at the bottom of the hanging drop and spheroids can typically take 24 hours to form for a variety of different cancer cell lines[102]. As drug efficacy is usually lost at the 3D pathophysiological level due to inadequate

penetration of the drug molecule, spheroids are often the cheapest and simplest models to employ to test new drugs as a precursor to animal studies[103].

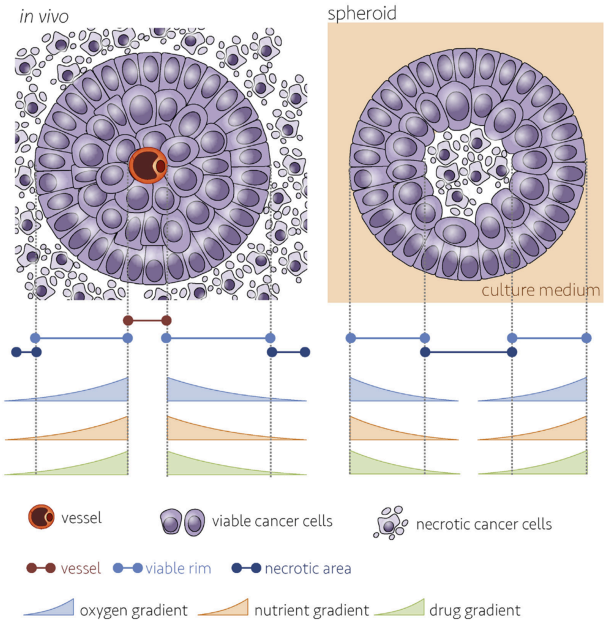

Figure 1.7: Gradient formation *in vivo* and in multicellular tumour spheroids. A schematic diagram depicting the oxygen and nutrient gradients in a tumour compared to multicellular spheroids. (Image adopted from [104])

With regards to multicellular spheroids, the most suitable model of cancer must be carefully chosen to match the requirements of the investigation. For instance, spheroid monocultures have long been used to identify new mechanistic pathways involved at the 3D cellular level, whereas spheroid co-cultures have been used to explore combinations of therapies such as radiotherapy and anti-neoplastic drugs[105]. Spheroids have recently been employed to evaluate the anti-proliferative effects of two anti-cancer drugs with distinctive activity profiles; 5-fluorouracil (5-FU) that targets actively proliferating cells and tirapazamine (TPZ), a hypoxia-activated toxin[106]. Following drug incubation, 3D spheroids displayed remarkable resistance to 5-FU in comparison to their 2D counterparts whereas TPZ induced a far greater reduction in cell viability in 3D spheroids than 2D cultures. These differences in

chemosensitivity may be attributed to the fact 5-FU actively targets proliferating cells and not the quiescent cells within the spheroids, while TPZ targets hypoxic cells known to be present within spheroids.[107] This study further highlights the differences of cytotoxicity treatment when the 3D physiological environment is enhanced.

With regards to drug evaluation, spheroids are inherently limited by several factors. As there is no external bulk ECM component present in spheroid cultures, it is difficult to model cancer invasion without nesting the spheroids within a matrix to which they can invade. However, cells cultured in 3D have also been shown to endogenously secrete various ECM proteins such as collagen and laminin[108]. While cells cultured in 2D also secrete ECM proteins, they are typically upregulated in 3D culture systems. This has been demonstrated in a 3D model of pancreatic ductal adenocarcinoma (PDAC) where the authors postulated the increase in matrix production was strongly correlated to the sphere formation and compaction of these cells in a 3D spatial configuration[109]. Due to the lack of an adequate vascular system, oxygen, nutrients and other compounds diffuse through the spheroids creating a concentration gradient limiting these compounds to the outer most cells[100]. This not only limits the maximum size of spheroids to ~500µm, but also prevents sufficient distribution of most drugs, which tend to be molecules larger than oxygen or carbon dioxide for instance. The diffusion properties of new prospective anti-cancer drugs are occasionally overlooked when they are assessed and therefore, more detailed pharmacokinetic studies are required to distinguish between general lack of efficacy of the agent and insufficient drug penetration. Nonetheless, there has been noteworthy progress in this field. A recent study reported exploiting diffusion gradients within spheroids to evaluate penetration of large antibody molecules such

as the anti-mesothelin immunotoxin SS1P[110]. The fluorescently labelled SS1P showed limited penetration that plateaued after 4 hours of incubation, which matched the reduced cytotoxicity observed in spheroids compared with 2D monolayers. However, this also reiterates the need for a standard analytical endpoint assay and furthermore, an accurate means for testing cell viability in spheroid cultures and in other 3D *in vitro* disease models. The assays must provide suitable accuracy, sensitivity and reproducibility while testing a robust variety of compounds. Classically, the same methods used to assess cell viability in 2D monolayer are used for spheroid cultures[111,112]. As there is currently no universal endpoint assay; a variety of different methods can be employed in combination to provide the appropriate results.

1.3.2 Natural scaffolds

Natural scaffolds are composed of ECM components that make up an interlocking mesh of fibrous proteins and glycosaminoglycans (GAGs) including collagens, fibrin and hyaluronic acid[113,114]. They provide tissues and cells with mechanical stability and enable cell-matrix interactions to regulate normal tissue function. When used for *in vitro* 3D cell culture, these scaffolds exist as cross-linked networks of ECM proteins known as hydrogels. Although one of their main disadvantages is their high water content (upwards of 99%), they are still extremely useful for mechanistic investigations as they are entirely malleable by cell behaviour. Natural scaffolds are also biologically active and promote excellent cell adhesion and growth[115].

Collagen type I is the current gold standard for 3D *in vitro* cell culture as collagen type I is the main constituent within the *in vivo* ECM[116]. Despite its poor

mechanical strength, it is the most widely used natural scaffold for 3D *in vitro* cell culture. It can be used either on its own or in combination with other ECM proteins such as glycosaminoglycan or laminin[115,117]. Using a collagen type I scaffold, recent studies have reinforced the importance of the tumour microenvironment, particularly in terms of specific populations of cells, such as CAFs[118]. The presence of CAFs instead of normal fibroblasts was found to disrupt dual cell co-unit formation in a heterotypic model of breast cancer. This was due to the release of high levels of MMPs into the surrounding cell culture medium, which led to the breakdown of the ECM and subsequent disruption and invasion of cancer cells. Collagen gels have also been used to identify novel invasion mechanisms involving Gα13 and discoidin domain receptor 1 (DDR1) exploited by pancreatic cancer cells to differentially regulate cell-cell junctions promoting cell migration[119].

The collagen used throughout this study is acetic acid solubilized rat-tail collagen type I. As the collagen is neutralized with sodium hydroxide to a neutral pH, fibrillogenesis is initiated and cells are embedded within a random organization of collagen fibers[120]. Collagen is highly conserved across entirely different species from sponge to human and has undergone very little evolutionary changes over time[121]. While the mechanical strength of these hydrogels is weak, plastic compression can increase the collagen density and mechanical strength to mimic the *in vivo* tissue barrier.

Hyaluronic acid (HA) has also been extensively used as a scaffold for 3D cell culture of cancer cells. It is a major component of the ECM and plays a key role in cell proliferation and migration. Its main receptors CD44, RHAMM and hyaluronidase-1 (HYAL-1) have been shown to be highly involved in tumour growth and progression in a range of different cancers[122]. Porous scaffolds such as HA make excellent *in*

vitro culture models of glioblastoma, as it is the major GAG component of the brain ECM[123]. However, HA is negatively charged and prevents optimum cell adhesion. This has led to the incorporating of other materials such as chitosan to increase the scaffold properties. The development of hybrid scaffolds such as chitosan-HA hydrogels have been recently employed to model the microenvironment of glioblastoma multiforme (GBM)[124]. GBM cells cultured in chitosan-HA hydrogel were highly resistant to doxorubicin and temozolomide in comparison to 2D cultures and upregulated a number of stem cell like markers including CD44, Nestin and GFAP. Other hybrid materials include HA chemically bound to acrylate groups or reactive thiols to increase crosslinking and have been used to test novel nanoparticle therapies in a model of prostate cancer[87].

Another scaffold often used for *in vitro* tumour modeling and angiogenesis studies is the commercially available ECM and basement membrane extract from the Engelbroth Holm sarcoma mouse, Matrigel®[125,126]. It is a matrix rich in ECM proteins including laminin, enactin and collagen IV, which are the main constituents of the basement membrane[127]. However, the exact protein composition is not known and it usually contains additional growth factors and cytokines[128]. When used for angiogenic assays, the presence of these growth factors induces EC tubule formation within hours of encapsulating ECs within the matrix[129]. For tumourogenic studies, human mammary fibroblasts and breast cancer cells have been co-cultured in a model of Matrigel and collagen and demonstrated the progression from ductal carcinoma in situ (DCIS) to invasive ductal carcinoma (IDC)[130]. Other studies utilizing Matrigel have shown that CAFs co-cultured with breast cancer cells contribute to cancer invasion by upregulating MMP-9 which specifically degrades the BM[131]. The presence of ECs in the co-culture also resulted in a significant

increase in proliferation and branching ductal alveolar morphology of the preneoplastic breast epithelial cells.

1.3.3 Synthetic scaffolds

The recent increase of synthetic polymers for tissue engineering and regenerative medicine applications has prompted the development of more biocompatible and biodegradable synthetic scaffolds that can be used as matrices for 3D cancer models. Synthetic polymers used for cancer studies include poly (lactide-co-glycolide) (PLG), polyethylene glycol (PEG) and poly (ε-caprolactone) (PCL)[132–134]. These synthetic matrices aim to mimic the fibrous and interconnected macromolecular structures of the ECM. They exist in many different forms including fibers, meshes and sponges. Synthetic scaffolds are mechanically stronger in comparison to natural scaffolds making them ideal for simulating the dense microenvironment of a tumour. Although they are not without their disadvantages and often tend to have poor cell adhesion and must undergo surface property modifications to improve their biocompatibility and functionality[135]. Biofunctionalization of polymers can include surface modifications such as adding ECM components such as collagen, fibronectin or laminin to improve cell adhesion[136]. Customizable features such as matrix composition, organization, stiffness and orientation make synthetic scaffolds ideal for use as scaffolds for 3D cancer models.

Synthetic hydrogel matrices such as PEG have been recently modified with the integrin-binding motif Arg-Gly-Asp (RGD) and MMP sensitive substrates to mimic certain degradability aspects of the ECM[137]. Epithelial ovarian cancer cells seeded in this scaffold formed aggregates of cells that resemble tumour masses found in the

peritoneal cavity of patients with advanced disease. Matrix stiffness was also found to regulate the proliferation of these cancer cells. PEG hydrogels have also been used to investigate the motility profile between normal and cancerous cells by tuning the mechanical properties of the scaffold, including the microarchitecture and the overall material stiffness[138]. Controlling pore size and density of the material is critical to understanding some of the molecular mechanisms involved in metastases[139].

The co-polymer, PLG which is FDA approved has also been used as a model of oral squamous carcinoma[126]. This model demonstrated the presence of central hypoxia where oxygen measurements revealed similar oxygen concentration levels to those of *in vivo* tumour masses. Several genes including VEGF, IL-8 and bFGF that are associated with hypoxia were found to be upregulated in comparison to 2D cultures. Other co-polymers with high mechanical strength include poly (lactic acid) (PLA) used as microparticles containing a chemically bound mixture of poly vinyl alcohol (PVA) and chitosan[140]. Breast cancer cells were shown to grow as spheroids on the surface of the porous microparticles and formed tumour like structures *in vitro* with reduced drug efficacy suggesting the role of cellular architecture on drug distribution.

1.4 Aims and objectives

The aim of this research was to apply the principles of tissue engineering and cancer biology to develop a spatially relevant collagen based biomimetic three-dimensional (3D) *in vitro* model of cancer, termed a 'tumouroid' that aims to mimic important aspects of the *in vivo* tumour microenvironment. The main objective was to reproducibly develop a 3D *in vitro* cancer model with the ultimate aim of providing results relevant to the *in vivo* scenario. ECM stiffness and composition are factors that are often overlooked in cancer research but have more increasingly been implicated as significant factors involved in cancer progression[41]. Utilizing collagen type I hydrogels, we used plastic compression (PC) to increase and control the matrix density to mimic the dense nature of *in situ* tumours. The effect of matrix stiffness on cancer invasion was investigated. The stromal compartment was also populated with the basement membrane protein laminin, and stromal cells such as fibroblasts and endothelial cells, which are found in the local tumour microenvironment. The interplay between cancer cells and stromal cells is a critical step in the metastatic cascade. The development of a primitive vascular network was also explored due to the presence of the endothelium adjacent to a tumour *in vivo*, as these cell-cell interactions have been shown to promote tumourigenesis. Finally, we investigated targeted treatment using the clinically used anti-epidermal growth factor receptor (EGFR) inhibitor cetuximab to validate the tumouroids as a suitable *in vitro* drug-screening platform.

1.5 Hypotheses under test

1. Increases in collagen type I density and concentration will enhance colorectal cancer cell migration.
2. The attachment factor and BM protein laminin will increase colorectal cancer cell migration.
3. The presence of an active stroma (the presence of fibroblasts and ECs) will enhance colorectal cancer cell migration.
4. ECs will form end-to-end vascular networks in the presence of fibroblasts in dense collagen type I gels.
5. The biomarker EGFR will be significantly upregulated in tumouroids in comparison to 2D monolayers.
6. The effect of targeted treatment of EGFR will be hindered in tumouroids in comparison to 2D monolayers.

1.6 Thesis overview

Chapter one focuses on the pathogenesis of colorectal cancer, an overview of the neovascularization process and the current 3D *in vitro* models that have been successfully utilized to date. This includes the use of multicellular spheroids, natural and synthetic scaffolds. Chapter two will focus on the general materials and methods that have been used throughout the experiments in this thesis. Chapter three focuses on controlling matrix stiffness and composition to regulate cancer invasion. This will also include investigations into the molecular mechanisms and morphological changes that contribute to an invasive phenotype. Chapter four will present the development of a primitive vascular network within the tumouroids and the influence of stromal cells on cancer invasion. Chapter five will explore the expression of

EGFR as a potential biomarker and its suitability to anti-EGFR therapy in conventional monolayer cultures and in tumouroids.

Chapter Two

Materials and Methods

2.1 Introduction

This Chapter includes a description of the general methodologies used throughout the thesis. Specific experimental protocols are outlined in the materials and methods of each respective Chapter.

2.2 Cell maintenance of cancer cells

Two colorectal cancer cell lines were used throughout this thesis. The HT29 human colorectal adenocarcinoma cell line and the HCT116 human colorectal carcinoma cell lines were obtained from the European Collection of Cell Cultures (Sigma Aldrich, Dorset, UK). Cells were routinely cultured in 2D monolayers in Dulbecco's

modified eagle medium (DMEM) supplemented with 10% fetal bovine serum (FBS), 100 units/ml penicillin and 100µg/ml streptomycin (1% P/S) (all from Invitrogen, Paisley, UK). Cells were maintained at 37°C and 5% CO_2/air.

HT29 and HCT116 cells were cultured in T75cm^2 flasks. Cells were allowed to reach 90% confluency before being passaged using a 1:5 ratio. Briefly, the medium was aspirated from the flasks before being washed once with 10ml phosphate buffered saline (PBS) (Lonza, Slough, UK). Cells were detached by incubating the flasks with 3ml of 0.25% trypsin/EDTA (Sigma) at 37°C for 5 minutes and by gently tapping on the side of the flask to ensure all the cells were floating. For neutralization, 7ml of fully supplemented DMEM was added and mixed thoroughly by pipetting up and down several times. Subsequently, 2ml was added to a fresh flask containing medium.

For experiments, cells were prepared for counting after neutralization by adding 50µl of the cell suspension and 50µl of PBS (1:2 dilution) into a fresh eppendorf tube. This was vortexed briefly (3-4 seconds) to break up any clumps of cells. Cells were counted by adding 10µl of the PBS-cell suspension into a haemocytometer. The number of cells in the four quadrants of the haemocytometer was counted and the total cell number was calculated using the following formula: $N = M \times V \times D \times 10^4$ cells/ml. M denotes the average number of cells, V the volume of medium the cells were re-suspended in and D the dilution factor (1:1 cells and PBS). The cells were then centrifuged at 1500rpm for 5 minutes. The supernatant was discarded and the cells resuspended in the appropriate volume required for experiments. Cells were used up to passage 40.

2.3 Cell maintenance of endothelial cells

Human umbilical vein endothelial cells (HUVECs) were purchased from Promocell (Heidelberg, Germany). HUVECs were cultured in 2D monolayers in complete endothelial growth medium (EGM) (Promocell, Heidelberg, Germany) supplemented with 10% fetal bovine serum and 100 units/ml penicillin and 100µg/ml streptomycin (all from Invitrogen, Paisley, UK) and maintained at 37°C and 5% CO_2/air.

HUVECs were routinely cultured in T75cm^2 flasks and were allowed to reach ~95% confluency before being passaged at a 1:4 ratio. The EGM was removed and flasks were washed once briefly in PBS-EDTA (Ethylenediaminetetraacetic acid) (Invitrogen, Paisley, UK). The cells were then detached using 3ml of 0.25% trypsin/EDTA for 2-3minutes. To ensure the cells were detached, they were checked under a light microscope and gently tapped on the side of the flask. To neutralize, 7ml of EGM was added to the flask and mixed well. 2.5ml was then added to a new flask containing medium and returned to the incubator.

For experiments, cells were trypsinized and counted as described in Section 2.1. Cells were used up to passage 5 for experiments.

2.4 Cell maintenance of fibroblasts

Adult human dermal fibroblasts (HDFs) were purchased from Invitrogen (Paisley, UK). HDFs were cultured in 2D monolayers in high glucose DMEM supplemented with 10% FBS and 100 units/ml penicillin and 100µg/ml streptomycin (all from Invitrogen, Paisley, UK) and maintained at 37°C and 5% CO_2/air. HDFs were cultured in T75cm^2 or T225cm^2 flasks depending on the number of cells required for experiments. HDFs were trypsinized, neutralized and counted as described in Section

2.1. Cells were used up to passage 12 as recommended by the manufacturer's instructions.

2.5 Fabrication of 3% matrix tumouroids

The same basic formula was used to create 3% matrix tumouroids throughout. A total volume of 4ml was prepared for the ACM comprising 3.2ml of acid soluble rat tail collagen type I (protein concentration 2.05mg/ml in 0.6% acetic acid, First Link, Wolverhampton, UK), 0.4ml 10X Minimum Essential Medium (MEM, 10X with Earle's Salts, without L-glutamine and without sodium bicarbonate, Invitrogen, Paisley, UK), 0.4ml of the appropriate colorectal cancer cell suspension at a ratio of 8:1:1. Collagen type I was mixed with 10X MEM and neutralized dropwise with 5M NaOH and then 1M NaOH to reach a pH ~7.4. Once neutralized the collagen-MEM mixture colour changed yellow to pink following gentle agitation. The cell suspension was immediately added and mixed thoroughly to ensure the cells were even distributed within the viscous collagen solution. Using a pasteur pipette, the collagen-cell solution was transferred into a mould resting on top of a glass slide with 30nm filter paper on the underside. The solution was left to compress under its own weight for 30 minutes at room temperature. The mould was then transferred to a nylon mesh resting on top of a 165µm stainless steel mesh and 30nm filter paper at the base (Figure 2.1 and 2.2). The gel was compressed under a load (weight = 175g) for 1 minute at room temperature. This compression process was also carried out for the other side of the gel to create the ACM (Figure 2.2b). The mould was removed and the resulting collagen gel (22 x 10 x10mm) was cut into 4 equal pieces (~5.5 x 10 x 10mm) using a sterile surgical knife (Figure 2.2c). A few drops of DMEM was

added to each piece and placed in the incubator. To create the acellular stromal surround, 4ml of acellular collagen was prepared as described above with 0.4ml DMEM substituted for the cell suspension. The collagen solution was pipetted (1ml was added to each well) in a 12 well plate and each ACM was nested within the collagen hydrogel and placed in the incubator for 30 minutes to initiate fibrillogenesis. Once the gel had formed, 1ml of fully supplemented DMEM was added to each well and returned to a humidified incubator set at 37°C.

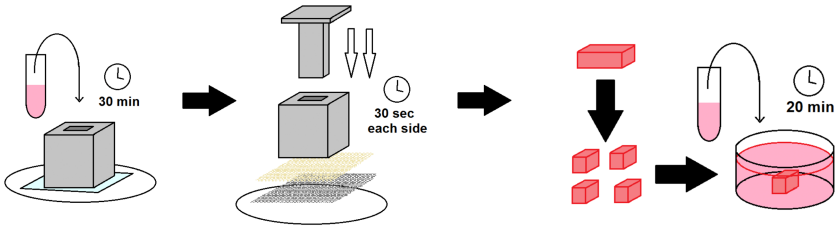

Figure 2.1: A schematic illustrating how 3% matrix tumouroids are fabricated: Collagen and 10X MEM were mixed and neutralized with 5M and 1M NaOH on ice. Once the solution was neutralized, observed by a colour change from yellow to pink, the cell suspension was added and mixed thoroughly. The collagen – cell mixture was then added into a mould and allowed to gel at room temperature for 30 minutes. A plunger (175g) was then used to compress both sides of the collagen gel for 30 seconds each. The resulting ACM, containing the cancer cells was cut into 4 equal pieces and nested into an acellular collagen hydrogel surround set in a 12-well plate for 20 minutes in the incubator set at 37ºC before 1ml of fully supplemented DMEM was added to each tumouroids to fully immerse the culture.

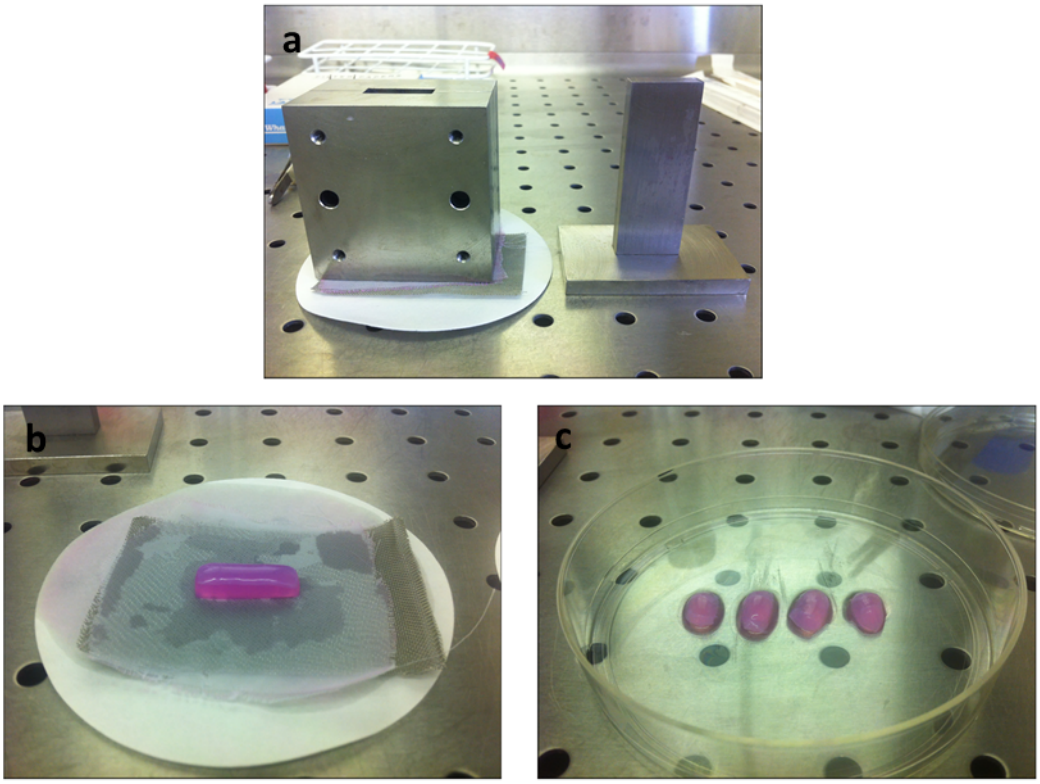

Figure 2.2: Plastic compression of a collagen gel to create 3% matrix tumouroids (a) The collagen-cell solution was added to the mould and compressed with a load (175g) for 30 seconds on each side (b) The ACM after compression on both sides (c) The ACM divided into four equal pieces.

2.6 Fabrication of 10% matrix tumouroids

High density ACMs were prepared using the RAFT™ 3D cell culture system in 96 well plates as detailed by the manufacturer's instructions (TAP Biosystems, Royston, UK). A full 96 well plate was never populated with 96 RAFT™ gels, as this was never required at once. The manufacturer's instructions detailed the different reagent volumes required to create different numbers of wells of a 96 well plate. The volumes required were pre-established in the manufacturers protocol. For example, experiments that required 10 wells, 0.3ml of 10X MEM, 2.7ml of rat tail collagen type I, 0.197ml neutralizing solution and 0.143ml cell stock solution (1.98 x 10^6 cells/ml for 20,000 cells per well or 4.96 x 10^6cells/ml for 50,000 cells per well)

were added in that order and mixed thoroughly to create a final volume of 3.4ml. From this solution, 240µl was pipetted into 10 wells in a 96 well plate and placed on a plate heater (Tap Biosystems, Royston, UK) set at 37°C for 15 minutes to initiate fibrillogenesis. While still on the plate heater, biocompatible hydrophilic RAFT™ absorbers were placed on the hydrogels and left for 15 minutes to remove some interstitial fluid to create a high density ACM. The absorbers were then removed and fully supplemented DMEM was added to each well. To create the stromal surround, acellular collagen gels were prepared as described in Section 2.5. 500µl of acellular collagen was cast in a 24 well plate and placed on a plate heater for 5 minutes at 37°C to begin gelation. Each RAFT gel was then carefully removed from the 96 well plate using a fine tip stainless steel forceps and placed on top of the collagen hydrogel. 200µl of the acellular collagen solution was then added on top of the RAFT gel to fully encapsulate it. The 24 well plate was returned to the incubator for 15 minutes to gel the stromal surround. Fully supplemented medium was added immediately after and returned to a humidified incubator set at 37°C.

2.7 Basement membrane incorporation into tumouroids

To investigate the effect of laminin on cancer cell morphology and invasion, 50µg/ml of laminin (mouse, BD Biosciences) was added to the collagen-MEM mixture prior to neutralization. This concentration was based on information from the literature[117,141,142]. Laminin was only added to the stromal surround for experiments. The stromal surround collagen-laminin hydrogel was prepared as described above by casting hydrogels in 12 or 24 well plates.

2.8 Physiological stromal surround

In order to test the effect of matrix density on cancer cell morphology and invasion, the stromal surround was compressed for a series of experiments in 10% matrix tumouroids. Collagen gels with or without laminin were prepared as described in Section 2.6. Briefly, 500µl of neutralized acellular collagen ± laminin was cast in 24 well plates and allowed to gel for 5 minutes on a plate heater (TAP Biosystems) set at 37°C. RAFT cultures were then placed on the gel before 500µl of acellular neutralized collagen ± laminin was added on top to fully immerse the RAFT construct containing the cancer cells. This was allowed to gel for 10 minutes at 37°C before being compressed for 15 minutes under biocompatible hydrophilic RAFT absorbers to produce the dense stromal component.

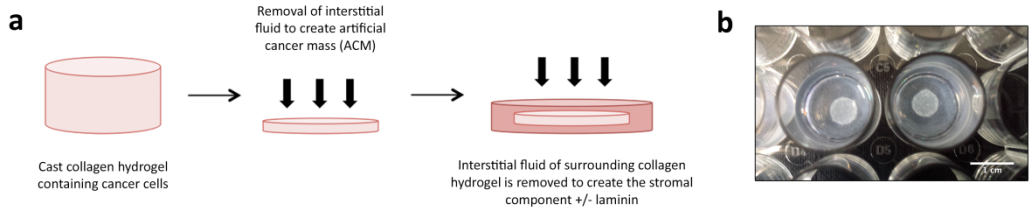

Figure 2.3: The morphological appearance of 10% matrix nested tumouroids. (a) A schematic diagram illustrating how tumouroids are made and (b) the gross appearance of the ACM containing cancer cells nested within the stromal component after 21 days in culture. Scale bar – 1cm.

2.9 ImageJ analysis

The total surface area (µm^2) of cell aggregates was measured using the ImageJ software version 1.47 (National Institute of Health, USA). All analysis was done manually. Cancer invasion was defined as cell aggregates detaching and invading the stromal surround or cell sheets growing outwards from the ACM. The freehand line tool was used to trace around the cellular aggregates and the surface are was

calculated using a pre-set scale set in ImageJ. HCT116 epithelial cell sheet invasion was measured using the straight-line tool. The furthest distance the cell sheet had migrated from the ACM was taken as a single measurement as shown in Figure 2.4.

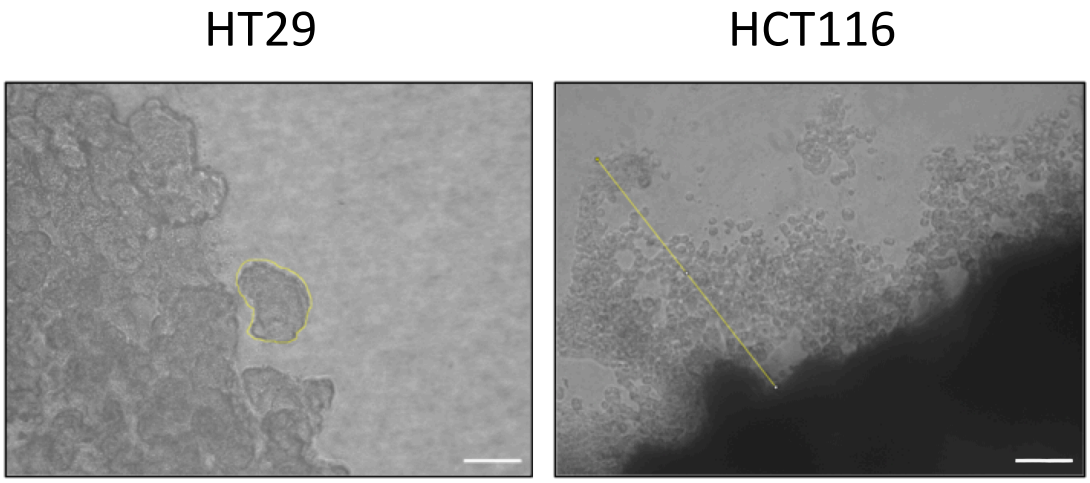

Figure 2.4: ImageJ analysis of tumouroid invasion. To quantify aggregate size and cancer invasion, the freehand line and straight-line tools of ImageJ were used to trace around HT29 cellular aggregates and HCT116 cell sheets respectively. The sizes and distances were measured and the average was calculated. Ten random aggregates or cell sheets were analyzed per well. (n=4). Scale bar – 100µm.

2.10 Statistical analysis

The data shown throughout this thesis is displayed as the mean ± standard deviation (SD) and was calculated using GraphPad Prism 6 software (GraphPad, San Diego, CA). Statistical analysis was carried out on original data values where the data was converted to percentages. Data points (n numbers) are displayed for each respective experiment in the figure legend. Data comparisons for two sets of data were analyzed for statistical significance by Students T-test analysis. Vascular network analysis among different groups was carried out using one-way analysis of variance (ANOVA) followed by post hoc analysis using Tukeys multiple comparisons test.

Drug treatment experiment datasets were analyzed using ANOVA followed by post hoc analysis using Dunnett's test. Significance was taken at $p<0.05$.

Chapter Three

Colorectal cancer cell morphology and invasion

3.1 Introduction

Understanding the more complex mechanics of tumour cell migration within conventional 2D *in vitro* models has proved challenging. As a result, there has recently been an increase in tissue engineered solutions to address this problem. One avenue, not often explored within 3D *in vitro* models, is the effect of the tumour stroma on cancer growth and invasion.

We previously described the development of a novel 3d *in vitro* model of colorectal cancer (tumouroid) based on the removal of interstitial fluid in collagen hydrogels[143–145]. Our tumouroid model is spatially accurate. It is based on a dense ACM which contains colorectal cancer cells, nested within a collagen hydrogel that represents the tumour stroma. Although, tumouroids are formed entirely with

collagen type I, we also added the basement membrane (BM) protein, laminin, to the stromal component to investigate the effects on cancer invasion.

The aim of this Chapter was to characterize the effect of matrix composition and matrix density on cancer cell morphology and invasion both within the cancer mass and within the stroma. Providing further insight into the effect of matrix density and composition on cancer cell migration particularly, investigating the onset of EMT and subsequent invasion of cells could open up a new avenue of therapeutics that targets not only the cancer cells but also the adjacent tumour stroma.

The effect of matrix density on cancer cells cultured in two ACMs of different densities was also investigated. Section A in this Chapter relates to preliminary work carried out on 3% matrix tumouroids nested in 0.2% matrix collagen gels using both HT29 and HCT116 cell lines. Section B describes HT29 and HCT116 cell behaviour in 10% matrix tumouroids nested in both stromal matrices of 0.2% and 10% collagen. The effects of the BM extract, laminin, on cancer cell invasion were also investigated in both stromal surrounds.

3.2 Materials and Methods

3.2.1 Cell Maintenance

The colorectal cancer cell lines HT29 and HCT116 were routinely cultured as described in Chapter 2. Cells were maintained routinely in culture and appropriate cellular concentrations were prepared for the experiments described below.

3.2.2 Collagen gel density measurement

The density of collagen gels was assessed using the freeze-drying method. Acellular

collagen gels were prepared and compressed under various weights as described in Section 2.5 and 2.6. Collagen gels (uncompressed), partially compressed gels (compressed with 175g weight for 1 minute) and fully compressed gels (removal of interstitial fluid using RAFT hydrophilic absorbers for 15 minutes). Once the gels were prepared, DMEM was added to each sample for 24 hours to accommodate a bounce back effect from the collagen gels (reabsorption of fluid). The gels were then washed with phosphate buffered saline (PBS, Sigma Aldrich) followed by a thorough wash in distilled water in until all the salts within the gel were removed. This was estimated by a colour change of the collagen gel from pink to colourless. The gel weight was then measured using a balance to calculate the wet weight of the gel. Each gel was then frozen at -20°C for 1 hour before being freeze-dried overnight and the weight of the dry gels was measured again. The difference between the wet and dry weights was then used to calculate the overall collagen content within the gels once the water had been removed.

3.2.3 Proliferation assay

The alamarBlue assay was used to assess proliferation in 3% and 10% matrix tumouroids. AlamarBlue measures the chemical reduction of resazurin to resorufin by mitochondrial activity and provides an indicator of metabolic activity. This metabolic activity was taken as an indicator of cell proliferation within the tumouroids. AlamarBlue was diluted 1:10 in phenol red free media and added to each well. Plates were covered in tin foil, as alamarBlue is photosensitive and placed in an incubator set at 37ºC, 5% CO_2/air for 4 hours. Following incubation, 100µl of solution in each well (n=4) was transferred to a blank 96 well plate (Nunc,

Loughborough, United Kingdom). The absorbance was recorded at excitation 530nm and emission 620nm.

3.2.4 Haematoxylin and Eosin staining

Haematoxylin and eosin (H&E) staining was used to evaluate cell morphology, proliferation and migration. 3% matrix tumouroids were cultured for up to 21 days and fixed on days 1, 7, 14 and 21 in 10% formalin for 1 hour at room temperature. The samples were then washed with PBS three times for 5 minutes each and dehydrated through increasing alcohols and chloroform in an automated tissue processor (Shandon Citadel 2000TM Tissue Processor, Ramsey, Minnesota, USA) overnight for paraffin wax embedding. Dehydrated samples were then placed in metal moulds and filled with paraffin wax and set on a cold plate overnight to solidify. Paraffin wax embedded sections were cut (10μm thick) using a microtome and dipped in 20% ethanol before being placed in a hot water bath set at 37ºC to soften the wax. Microscope slides were used to lift the sections out of the water bath and left to dry on a rack at room temperature overnight. Prior to staining, the microscope slides were placed in an oven set at 60ºC for 20 minutes to soften the wax. The following procedure for staining was carried out (Figure 3.1) and slides were then mounted with coverslips using DPX mounting media and imaged using an EVOS XL Core Cell Imaging System (Life Technologies).

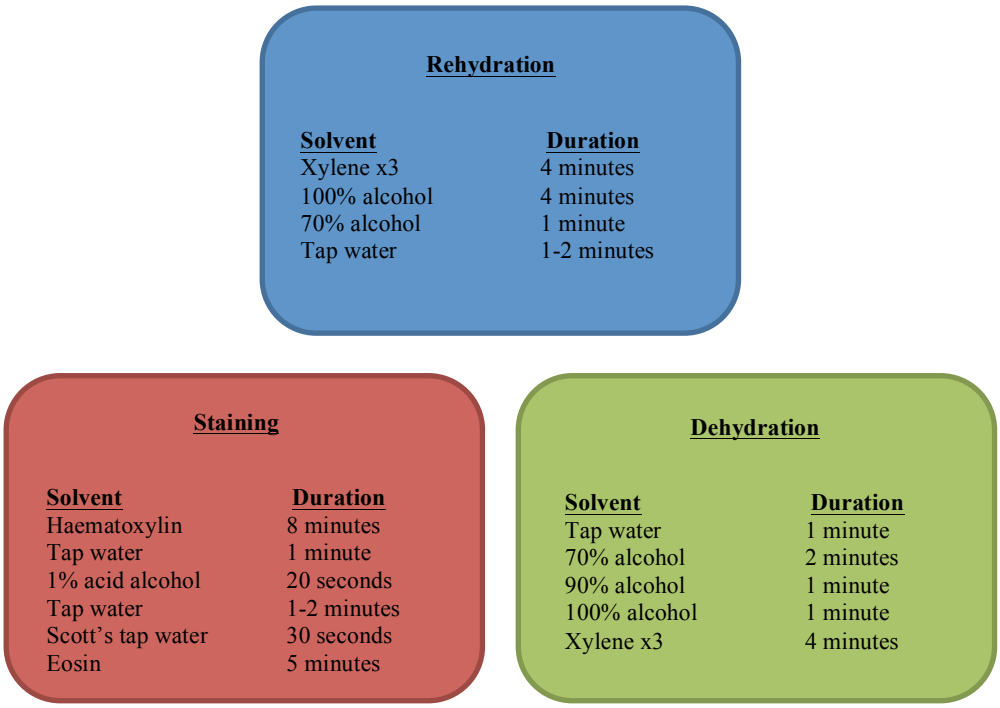

Figure 3.1: The rehydration, staining and dehydration process involved in haematoxylin and eosin staining.

3.2.5 Immunofluorescence

Immunofluorescent staining of tumouroids was carried out using a slightly modified protocol that was previously established[144]. Briefly, collagen gels were fixed in 10% formalin for 1 hour and washed three times for 5 minutes with PBS. The gels were then permeabilised with 0.2% Triton X-100 (TX-100, Sigma) for 30 minutes and washed with PBS (3 x 5 minutes). Each gel was then incubated with a Rhodamine Phalloidin conjugated to an Alexa Fluor 488 fluorescent antibody (Life technologies) for 1 hour at room temperature. The samples were then washed in PBS thoroughly and Hoechst 33342 was added to counterstain the cell nuclei. The gels were then imaged using an EVOS FL imaging microscope (Invitrogen).

3.2.6 Protein extraction and quantification

For 2D cultures, HT29 or HCT116 cells were plated on 6 well plates at a density of 300,000 and 250,000 cells per well. The plates were then placed on ice and washed with PBS twice. For 3D cultures, collagen gels were washed with PBS twice and digested with collagenase type I (Invitrogen) at a concentration of 500 units/ml for 1 hour. The sample was pipetted up and down to help speed up the degradation process. Once the gel was visibly degraded, the cells were then removed, resuspended in FBS supplemented DMEM to neutralize the collagenase and centrifuged at 377G for 5 minutes to create a cell pellet. Cells were lysed with 250µl of RIPA lysis buffer (Sigma) containing 1x protease inhibitor (Sigma). Cells cultured in 6 well plates were lysed within the plate and the supernatant subsequently transferred to 1.5ml eppendorf tubes. Protein concentration was calculated using the Pierce™ Modified Lowry Protein Assay Kit (Thermo Scientific) using a bovine serum albumin (BSA) standard curve according to the manufacturers protocol. Each standard and protein sample was measured at 750nm using Genova Plus Spectrophotometer (Jenway).

3.2.7 Sodium dodecyl sulfate polyacrylamide gel electrophoresis (SDS-PAGE) and Western Blot

Equal amounts of protein (35µg) were calculated in a final volume of 30µl. The loading dye was prepared by mixing 1.2µl of β-Mercaptoethanol and 8.8µl of 4 x Sample Buffer per sample. 10µl of the loading dye was mixed to each sample thoroughly to ensure it was mixed well before being heated at 95°C for 5 minutes to denature the samples. 15µl of the SeeBlue Plus2 Pre-stained protein standard

(Invitrogen) was added as a protein ladder and 40µl of each sample containing the loading dye was added to each well. SDS-PAGE gels were run at 150V for 60 minutes and proteins transferred to PVDF (Polyvinylidene fluoride) membranes at 30V for 90 minutes.

Membranes were blocked for 30 minutes in 2.5% BSA and 0.05% Tween 20 in PBS. Antigens were detected using mouse monoclonal antibodies against MMP-7 and vimentin (both at 1:1,000, Santa-Cruz Biotechnology, Santa Cruz, CA) and incubated with a goat anti-mouse IgG-HRP (Santa Cruz) secondary antibody at room temperature for 30 mins. Blots were developed using the Clarity™ Western ECL Substrate (Bio-Rad, Hertfordshire) and visualized using the ChemiDoc™ XRS+ System (Bio-Rad).

3.3 Results

Section A

3.3.1 Collagen gel density measurement

The matrix density of collagen gels was evaluated by freeze-drying acellular collagen gels under a variety of methods which remove the interstitial fluid within the gels. Partially compressed gels were prepared as described previously (Section 2.5) and were compressed with a 175g weight for a total of 1 minute. Partial compression of the collagen gels revealed a 13-fold increase (2.63% ± 0.32%) in collagen density in comparison to standard uncompressed collagen gels (0.2%) ($p < 0.05$) (Figure 3.2). Fully compressed gels were prepared by compressing the collagen gels with a 175g weight for a total of 10 minutes. Full compression using this method revealed a 35-fold increase in collagen density (6.98% ± 1.24%) in comparison to collagen hydrogels. The removal of fluid in fully compressed gels was also carried out for 15 minutes under hydrophilic RAFT absorbers, which absorbs the interstitial fluid to create a dense collagen matrix. RAFT absorbers produced a matrix with a 48-fold increase in collagen density (9.59% ± 1.28%) ($p < 0.05$) in comparison to uncompressed collagen gels. From this point, partially compressed gels and RAFT gels will be referred to as 3% and 10% matrix respectively. The protein concentration of uncompressed collagen gels, partially compressed gels, fully compressed gels and RAFT gels was 2.04mg/ml, 26.52mg/ml, 71.4mg/ml and 97.81mg/ml respectively.

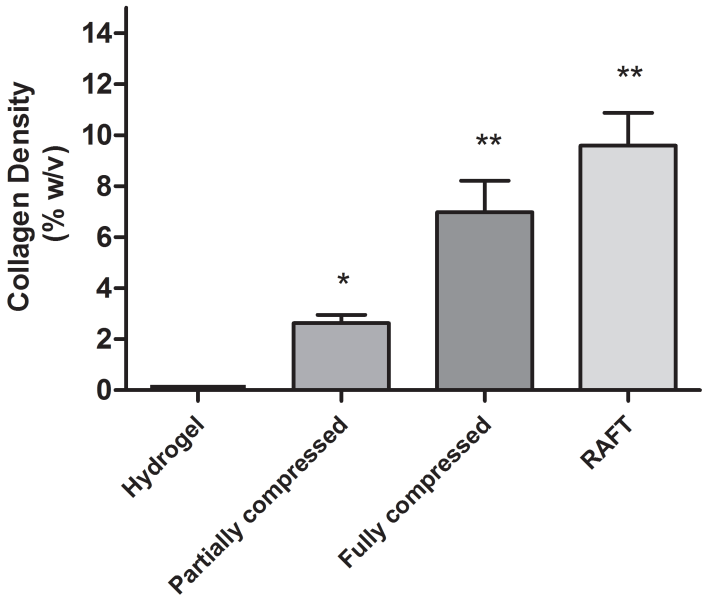

Figure 3.2: Collagen density of acellular gels. Matrix densities (mean ± SD) of collagen gels under various compressions as a % w/v. (n=4) *$p < 0.05$; **$p < 0.0001$.

3.3.2 Colorectal cancer cell proliferation and morphology in 3% matrix tumouroids

The proliferation rate of HT29 and HCT116 cells was tested in 3% matrix tumouroids over a 14-day period. To assess the proliferation profile of cells cultured in 3D, the alamarBlue assay was used. The advantage of using the alamarBlue assay lies in the fact that the assay is non-toxic and therefore the same construct can be measured on a timescale. The optimum cell density for 3% matrix tumouroids has been established previously[145]. Both HT29 and HCT116 cell lines were cultured in 3% matrix tumouroids at a density of 1.6 x 10^6 cells/ml (to make up a total of 4ml). HT29 cells cultured in 3% matrix tumouroids displayed no significant increase in proliferation over the 14-day period (Figure 3.3), as the cells appeared to slow down metabolically. However, HCT116 cells had a much higher proliferation profile in comparison to HT29 cells. Interestingly, while the overall growth pattern of HCT116 cells increased over 14 days, there was a significant drop in the proliferation readings at day 7 indicating a state of cellular quiescence. By day 7 and significantly more so by day 14, cells aggregated together to form spheroid like structures in both HT29 and HCT116 cells (Figure 3.4a) On day 21, HT29 cells formed aggregates that were 31,337.6μm^2 ± 9438.8μm^2 and HCT116 cells formed aggregates that were 34,791.2μm^2 ± 9378.4μm^2 (Figure 3.4b). It is interesting to note that although aggregates formed 3D cellular structures, the quantification of these structures was carried out in two-dimensions. The surface area of the largest area was measured and taken as an indicator of growth over time. This is because volumetric measurements were difficult to quantify using microscopy.

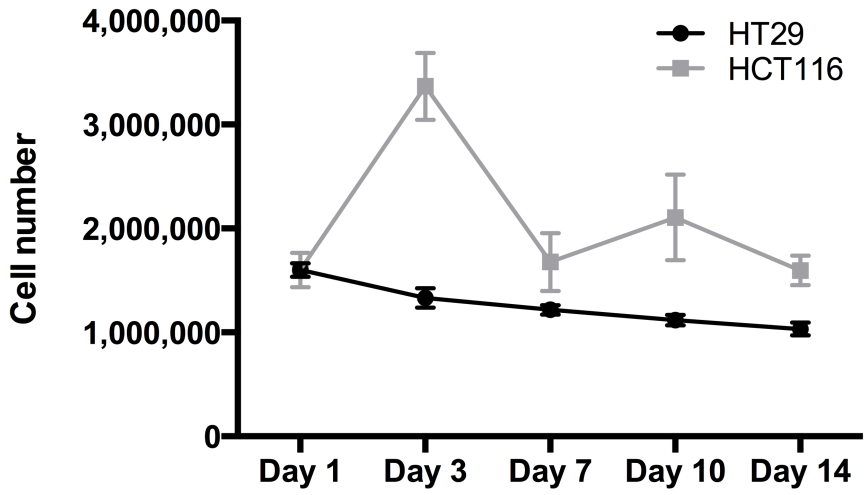

Figure 3.3: Growth kinetics of colorectal cancer cells cultured in 3% matrix tumouroids. The alamarBlue assay was used to measure the metabolic activity of HT29 and HCT116 cells over a 14-day period. Data is presented as mean ± SD (n=4).

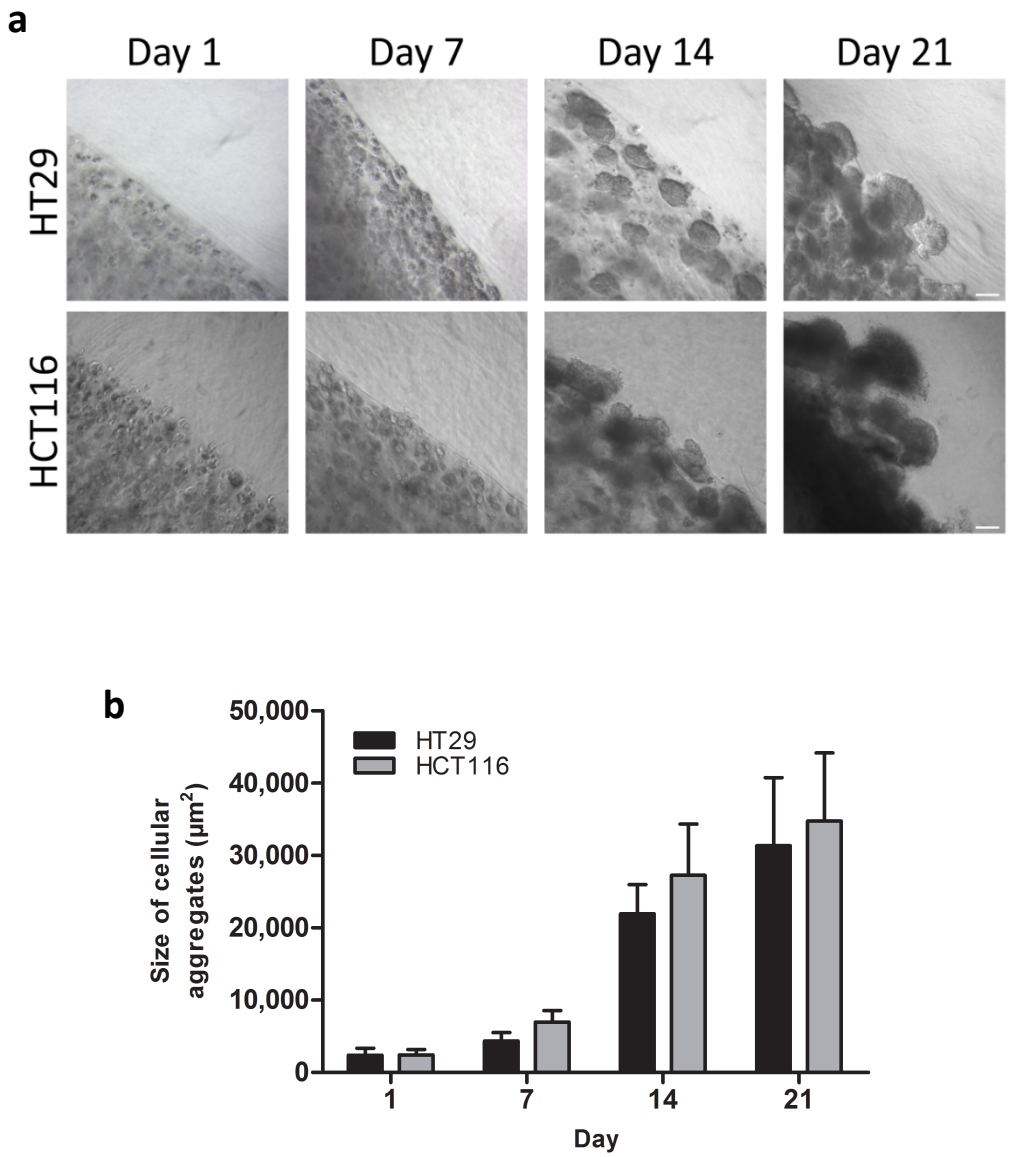

Figure 3.4: Cell morphology of colorectal cancer cells in 3% matrix tumouroids. (a) Bright field microscope images at the interface between the ACM and the stromal surround over a 21 day period. (b) Quantification of the size of HT29 and HCT116 aggregates as measured by ImageJ of 10 random cellular aggregates (n=4). Data is presented as mean ± SD. Scale bar – 100μm.

3.3.3 The morphology of invading cancer cells from the ACM is cell specific

H&E staining was used to analyze cell distribution and the morphology of colorectal cancer cells within the ACM of 3% matrix tumouroids for HT29 and HCT116 cells. H&E stains the cell nuclei blue and can distinguish cells from the collagen matrix by staining the matrix pink.

Histological analysis of HT29 and HCT116 tumouroids revealed an equal distribution of cells throughout the ACM at day 1 (Figure 3.5). By day 7, cells had formed small aggregates of cells similar to those observed using light microscopy in Figure 3.4a. However, all of the larger aggregates were localized to the boundary between the ACM and the surrounding stroma. Increasingly, by day 14, HT29 cell aggregates had invaded out of the ACM as aggregates whereas HCT116 formed dense cell sheets. After 21 days, it was evident that the invasion profile of each cell line was significantly different from each other with HT29 cells remaining as aggregates within the ACM and the surrounding stroma whereas HCT116 cells, which still formed aggregates in the ACM, invaded exclusively as cell sheets.

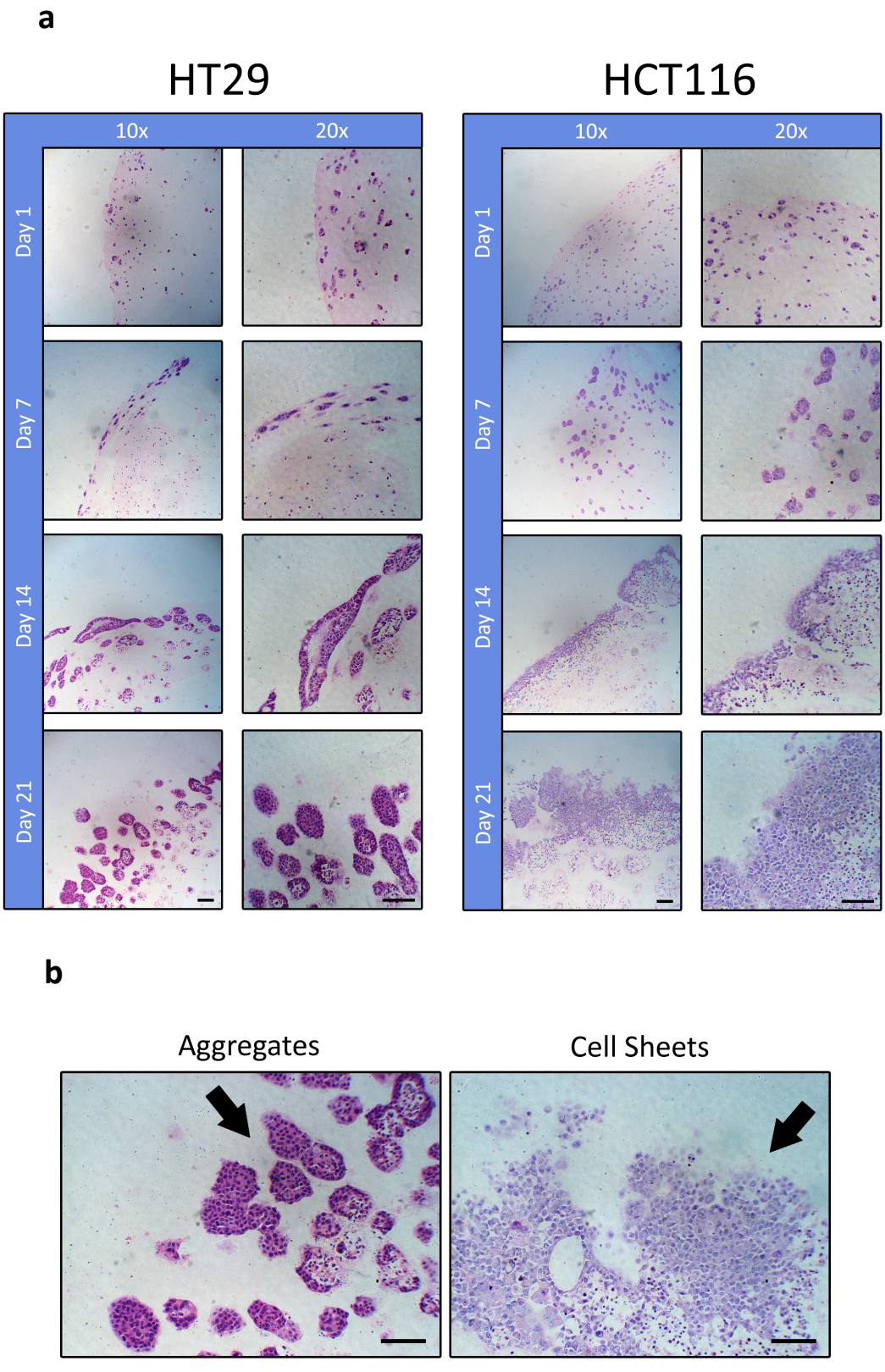

Figure 3.5: Morphology of colorectal cancer cells in 3% matrix tumouroids. H&E staining was used to evaluate cell distribution, morphology and cancer invasion in 3% matrix tumouroids. (a) HT29 cells and HCT116 migrated towards the edge of the ACM by day 1 which increased by day 7. Both cell lines formed cellular aggregates by day 7 which were mostly localized to the interface between the ACM and the acellular stromal surround. At day 14, HT29 cells invaded into the stroma as

aggregates while HCT116 invaded as cell sheets. By day 21 there was a marked presence of HT29 cellular aggregates and HCT116 cell sheets in the stromal surround. (b) Higher magnification images of the ACM stromal interface. Black arrows represent invading HT29 aggregates and HCT116 cell sheets. Scale bars – 100μm.

3.3.4 Cancer invasion in 3% matrix tumouroids

The invasive capacity of HT29 and HCT116 cells in 3% matrix tumouroids was further established using bright-field microscopy. This was carried out to evaluate the migration of cells in real time. HT29 and HCT116 cell invasion was observed at day 12 and day 11 respectively with prominent invasion shown at day 14 (Figure 3.6a). HT29 cells invaded from the ACM as spherical cellular aggregates. The distance of aggregate invasion was then quantified using the ImageJ software. There was no statistically significant difference in the distance of invaded aggregates between day 14 and day 21. However, while the distance was not significant, the size of the aggregates increased over time indicating that the aggregates continued to proliferate in the stromal surround at a much faster rate than within the ACM (Figure 3.6a). The addition of laminin did not appear to enhance the size or the distance of the invaded aggregates in the stromal surround. HCT116 cells, which also formed aggregates within the ACM invaded as epithelial cell sheets contiguous from the ACM. Over time, secondary cell sheets were observed to detach from the primary invading cell sheet and form and continue to proliferate within the stromal surround (Figure 3.6b). Although it was not statistically significant, laminin slightly increased the overall distance migrated of the cell sheets in comparison to the collagen only stromal surround.

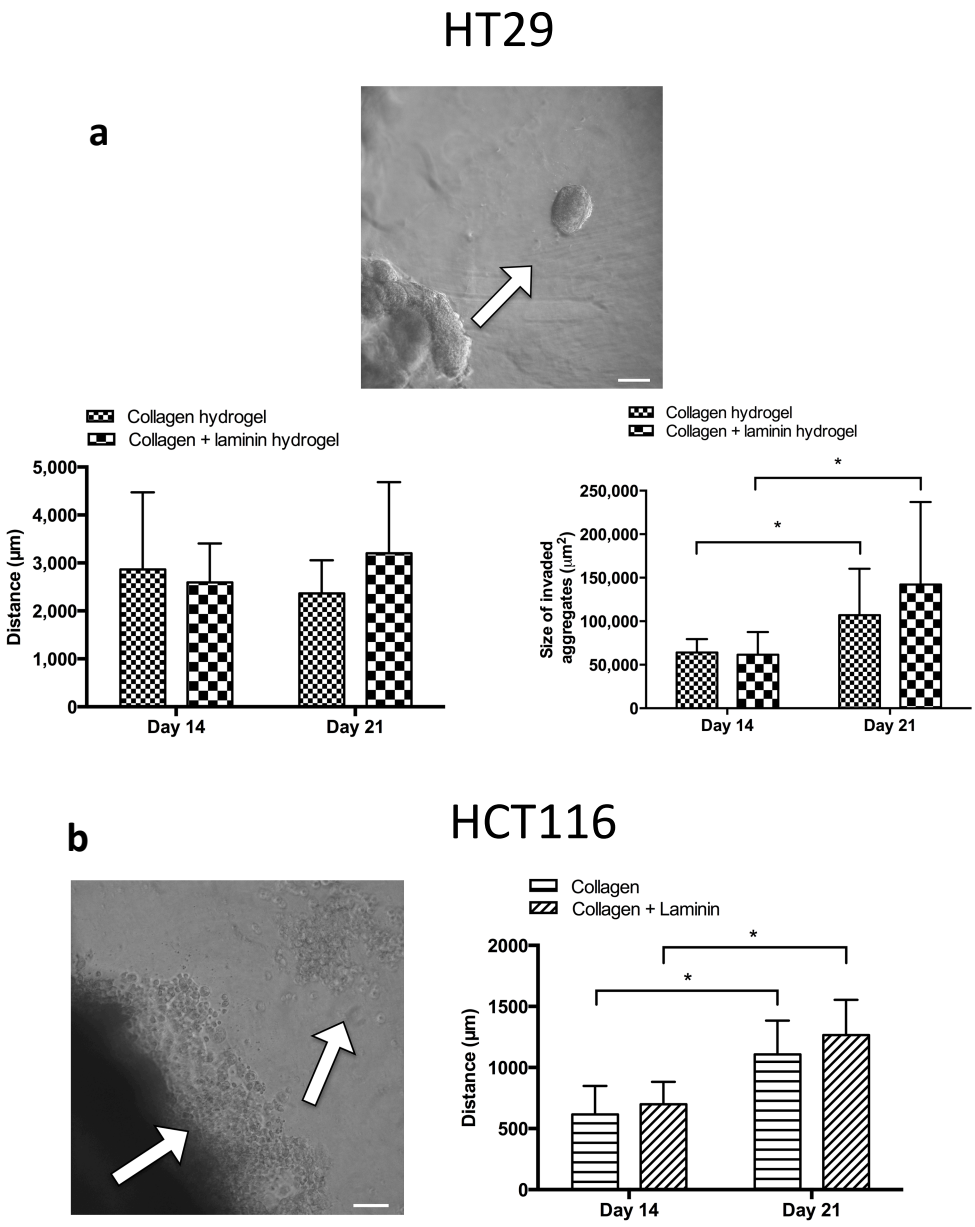

Figure 3.6: Invasive profile of colorectal cancer cells in 3% matrix tumouroids. (a) Phase contrast images of HT29 cancer cells invading as a cell aggregate from the ACM into the stromal surround. Quantification of the distance travelled by the invading HT29 aggregates from the ACM and the average size of the aggregates both in a collagen only stromal surround and a collagen + laminin stromal surround. (b) Phase contrast images of HCT116 cancer cells invading as an epithelial cell sheet, forming secondary cell sheets, within the stromal surround. The total distance migrated of the cell sheet from the ACM was also quantified in collagen and collagen and laminin gels. Data is presented as the mean ± SD. * $p < 0.05$. Scale bars – 100µm.

3.4 Results

Section B

3.4.1 Colorectal cancer cell morphology in 10% matrix tumouroids

The proliferation profile of HT29 and HCT116 cells was also measured in 10% matrix tumouroids that were cultured at a density of 2 x 10^4 cells per well. These differences in cell number are due to the volumetric differences taken into consideration between 3% and 10% matrix tumouroids.

In 10% matrix tumouroids, HT29 cells displayed a steady increase in metabolic activity that appeared to plateau at day 14 (Figure 3.7). Morphologically, the size of the cellular aggregates grew in size in line with the proliferation measurements. Similarly to 3% matrix tumouroids, HCT116 cells cultured in a 10% matrix displayed a drop of metabolic activity by day 7. Conversely, bright field microscope images (Figure 3.8a) of HCT116 aggregates showed no decline in growth between day 3 and day 7; therefore any state of biochemical quiescence did not result in any associated decrease in aggregate size. On day 21, HT29 cells formed aggregates of 32,565.2μm^2 ± 5993.4μm^2 and HCT116 cells formed aggregates of 35,847.8μm^2 ± 5536.8μm^2 (Figure 3.8b). Overall, HCT116 cells formed slightly larger aggregates than HT29 cells in 10% matrix tumouroids; however this appeared to follow a trend, which was not statistically significant.

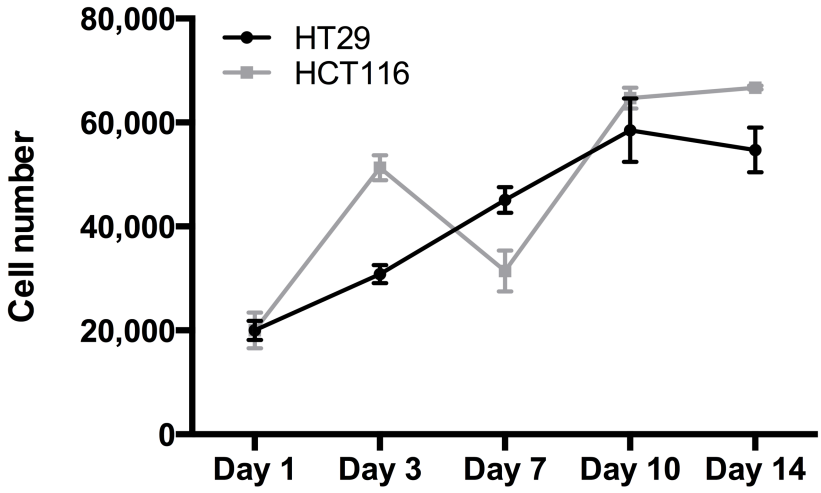

Figure 3.7: Growth kinetics of colorectal cancer cells cultured in 10% matrix tumouroids. The alamarBlue assay was used to measure the metabolic activity of HT29 and HCT116 cells over a 14-day period. Data is presented as the mean ± SD (n=4).

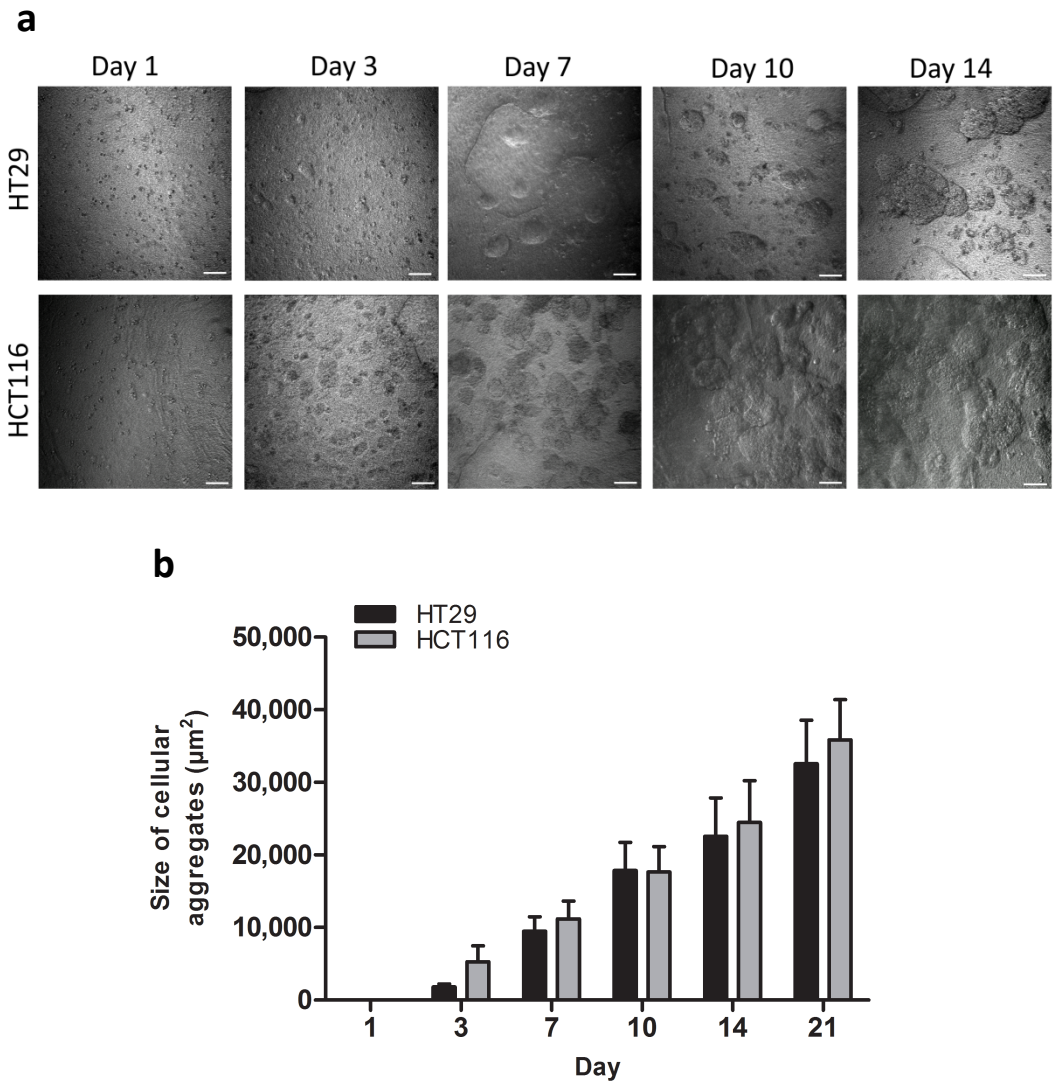

Figure 3.8: Cell morphology of colorectal cancer cells in 10% matrix tumouroids. (a) Phase contrast images of HT29 and HCT116 cells cultured in 10% matrix tumouroids over a 14-day period. Single cell proliferate and migrate to form cellular aggregates. (b) Quantification of the size of the cellular aggregates as measured by ImageJ of 10 random cellular aggregates (n=4). Data is presented as mean ± SD. Scale bar – 50µm.

3.4.2 Extracellular matrix density and composition of the stroma regulates cancer cell invasion

During the metastatic cascade, cancer cells must first detach from the primary tumour site where they invade the surrounding stromal tissue and adjacent parenchyma. Subsequently, cancer cells then break through the basement membrane where they enter the circulating blood flow and travel to distant organs. The aim of these experiments was to examine the influence of cell-matrix interactions on the migration of cancer cells. We investigated the effect of incorporating the basement membrane protein laminin and increasing matrix density of the stromal surround on cancer cell invasion. This was demonstrated in 10% matrix tumouroids which have a much stiffer ACM than partially compressed tumouroids (see Figure 2.2).

Similarly to the 3% matrix tumouroids shown in Figure 3.6a, HT29 cells invaded as cellular aggregates in 10% matrix tumouroids (Figure 3.9ai). They also detached from the ACM as they invaded and migrated into the stromal surround. The addition of the attachment factor and basement membrane component laminin, also increased the size of the invaded aggregates at day 21 between collagen only (56,615.9μm^2 ± 28,792.6μm^2) and collagen + laminin cultures (253,564.6μm^2 ± 115,601.8 μm^2) (Figure 3.9b) ($p<0.05$). Again, similar to 3% matrix tumouroids there was no correlation between the distance migrated by aggregates between day 14 and day 21 (Figure 3.9c). When the collagen density of the surrounding stroma was increased from 0.2% to 10% collagen, HT29 cells began to form additional migratory patterns. While cellular aggregates were still distinguishable within the stroma, contigous cell sheets also invaded from the ACM (Figure 3.9aiii). Invaded aggregates displayed a trend of migrating further in the dense stromal surround in comparison to standard uncompressed collagen gels (Figure 3.9c), however this was not statistically significant.

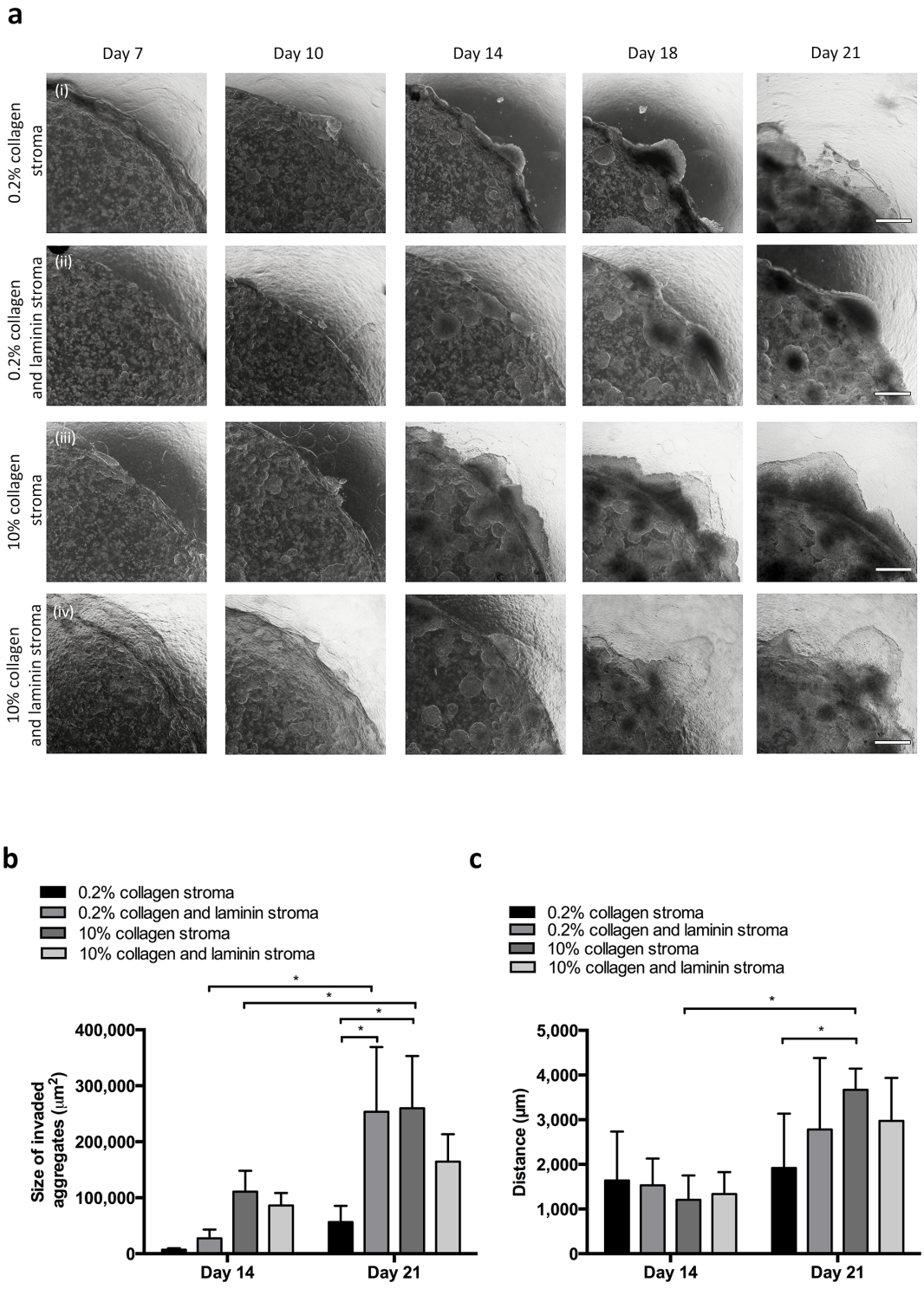

Figure 3.9: Matrix density changes cancer cell invasion in HT29 tumouroids. (a)i HT29 cells cultured in a 10% collagen matrix invade into a collagen hydrogel only stromal surround and a (ii) collagen and laminin hydrogel stromal surround. (iii) HT29 cell invasion switches to an epithelial cell sheet in a stiff stromal surround and (iv) invasion is enhanced when laminin is added to the stromal surround. (b) Quantification of size of invaded aggregates and (c) the distance that aggregates invaded into each respective stromal surround. (n=6). Data is presented as mean ± SD. * $p < 0.05$. Scale bar – 500μm.

HCT116 cells, which are the more metastatic than HT29 cells[146], invaded exclusively as epithelial cell sheets (Figure 3.10a) under all stromal conditions. The addition of laminin to the stromal cultures increased the overall migration distance of the epithelial cell sheets between day 7 and day 21 in comparison to collagen only stromal surrounds (Figure 3.10b) Interestingly, when the distances of cell sheet invasion were quantified in different stromal surrounds, highly different patterns of the rate of invasion were observed. In the low density collagen stroma, the invasion of the cell sheets appeared slow at first, however between day 10 and day 21, the rate of invasion increases in a linear fashion. On the contrary, the invasion pattern of HCT116 cells migrating into a dense stromal surround was earlier than the low-density stroma (Table 3.1). Conversely, at day 14, HCT116 cell sheet invasion appears to slow down significantly until day 21 where the presence of laminin appears to be the major driving factor in enhancing the total distance migrated (Figure 3.10c).

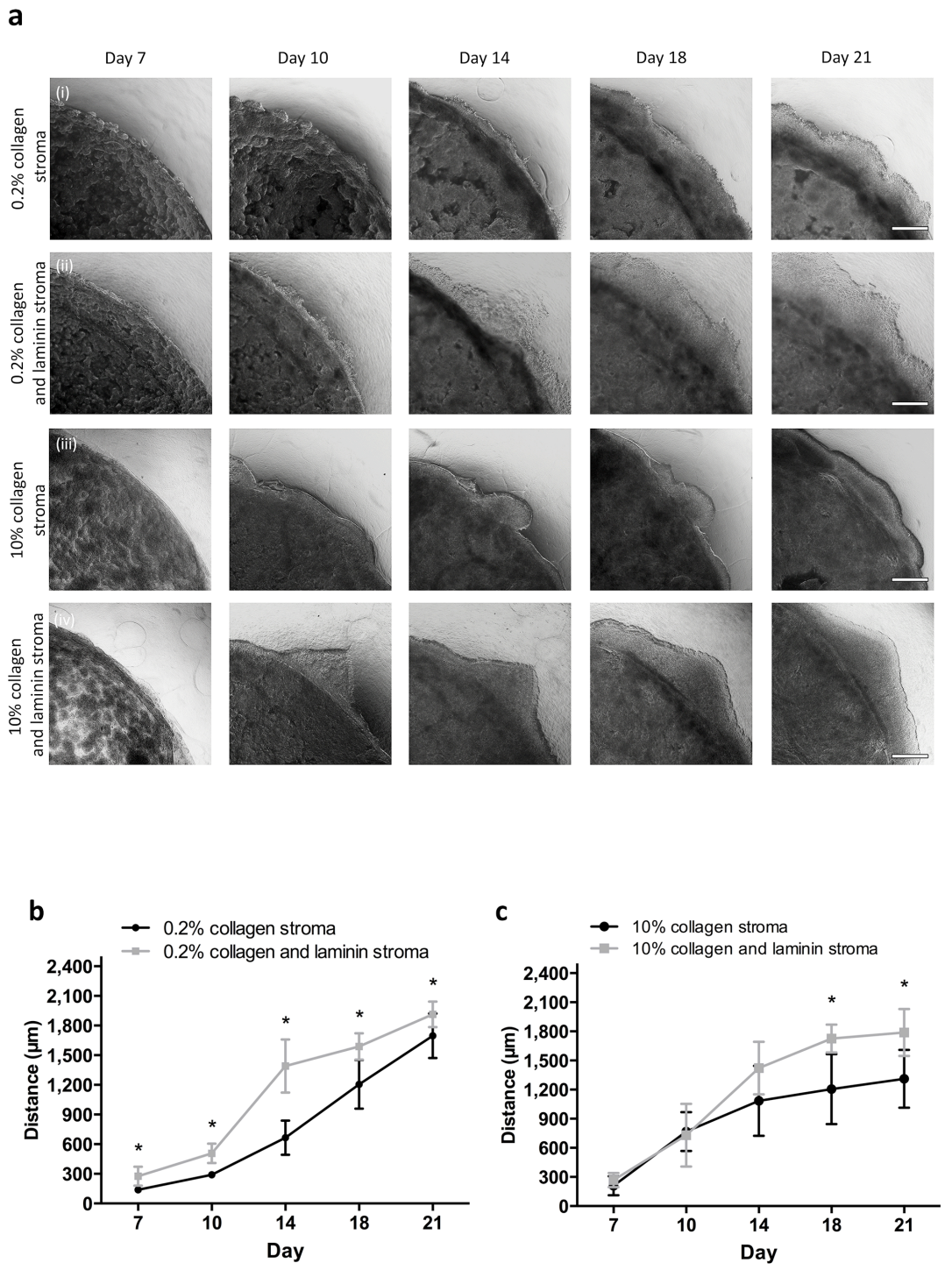

Figure 3.10: HCT116 cancer cell invasion rate is dependent on collagen density. (a)i HCT116 cells cultured in a 10% collagen matrix invade into a collagen only hydrogel stromal surround (ii) and a collagen and laminin hydrogel stromal surround as cell sheets. (iii) HCT116 cells invading into a collagen only stiff stromal surround and (iv) enhanced invasion when laminin is added. (b) Quantification of the total distance of invasion of HCT116 cells into a collagen and collagen/laminin hydrogel (0.2% collagen) and (c) a stiff (10% collagen) stromal surround with or without laminin by ImageJ. Ten random cell sheets were measured from the ACM to the furthest point. (n=6) Data is presented as mean ± SD. * $p < 0.05$. Scale bar – 500µm.

Stromal surround composition	Day of invasion	
	HT29	HCT116
0.2% collagen matrix	Day 11	Day 7
0.2% collagen + laminin matrix	Day 10	Day 5
10% collagen matrix	Day 10	Day 6
10% collagen + laminin matrix	Day 10	Day 5

Table 3.1: The invasion profile of HT29 and HCT116 cells into different stromal conditions.

3.4.3 Morphological changes in invading leader cells

The invasive capacity of HT29 and HCT116 cells was also characterized in a dense (~10% collagen) stromal surround. Both cell lines used thus far were highly invasive, particularly the HCT116 cells which invaded earlier than HT29 cells in all conditions (Table 3.1). The aim of these experiments was to investigate the morphology of the invading 'leader' cells, which appeared elongated and morphologically distinct from the cells that seemed to follow.

Interestingly, as the cells begin to invade the stromal surround, HT29 cells display three different morphologies whereas HCT116 cells displayed only two (Figure 3.11). However, this was not visible by the light microscope images in Figure 3.9 and 3.10 and was confirmed by the immunofluorescent staining of the actin filaments (phalloidin). Although the location and morphology of the invading cells appeared random and unsystematic, there were distinguishable features to each pattern. In some instances, HT29 cells protruded outwards from the ACM into the stromal surround and formed polarized organized structures as evident by the coordinated one-directional organized migration of the invading cell sheet (Figure 3.11a). It is worthwhile mentioning that these dense collagen scaffolds were not aligned prior to

these experiments and that collagen fibers would have a random non-aligned orientation.

On the other hand, invading HCT116 cell sheets had no structured organization and the migration appeared to random and in all directions (Figure 3.11b). Moreover, the morphology of the cells at the front of the invading sheets differed greatly from those comprising the bulk of the cell sheet. These leader cells were particularly elongated for both HT29 and HCT116 cell lines, and appeared morphologically distinct from the cells in of the ACM (Figure 3.11c, e) Moreover, HT29 cells also formed cellular aggregates, which invaded the surrounding stroma (Figure 3.11e). This feature was again, entirely absent from HCT116 tumouroids.

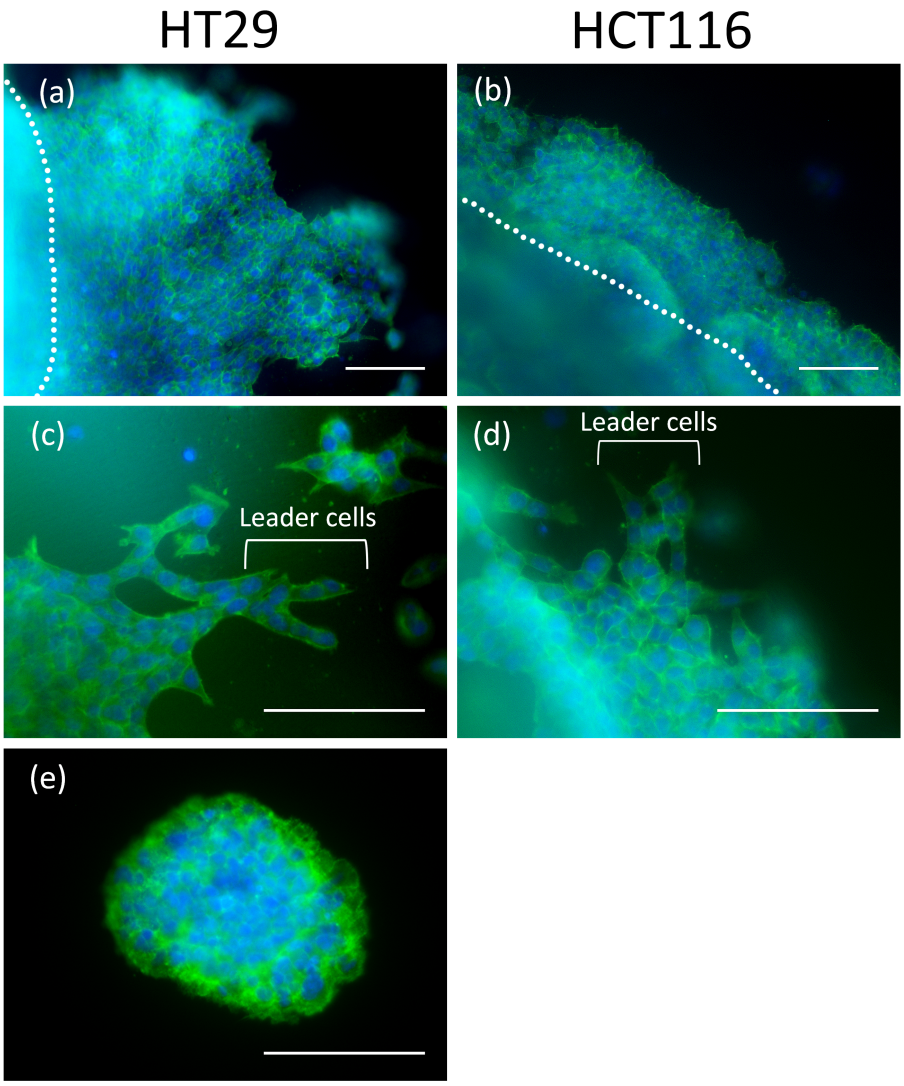

Figure 3.11: Different morphologies of invading cell sheets and aggregates in a dense collagen stroma. HT29 and HCT116 cells invading into a 10% collagen matrix containing laminin after 14 days in culture were fixed and stained for F-actin (green - phalloidin). Nuclei were stained with DAPI (blue). (a) HT29 cells invading as organized polarized cell sheets into a single direction whereas (b) HCT116 invasion was disorganized and was observed to migrate in all directions. The dotted line represents the border between the ACM and the stromal surround. The presence of elongated leader cells (c, d) at the invading edge of both HT29 and HCT116 cell sheets. (e) A single invaded HT29 aggregate in the stromal surround. (n=6). Scale bars - 100µm.

3.4.4 Induction of EMT corresponds with extracellular matrix remodeling

In order to validate phenotypic changes associated with cancer cell invasion, we examined the presence of EMT and MMP expression involved in ECM degradation. Western blotting was used to detect the expression patterns of MMP7 and the EMT marker vimentin between cells cultured in 2D and in tumouroids (Figure 3.12). MMP7 overexpression has been linked to an increased incidence of metastasis and advanced disease in colorectal cancer[51,147]. Although, MMPs are typically expressed by stromal cells, MMP7 was chosen due to its previously established expression exclusively by carcinoma cells[148]. MMP7 is the smallest member of the MMP family and is involved in the degradation of a host of ECM proteins including fibronectin, collagen IV and various proteoglycans[149]. Two versions of MMP7 exist, pro-MMP7 and an active MMP-7. Similarly to all MMPs, pro-MMP7 is converted to the active MMP-7 form via various extracellular proteases and plasmins[150].

Densitometry analysis revealed vimentin expression was highly upregulated in both HT29 and HCT116 tumouroids in comparison to their monolayer counterparts (fourfold and twofold respectively). The expression level of active MMP7 in HT29 cells was four times higher in tumouroids than in 2D. On the other hand, HCT116 tumouroids and 2D monolayers did not illustrate a dramatic difference in active MMP7 expression.

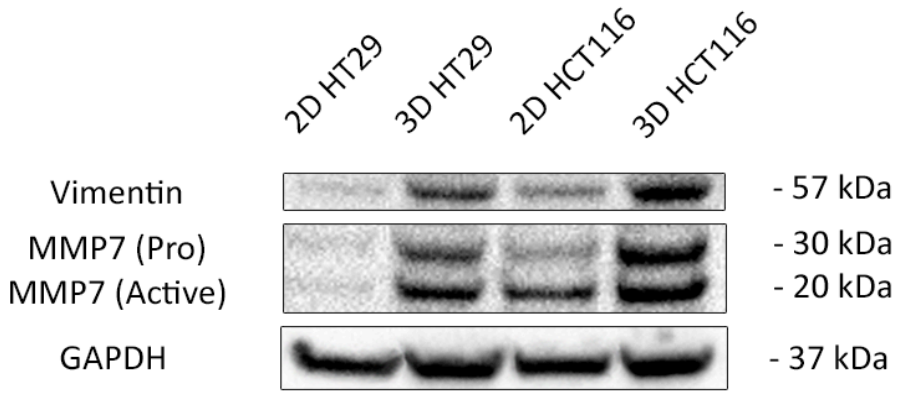

Figure 3.12: Expression of invasive and EMT markers in colorectal cancer tumouroids. Western blot analysis demonstrates the expression of the ECM degradation protein MMP7 and the EMT marker Vimentin after 10 days in culture in 10% matrix tumouroids. Densitometry analysis using ImageJ demonstrated a fourfold and twofold increase in vimentin expression in HT29 and HCT116 tumouroids in comparison to monolayers.

3.5 Discussion

This Chapter explores the effect of matrix density on cancer cells cultured in collagen gels, and how these differences in matrix density influence cancer cell morphology and invasion. The method of PC, developed previously in our lab[120], was used to expel excess interstitial water and increase the collagen density within collagen hydrogels. We have developed a 3D *in vitro* cancer model and identified different mechanisms of invasion between colorectal cancer cell lines. The advantage of using tumouroids is that they allow mechanistic investigations such as cell migration due to the distinct compartments (the ACM and the stromal surround).

3.5.1 Matrix density of collagen hydrogels

Collagen is the most abundant protein and constitutes around 30% of the total protein content within the human body. Currently, type I collagen hydrogels are the gold standard for 3D *in vitro* cell culture, however their low mechanical strength is not representative of *in vivo* tissue matrix density. PC of collagen hydrogels rapidly produces dense collagen constructs that mimic the structural characteristics of *in vivo* tissues without compromising cell viability[120]. These constructs have been shown to support the growth and promote the normal phenotypic expression of a variety of different cell types including fibroblasts[151], ECs and human bone marrow derived stem cells (HBMSCs)[117]. However, one of the major limitations of PC collagen gels is the inability to control for fibril diameter or fibril orientation. This is particularly relevant with regards to cancer invasion, as recent work published has shown fibril diameter and not pore size is the main determinant of cell clustering and invasion[152]. There are a variety of different techniques that can be used in conjunction with PC

collagen gels to control fibril orientation. A study by Guo *et al.* in 2007 established a simple technique to control collagen fibril orientation, which requires no specialized equipment other than streptavidin coated magnetic beads and a magnet[153]. Incubating the magnetic beads within the gel and using a relatively weak magnet, the authors demonstrated highly aligned collagen 1 hour after fibrillogenesis. Another inexpensive technique utilized by Georgiou and colleagues was reported in 2013 and involved a method of cellular self-alignment using tethered PC collagen gels. This method generated aligned stabilized collagen gels in 24 hours and was found to promote neuronal growth during rat sciatic nerve repair[154]. Focusing on developing anisotropic biomaterials will provide novel methods of creating aligned scaffolds for tissue engineering and regenerative medicine purposes.

We first examined the matrix density of collagen gels under varying types of PC. Partial and full PC under a 175g weight for 1 and 10 minutes, generated matrices of 2.6% and 6.9% collagen respectively. It is interesting to note that there is a lack of information on the matrix density of different tissues. However, due to the soft nature of bowel tissue, it is highly unlikely that it contains dense amounts of collagen in comparison to bone or tendon. A different method of producing stiff collagen constructs was developed recently and works on the principal basis interstitial fluid removal using biocompatible hydrophilic absorbers instead of a weight[144]. Using this method we were able to generate collagen matrices consistently of 9.6% collagen content. One of the disadvantages of creating PC collagen gels lies within the uncontrollable heterogeneity during the PC process. The fluid-leaving surface, in this instance the top of the construct, always forms compacted lamellae of collagen fibrils. This was explained in detail by Brown and colleagues[120]. Other groups have made advances in generating more biomimetic collagen scaffolds. Typically, this

involves increasing the overall concentration of collagen in the acid solution or using reverse dialysis to generate more defined collagen fibril orientations[155]. Developing scaffolds with controllable characteristics such as matrix stiffness, pore size or fibril orientation will provide the foundation of the next generation of biomimetic scaffolds.

3.5.2 Colorectal cancer cell proliferation in 3D

In order to test the effect of matrix density on cancer cell behaviour, we chose to construct ACMs with two different collagen densities; 3% and 10% collagen using both HT29 and HCT116 cells lines. The alamarBlue assay was used to assess the proliferation rate of HT29 and HCT116 cell lines in the 3% matrix tumouroids over a 14-day period. The growth rates of HT29 and HCT116 cultures, varied slightly. HT29 cells cultured within 3% matrix tumouroids were characterized by a steady decrease in proliferation up to day 14. This decrease in cell proliferation could be explained by the migration and aggregation of cells to form cell aggregates within the ACM. In contrast, HT29 cells cultured in 10% matrix tumouroids did not exhibit the same decrease in proliferation and the cell number increased steadily until a plateau was reached at day 14. Light microscope analysis of the interface between the ACM and the stromal surround revealed moderately – poorly differentiated glandular structures, which formed over a 21-day period. Furthermore, the alamarBlue assay may not have been able to penetrate the newly formed aggregates, which may have resulted in an overall decrease in the readings obtained from the cultures. The problem of transferring 2D end-point assays to 3D cell culture has been highlighted before in detail[156]. It is also important to note the presence of

proliferative heterogeneity present within aggregates of cells, even as small as few hundred microns in diameter. A recent study by Laurent and colleagues investigated the expression of Ki67, a proliferative marker, in spheroids of different sizes. It was found that the expression of Ki67 was localized to the outer periphery of the spheroids with a diameter of 500μm, whereas the core of these spheroids contained a high proportion of quiescent hypoxic cells[157].

On the other hand, the HCT116 cultures had a much different proliferation profile than the HT29 cultures. Surprisingly, the proliferation readings appeared to drop transiently between day 3 and day 7 in both 3% and 10% matrix tumouroids. While there was no concomitant reduction in the size of cellular aggregates, the biochemical changes reflected within the alamarBlue readings may describe a short state of quiescence, which did not affect gross cellular behaviour. Similarly to the HT29 cultures, the drop and rise in the proliferation readings could indicate an inability of the alamarBlue to penetrate into the cellular aggregates. It is also possible that the cells are entering a brief state of quiescence as they become accustomed to the different microenvironmental change from 2D to 3D. Furthermore, there was no significant differences in the sizes of the these aggregates between HT29 and HCT116 cell lines indicating they may have a similar growth pattern in 3D culture, or other factors such as oxygen and nutrients limited their growth.

3.5.3 Colorectal cancer cell invasion from the ACM is cell specific

The morphology and cell distribution of cancer cells in 3% matrix tumouroids was examined using H&E staining. Cell aggregate formation was visible by day 7 in both HT29 and HCT116 tumouroids. These aggregates appeared to migrate to the edge of

the ACM and into the surrounding low-density collagen stromal surround. The formation of aggregates, or spheroids, is influenced by the density of the matrix the cells are cultured in[137]. This will be discussed in more detail later in the discussion.

The greatest differences between HT29 and HCT116 cell lines become more visible by day 14. At this time point, cell aggregates began to invade outwards from the ACM into the stromal surround. HT29 cells invaded the stroma as tightly bound compact aggregates whereas HCT116 cells, which also formed aggregates, invaded as epithelial cell sheets contiguous from the ACM. H&E staining revealed cell-specific morphological features. HT29 cells formed a highly concentrated network of budding glandular structures at the migrating front. This type of invasion resembles tumour budding and is often in histological sections *in vivo*[158]. Zlobec and colleagues strongly correlated the presence of budding with both vascular invasion and distant metastasis, which resulted in overall poor prognosis and tumour aggressiveness. Interestingly, they also investigated a small cohort of patients with metastatic colorectal carcinoma treated with anti-EGFR therapy and found that all patients with a *KRAS* mutation and/or high-grade tumour budding were found to be non-responsive to cetuximab and penitumumab. This does raise the prospect of using KRAS status alongside tumour budding grade to determine the suitability for anti-EGFR therapy.

On the other hand, cancer epithelial cell sheet migration such as that observed in HCT116 cells is not commonly detected in histological samples of colorectal cancer. In a systematic review of the histological characteristics of colorectal cancer, Fleming *et al.* characterized the presence of epithelioid neoplastic cell sheets at the tumour-stroma boundary in medullary carcinomas, which have an occurrence rate of 5-8 cases for every 10,000 colorectal cancers diagnosed[159]. Kitamura and colleagues

have also characterized the presence of collective invasion in a cis-Apc$^{+/\Delta 716}$ *Smad4*$^{+/-}$ mutant mouse model of colorectal cancer[160]. It was found that the over-expression of MMP2 and MMP9 by immature myeloid cells at the invasive front promotes this collective invasion. However, we have also identified similar mechanisms of collective migration within our tumouroids, which lack an immune component, suggesting that an immune component is not essential for this type of invasion.

To further characterize cancer invasion, light microscopy was used to evaluate the distance migrated by cellular aggregates and cell sheets in both cell lines. This was carried out on live cultures as histological processing can occasionally shrink the hydrogel stromal surround and affect the evaluation of the distance migrated. In HT29 tumouroids, there was no correlation between the time and distance migrated of cellular aggregates within the low-density stroma. This is evident by some cultures at day 14 travelling a further distance than those cultured for 21 days (2,866.1μm^2 ± 1,606.9μm^2 vs. 2,592.2μm^2 ± 812.8μm^2). This indicates that once cell aggregates detach from the ACM and invade, their migration is not limited and they are free to travel easily within a low-density collagen gel. It is also interesting to note that this mechanism of invasion i.e. a whole spheroid/aggregate detaching and invading from the primary ACM or spheroid has not been shown before in any 2D or 3D *in vitro* models of cancer. It is observed exclusively at the invading front of *in vivo* tumours.

3.5.4 Extracellular matrix density and composition of the stroma enhances cancer invasion

Tumour stiffness composition and the effect on cancer invasion has often been poorly studied, particularly within 3D *in vitro* cancer models. To date, most of the studies to date have not displayed control over ECM composition or concentration like the model presented in this thesis. Previous studies have focused on invasive *in vitro* models using either a single ECM protein such as collagen[161] or Matrigel[139] where the precise quantity of each basement membrane extract protein is unknown[162]. The objective of this Chapter was to further assess cancer invasion with a known surrounding matrix density and specific ECM composition. We incorporated a dense ACM (10% collagen) into a surrounding stroma of the same density, which included laminin, the bulk component of the BM.

Overall, HCT116 cells were much more invasive than HT29 cells. Interestingly, the addition of laminin to the stroma did not induce any morphological changes in HT29 and HCT116 cells, although it did enhance the invasion profile in comparison to the collagen only stromal surround. The incorporation of laminin also appeared to increase the overall size of invaded HT29 cellular aggregates in the stromal surround. This difference in size is most likely due to the earlier onset of migration into the stroma whereby cells migrate to regions of higher nutrients and oxygen concentrations and continue to proliferate. Differences in distances travelled of these aggregates demonstrated interesting migration patterns of clusters of cells. It appeared that once cellular aggregates migrate out from the ACM, they are able to migrate up to 3mm within 24 hours of detachment, indicating a highly motile phenotype of these cells in a low-density collagen stroma. Laminins are major regulators of cell adhesion, migration and proliferation[117,163]. They regulate these cellular processes via specific integrin binding. Moreover, the laminin-5 γ2 chain has

been implicated as an adhesion substrate for epithelial cells and is expressed in a wide variety of invasive carcinomas[164,165]. This is consistent with other findings in the literature. Pirilä *et al.* first demonstrated that the laminin-5 γ2 chain is proteolytically degraded by various MMPs into an 80 kDa form that reveals a cryptic site necessary for enhanced epithelial cell migration[91]. Another landmark study published in 2001 by Hlubek and colleagues correlated the expression of the γ2 chain of laminin-5 to the invasive front of colorectal carcinomas[166]. The authors also showed that nuclear accumulation of β-catenin in invasive cancer cells was present in primary tumours, however its expression was transient due its absence in metastases, which was also associated with a reduced expression of laminin γ2. They suggested that external influences from the surrounding ECM environment regulated the intracellular distribution of β-catenin and consequently activating its target genes. There have been other reports implicating laminin-5 modulation by the local microenvironment[167]. Laminin also significantly enhanced the invasion rate of HCT116 cells irrespective of the density of the stromal surround. Notably, the rate of migration differed. In the low-density collagen stroma, cells appeared to migrate in a linear fashion, particularly after 10 days in culture indicating the ability of the cells to remodel and migrate easily through this mechanically weak matrix[168]. An increase in stromal density revealed a gradual slowdown in HCT116 cell invasion by day 21. This decrease in migration speed could be attributed to the steric hindrance caused by the stiff surrounding stroma.

3.5.5 The presence of invasive leader cells corresponds with EMT and ECM remodelling

An analysis of the invading cells is essential to determining how these migratory cues and processes are regulated. The objective of these experiments was to morphologically analyze the invading cells and to determine whether changes at the molecular level that drive invasion. All of the following experiments were done in tumouroids with a dense surrounding stroma.

We observed three independent morphologies of invading HT29 cells and two for HCT116 cells. We found polarized collective migration was present in HT29 cells, which was evident by the aligned directional migration of cell sheets in non-aligned collagen gels indicating a high level of proteolytic degradation by cells to migrate. Previous studies have suggested that cancer invasion is dependent primarily on the loss of cell polarity, which drives the random migration of cancer cells[169]. However, we have found that this is not a necessary event for cancer invasion. Interestingly, we also observed leading elongated cells with a mesenchymal morphology at the edge of the invading cell sheet, forming cellular protrusions. These 'leader cells' often guide the following cells that compose the main body of the cell sheet. The collective migration of these cells did not appear to be driven in a single direction, with the presence of many leader cells migrating in random directions and appearing non-polarized. Several recent studies have highlighted the importance of these leader cells and their presence on the invasive front, and it is thought that they are phenotypically different from follower cells[50,150]. Cheung and colleagues recently demonstrated in 3D organoid model of breast cancer that collective invasion was led by genotypically distinct cells that were defined by their expression of the basal epithelial genes K14 and p63[170]. They showed that knockdown of either K14 or p63

was sufficient enough to block collective invasion. The genotype of leading invading cells in tumouroids will be discussed in more detail in Chapter 4.

Although, the behaviour of leader cells is inadequately studied in cancer, it may mimic TGFβ stimulated collective migration present during the wound healing process[50]. The presence of these leader cells in our tumouroid model also highlights the heterogeneity of cancer cells cultured in 3D for extended periods of time.

Furthermore, the upregulation in expression of the EMT marker vimentin and MMP7 suggests that invasion is an active process dependent on the proteolysis of the surrounding ECM. Interestingly, Remy et al have demonstrated that MMP7 degradation of the β3 chain in laminin-5 enhanced the migration of colorectal adenocarcinoma[150]. The expression of MMP7 has been shown to be differentially expressed in a small cohort of patients with colorectal tumours in different stages with the highest levels of expression associated with advanced disease[51]. It is likely the upregulation of MMP7 coupled with the addition of laminin in the stroma is responsible for the enhanced migration of both HT29 and HCT116 cells in the collagen-laminin cultures. Interestingly, in the majority of epithelial tumours such as those of the bowel or breast, cells typically tend to migrate collectively as outlined previously in Section 1.1.3[171]. *In situ*, invasive cells typically upregulate EMT markers such as vimentin, however this change in expression is not always associated with a spindle shaped mesenchymal phenotype. HT29 cells which invaded the dense stroma as aggregates and sheets, upregulated the expression on vimentin highlighting the heterogeneity in cell migration utilized by cancer cells. Using 3D reconstructions of the cancer-host interface, Bronsert *et al*. found that while invading buds exhibited changes in the expression of EMT markers, they rarely changed to a spindle-shape morphology.

3.6 Conclusion

In summary, we have described the development of a 3D *in vitro* cancer model with controllable parameters in both the matrix density and composition of both the tumour compartment and the stroma. The results presented in this Chapter have demonstrated distinct invasive mechanisms of CRC cells driven by matrix density alone i.e. from aggregates of cells to cell sheets. This model is the first to date to replicate the collective budding migration observed in histological sections at the invasive front of invading tumours. Furthermore, it appears that the invasion process is driven by several mechanisms simultaneously as seen by the presence of glandular structures, polarized collective migration and cell sheets driven by elongated leader cells. The addition of specific ECM proteins, such as laminins, can help further elucidate the interaction between cancer cells and the basement membrane, which acts as the primary barrier during invasion. We have found this to be particularly relevant for the migration of CRC cells in collagen gels. This migratory process is also driven by molecular cues as evident by the upregulation in ECM degradation proteins MMP7 and EMT marker vimentin, which contributes to a migratory phenotype. The development of sophisticated 3d *in vitro* cancer models such as the one presented here, aim to mimic the early steps of the metastatic process and are proving a vital step toward the understanding and development of therapies to prevent or reverse or block the switch to an invasive phenotype.

Chapter Four

Engineering a biomimetic stroma

4.1 Introduction

While metastasis is the leading cause of mortality in patients with CRC[40], studies have only recently started investigating the 'normal' components of a tumour such as the tumour stroma. The stromal cell types present in the *in vivo* tumour microenvironment consist mainly of fibroblasts, ECs and inflammatory cells. Although many of these cells will initially confer tumour-suppressing properties to the adjacent tumour, the stroma typically changes over time and eventually promotes growth, invasion and metastasis. This process is driven by the constitutive expression of certain tumour-derived cytokines such as TGF- β that transforms normal healthy fibroblasts into cancer-associated fibroblasts (CAFs). In recent years, it has become evident that cross-talk between tumour cells, CAFs and the surrounding ECM

contribute heavily to the initial metastatic cascade, mainly by fibroblast mediated degradation of the ECM to facilitate cancer invasion[118,172–174].

The presence of ECs in the stroma correlates to the high levels of pro-angiogenic factors released by cancer cells, which recruits them to the tumour site. Tumour induced angiogenesis is caused by an imbalance or pro and anti-angiogenic factors that results in 'leaky' vasculature. Many of these pro-angiogenic factors are released by fibroblasts, which compose the bulk cellular component surrounding a tumour.

Therefore, the objective of this Chapter was to investigate the effect of a reactive tumour stroma on cancer invasion and the ability of ECs to form primitive vascular networks within the stromal component of 10% matrix tumouroids. Due to the complex nature of co-culturing many types of cells together, only healthy fibroblasts and ECs were incorporated into the stroma. The presence of the BM was also hypothesized to be a critical component required for vasculogenesis and was included as it enhanced the invasion profile of CRC cells in the Chapter 3.

4.2 Materials and methods

4.2.1 Cell maintenance

In this Chapter, only the HT29 colorectal cancer cell line was used. Primary HDF and HUVECs were incorporated into the stromal surround. All cells were maintained routinely in culture and the appropriate cellular concentrations were prepared for the experiments described below.

4.2.2 Fabrication of biomimetic tumouroids

10% matrix tumouroids were fabricated as described in Section 2.8 with slight modifications. HT29 ACMs were created with a density of 50,000 cells per ACM (208,000 cells/ml). Once these were returned to the incubator, HDF and HUVECs were detached using trypsin and counted to give a cellular concentration of 25,000 HDFs and 50,000 HUVECs (per ml) per single well for the three cell co-cultures. The cell volumes in terms of cell density were seeded with a ratio of 8:2:1 for HT29, HUVEC and HDF cells respectively prior to removal of interstitial fluid. The stromal surround cell populations are based on ratios determined in a previous study investigating the effect of laminin as a promoter to form vascular networks[117,142]. The appropriate cell numbers were added to neutralized collagen containing laminin at a concentration for 50µg/ml. This was mixed carefully to ensure HDFs and HUVECs were mixed thoroughly and no bubble formation occurred in the gels. Briefly, 500µl of the HDF-HUVEC-collagen-laminin mixture was added to a 24 plate and allowed to gel for 5 minutes on a plate heater set at 37ºC. HT29 ACMs were then placed on top before 500µl of HDF-HUVEC-collagen-laminin solution was added to fully immerse the ACM. This was allowed to gel for a further 10 minutes at 37ºC before the hydrophilic absorbers removed the interstitial fluid within the gel. Finally, 1ml of DMEM and EGM (1:1) was added to each well and returned to the incubator immediately set at 37ºC (5% CO_2/air and 95% humidity). From this point onwards, the HT29, HDF and HUVEC co cultures will be referred to as the 'biomimetic tumouroids'.

Some experiments were carried out in physiological hypoxia. Physiological hypoxia is also known as '*in situ* normoxia' and is representative of the normal oxygen pressure present within tissues. This can typically range from 4-14% O_2 in a variety

of different tissues such as the brain, bowel and liver[175]. A separate incubator was used and set at 37°C (5% CO_2, 5% O_2 and 90% humidity).

4.2.3 Live dead assay

The live/dead viability/cytotoxicity kit (Invitrogen, Paisley, UK) was used to assess the viability of the biomimetic tumouroids as stated in the manufacturers protocol. Briefly, 5µl of calcein AM and 20µl of ethidium homodimer-1 was added to 10ml distilled PBS (DPBS) and tube was inverted several times to mix the solution. Cell culture medium was aspirated and the cultures were washed 3 times in PBS very briefly. The live/dead solution was then added to each well and returned to the incubator at 37ºC for 45 minutes. Biomimetic tumouroids were then imaged using an EVOS FL imaging microscope (Invitrogen).

4.2.4 Immunofluorescent staining of biomimetic tumouroids

Immunofluorescent staining of biomimetic tumouroids was carried out as described in Section 3.2.5. Briefly, tumouroids were fixed using 10% formalin for 30 minutes and washed three times for 5 minutes with PBS. After permeabilising with 0.2% TX-100 for 30 minutes, the gels were washed thoroughly with PBS (3 x 5 minutes) and blocked with 1% BSA for 30 minutes. After washing with PBS (3 x 5 minutes), the gels were incubated with either a CK20 rabbit primary antibody (D9Z1Z from New England Biolabs, Herts, UK), an anti-CD31 mouse primary antibody (JC70/A from Abcam, Cambridge, UK) or a vimentin mouse primary antibody (sc-6260 from Santa

Cruz, CA, USA) overnight at 4ºC. Following incubation, the gels were washed 3 times in PBS for 5 minutes and incubated with an Alexa Fluor 488 goat anti mouse igG secondary antibody (Invitrogen, Paisley, UK) and DyLight 594 goat anti-rabbit igG secondary antibody (Vector labs, Peterborough, UK) for 2.5 hours at room temperature. The gels were then washed with PBS thoroughly (3 x 10 minutes) and 2 drops of NucBlu (Invitrogen, Paisley, UK) was added to the PBS in each sample. Tumouroids were imaged in 24 well plates using an inverted EVOS FL imaging microscope.

4.2.5 Vascular network analysis

The formation of vascular networks in the stromal surround was analyzed and quantified using the ImageJ software (NIH, v1.43). The length, width, number of branches, junctions and loops were all quantified. The cell counter plugin was used for ImageJ. Figure 4.1 demonstrates how the length of each branch was measured and was traced over using the freehand line tool (yellow line). The numbers in the images below signify how the number of branches (number 1), the number of junctions (number 2) and the number of loops (number 3) were counted. The width of each vascular branch was measured using the straight-line tool and was used to draw across the width of each vascular branch within the image. Six images were analyzed per condition and all tubules, junctions and loops were quantified.

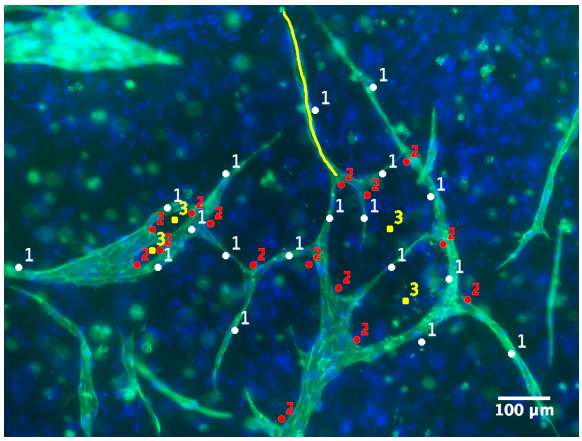

Figure 4.1: ImageJ analysis of vascular networks. The number of branches, junctions, length and width of vascular networks was analyzed using ImageJ. The numbers in the images signify how the number of branches (number 1), the number of junctions (number 2) and the number of loops (number 3) were counted. (n=6) Scale bar – 100µm.

4.3 Results

4.3.1 Viability of cells in HDF and HUVEC co-cultures

The objective of these experiments was to investigate the cell viability of cells in HDF and HUVEC co-cultures. It has been demonstrated before in collagen hydrogels that ECs do not survive when co-cultured with fibroblasts[108,117]. ECs are typically found in close proximity to the basement membrane in the *in vivo* scenario and it is thought to promote EC survival so it was added to all experiments unless stated otherwise. HDF and HUVECs were co-cultured together and seeded in 10% collagen gels containing laminin. Following 10 days of growth, the live/dead assay was carried out as outlined in Section 4.2.3. Interestingly, HDF and HUVEC co-cultures had relatively few dead cells and could be distinguished at lower magnifications (Figure 4.2 – left panel), as some ECs appeared to take cobblestone morphology. This was evident by the clustering of cells together to form small sheets throughout the gel. On the other hand, fibroblasts appeared disorganized throughout the gel.

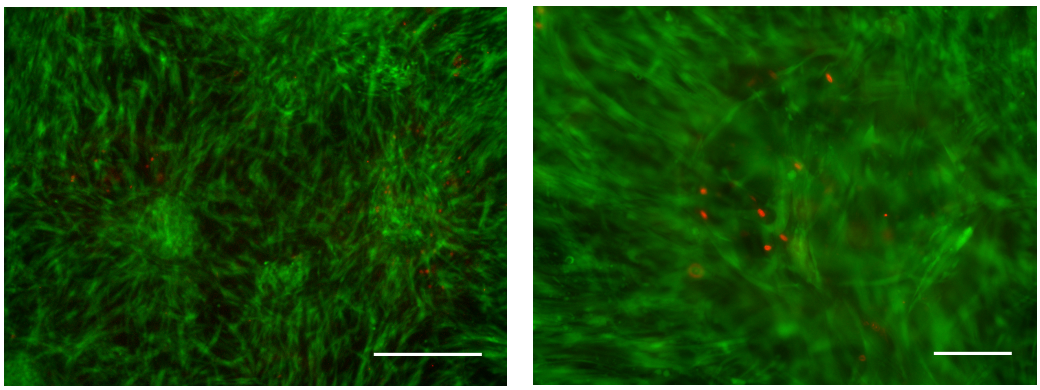

Figure 4.2: Live/dead stain of HDF and HUVEC co cultures. HDFs and HUVECs were co-cultured in 10% collagen gels containing laminin. Cell viability was assessed after 10 days of culture using a live (green)/dead (red) assay. Scale bar (left) – 1mm, (right) – 100µm.

4.3.2 Vascular network formation in HDF and HUVEC co cultures

The previous section determined that HUVECs survived in high numbers when co-cultured with HDFs. Therefore, the objective of these experiments was to further investigate the morphology and behaviour of HUVECs in the absence of cancer cells but in the presence of stromal cells that would be present within the tumour microenvironment, namely HDFs. HDFs and HUVECs were co-cultured for up to 21 days in both normoxia (21% O_2) and physiological hypoxia (5% O_2) and their morphology was investigated using immunofluorescence of CD31 and vimentin.

HDFs and HUVECs co-cultured in normoxia in the absence of laminin formed end-to-end vascular networks (Figure 4.3). These vascular networks were longer and wider, but not as interconnected as the HDF-HUVEC co-cultures in the presence of laminin (Figure 4.4). Vascular networks without laminin had an average length and width of 290.3μm ± 120.7μm and 35.9μm ± 15.4μm whereas the presence of laminin leads to the formation of vascular networks with a length and width of 197.5μm ± 87.5 and 19.1μm ± 8.1μm respectively (Figure 4.4). The length and width were both statistically significant ($p<0.05$). However, an interesting observation is that co-cultures without laminin formed significantly higher numbers of ECs with a cobblestone morphology in comparison to presence of laminin. HDF and HUVECs cultured in physiological hypoxia with laminin had a similar length and width to the normoxia cultures (215.2μm ± 79μm and 21.4μm ± 7.2μm respectively). Moreover, the presence of laminin in the normoxia cultures appeared to produce much more significantly interconnected vascular networks as signified by the large number of branches, loops and junctions ($p<0.05$) in comparison to the co-cultures in the absence of laminin and in hypoxia in the presence of laminin (Figure 4.5).

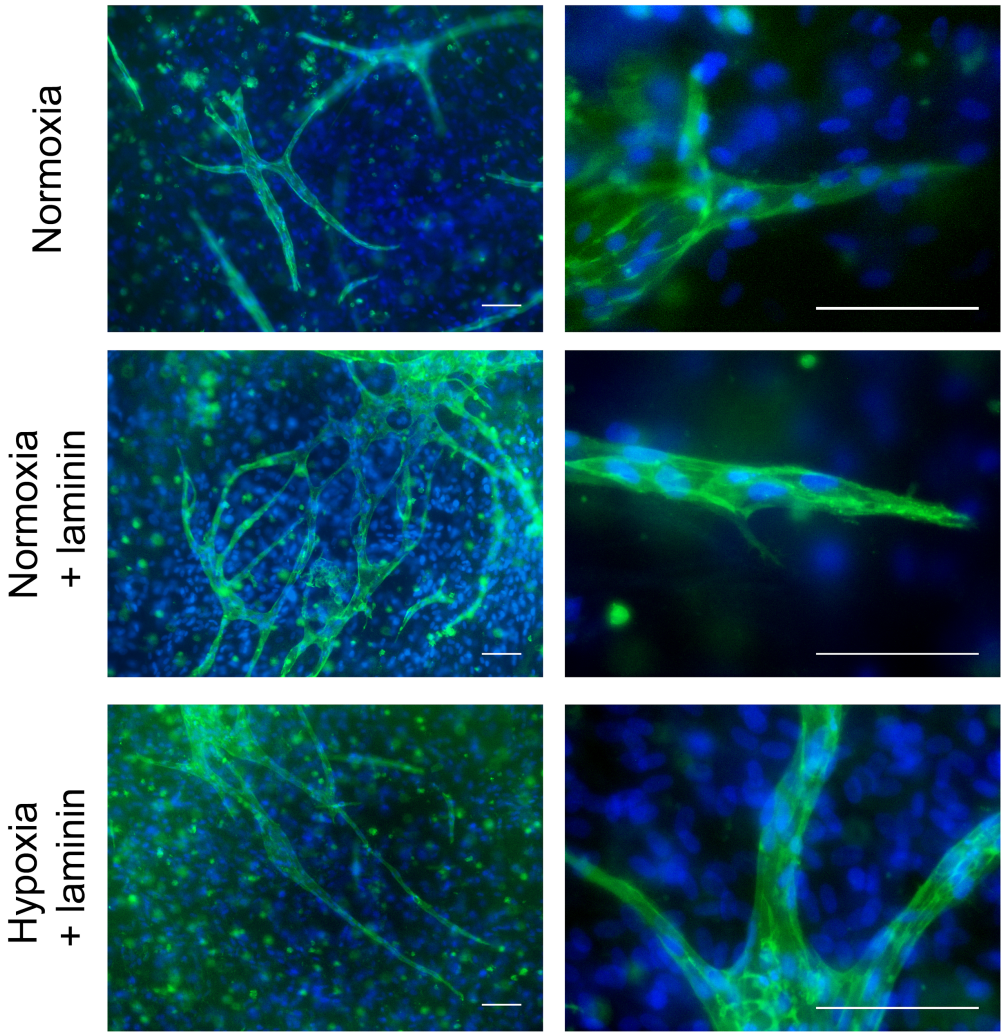

Figure 4.3: Endothelial cell morphology in HDF and HUVEC co-cultures. HDFs and HUVECs were co-cultured for 21 days under normoxia (21% O_2) in 10% collagen gels with and without laminin and in physiological hypoxia (5% O_2) with laminin only. HUVEC morphology was assessed using immunofluorescence of CD31 (green) and DAPI (blue). Scale bar – 100µm.

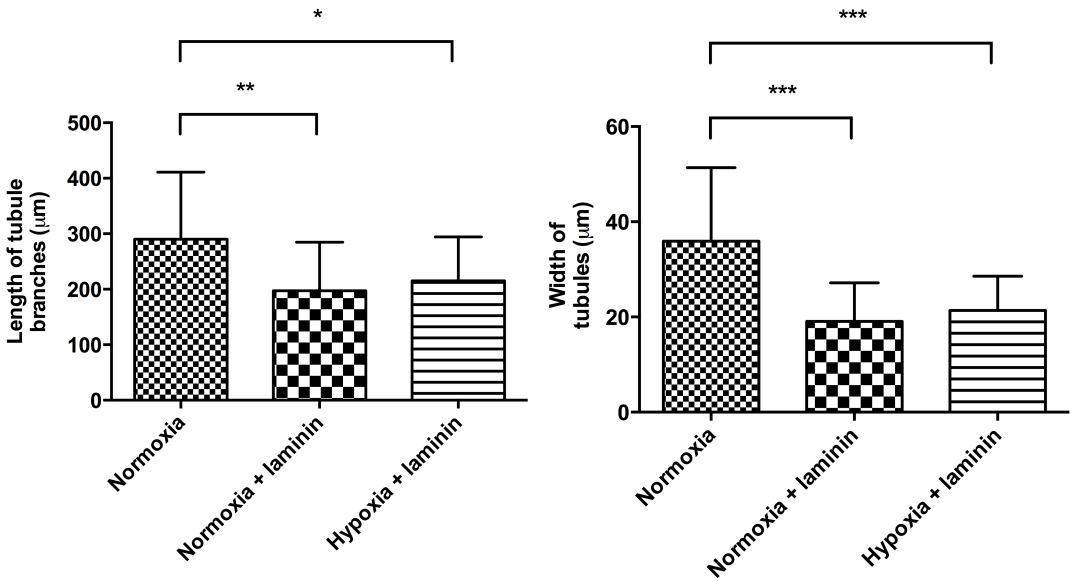

Figure 4.4: Analysis of vascular network length and width in HDF and HUVEC co-cultures. ImageJ was used to quantify the length and width of vascular networks in HDF and HUVEC co-cultures. Normoxia cultures without laminin formed longer and wider networks than either normoxia with laminin or hypoxia with laminin. Data is presented as mean ± SD (n=6). * $p < 0.05$; ** $p < 0.01$, *** $p < 0.0001$.

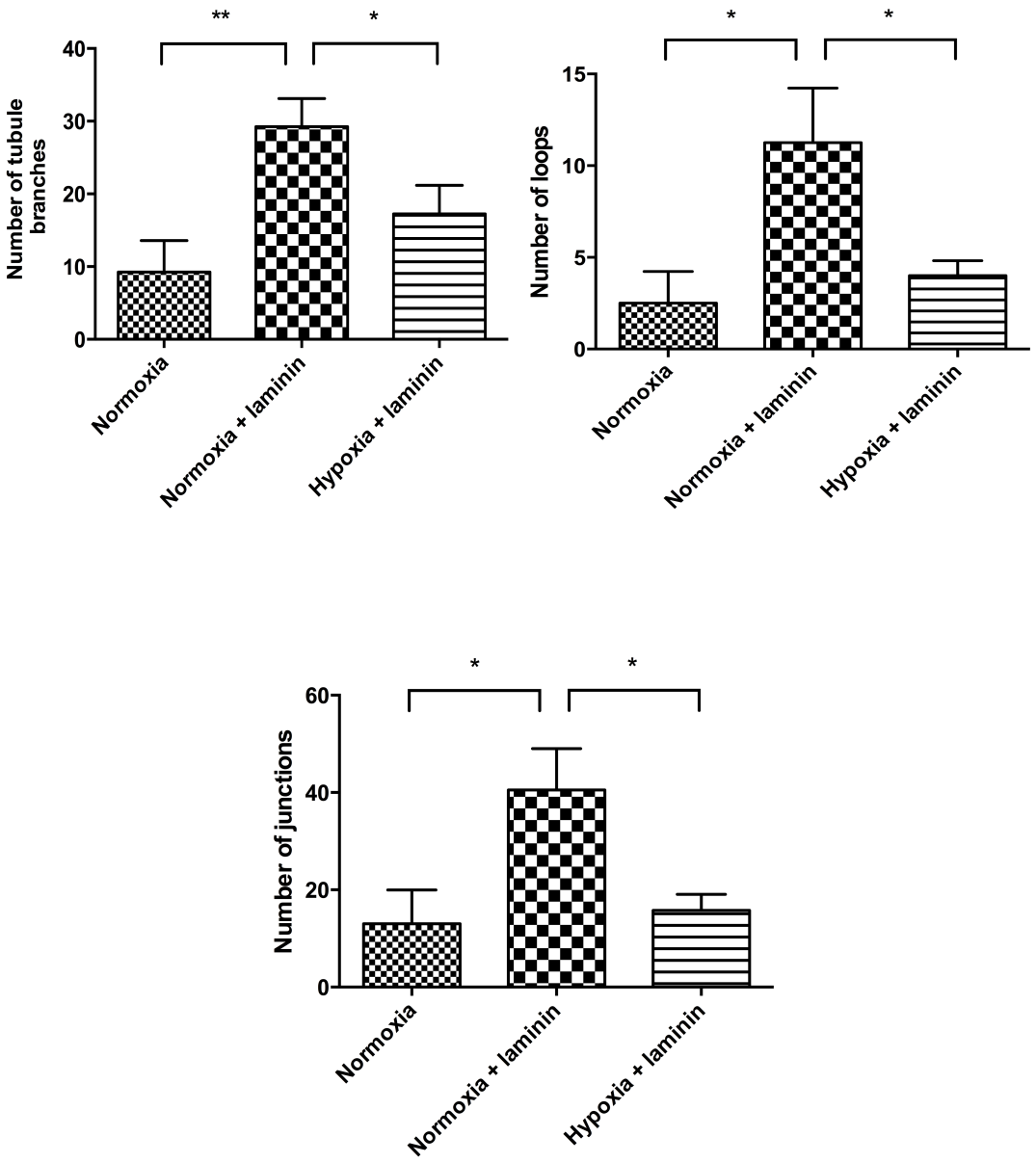

Figure 4.5 Analysis of the number of branches, loops and junctions in HDF and HUVEC co-cultures. ImageJ was used to quantify the number of branches, loops and junctions in HDF and HUVEC co-cultures. The normoxia cultures with laminin had a significantly higher number of branches, loops and junctions in comparison to normoxia without laminin and hypoxia with laminin. Data is presented as mean ± SD (n = 6). * $p < 0.05$, ** $p < 0.01$

The morphology of the HDFs was also investigated in the HDF and HUVEC co-cultures. HDFs were stained for the mesenchymal marker vimentin, which stains the intermediate filaments in mesenchymal cells such as fibroblasts. HDFs stained positively for vimentin after 21 days in culture and had an elongated morphology

(Figure 4.6). HDFs also appeared to form a sheet as they appeared in the same plane and were appeared to align together in a single direction. This was not evident in the fluorescent images in the live/dead stain in Figure 4.2, which stains both cell populations simultaneously.

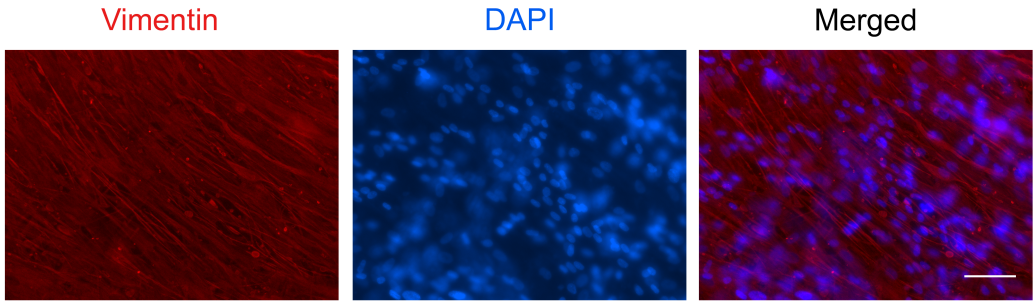

Figure 4.6: Immunofluorescent analysis of HDFs in HDF and HUVEC co-cultures. HDFs and HUVECs were co-cultured for 21 days in normoxia in the presence of laminin. HDFs were stained for vimentin (red) and DAPI (blue). Scale bar – 100µm.

4.3.3 Cell viability in biomimetic tumouroids

The objective of these experiments was to investigate cell viability in the three cell biomimetic tumouroids. Biomimetic tumouroids were fabricated as described in Section 4.2.2 and cultured for up to 21 days and the live/dead assay performed at day 10 and 21. Dead cells were not observed at either time point indicating an ability of the three cell populations to remain alive in culture together (Figure 4.7). Interestingly, cancer cells invaded at day 5 in a cellular stroma in comparison to day 10 in an acellular stroma (Table 4.1). Cell aggregates and sheets invaded from the ACM and were both visible within the cellular stroma. Again, at day 10, cells had an elongated morphology similar to the fluorescent images in Figure 3.11. However, by

day 21, there were visible gaps within the invading cell sheet (Figure 4.7, white arrow) mimicking microlumens, which are often seen in epithelial tubulogenesis.

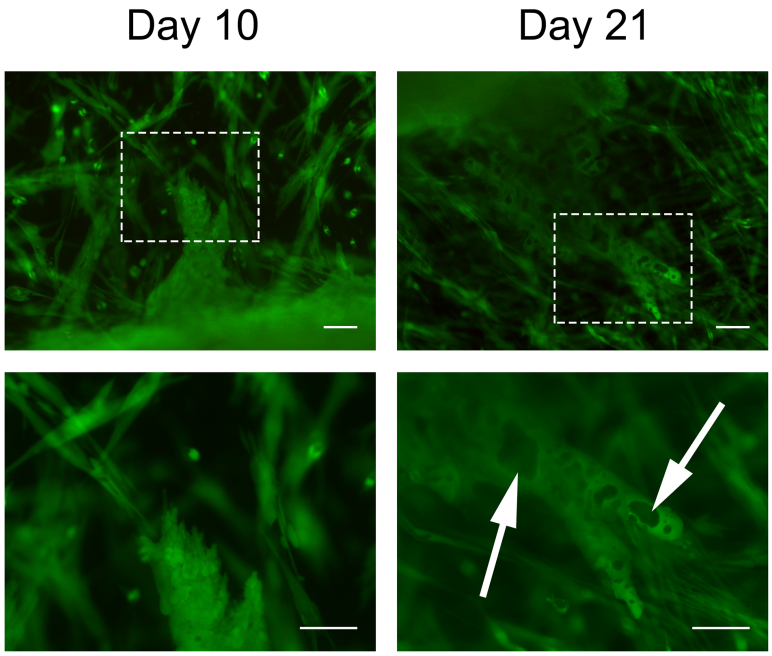

Figure 4.7: Cell viability of biomimetic tumouroids. Biomimetic tumouroids were cultured for up to 21 days and cell viability was assessed by the live (green)/dead (red) assay. HT29 cell sheets invaded as cell sheets with an elongated morphology. By day 21, there were visible gaps within the invading sheet indicating epithelial tubulogenesis (white arrows). Scale bar – 100µm.

4.3.4 Cancer invasion in biomimetic tumouroids

In Chapter 3, we investigated the effect of stromal matrix composition and density on cancer invasion (Section 3.4.2). These experiments aimed to investigate the effect of a cellular stroma on the timeline of cancer invasion in addition to the size of the invaded cellular aggregates. In biomimetic tumouroids, HT29 cancer cells invaded at day 5 whereas (Table 4.1) under the same conditions without a cellular stroma they invaded at day 10 (Table 3.1). Although, HT29 aggregates invaded the cellular stroma at day 5, the size of the aggregates was not statistically significant from the

acellular stroma aggregates (Figure 4.8) At day 21, aggregates in the acellular stroma and cellular stroma were 164,497.7µm ± 49,132.9µm and 182,726.7µm ± 78,708.4µm respectively.

Stromal surround composition	Day of Invasion HT29 cells
Acellular stroma (10% collagen + laminin stroma)	Day 10
Cellular stroma (10% collagen + laminin stroma)	Day 5

Table 4.1: The invasion timeline of HT29 cells in both an acellular and cellular stroma.

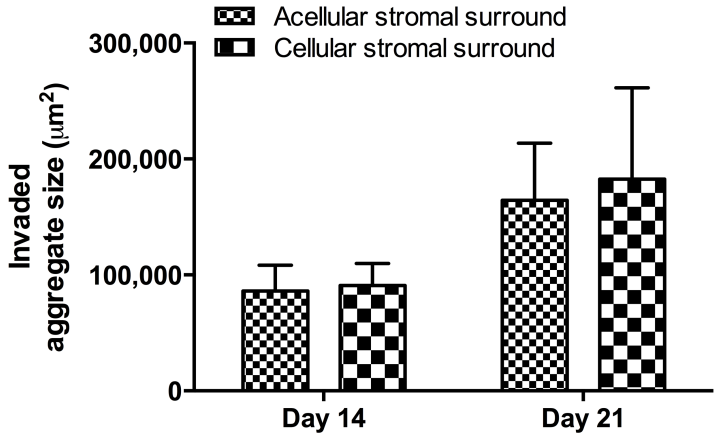

Figure 4.8: Invaded cell aggregate size in HT29 tumouroids. Tumouroids were cultured for up to 21 days. HT29 cells formed cellular aggregates and invaded into either an acellular or cellular stroma. Data is presented as mean ± SD (n = 6).

4.3.5 Vascular network formation in biomimetic tumouroids

The previous experiments in this Chapter have confirmed the viability of HUVECs and their ability to form 'tube-like' structures when co-cultured with HDFs. The next step was to investigate cancer cell invasion and the presence of cancer cells on

vascular network formation. Biomimetic tumouroids were fabricated and cultured for up to 21 days either in normoxia or physiological hypoxia. Light microscope analysis of the morphology at the invading edge of biomimetic tumouroids cultured in normoxia proliferated much faster as evident by the greater amount of cells present in comparison to hypoxia and due to the inability of light to penetrate through the ACM (Figure 4.9a). HT29 cells invaded the biomimetic stroma as cell aggregates and cell sheets in the normoxia cultures. In hypoxia, cells exclusively invaded as cell aggregates. Cell aggregates invaded first at day 5 for both conditions, followed by cell sheet invasion by day 7.

To further investigate cell morphology and the formation of vascular networks, HT29 cells were stained for the colorectal cancer epithelial marker CK20 and HUVECs were stained with CD31. CK20 is a type I cytokeratin expressed mainly in the gastric and intestinal mucosa[176]. CK20 was expressed uniformly throughout the ACM while CD31 stained positively for HUVECs in the stroma indicating viable ECs present within the stroma (Figure 4.9b).

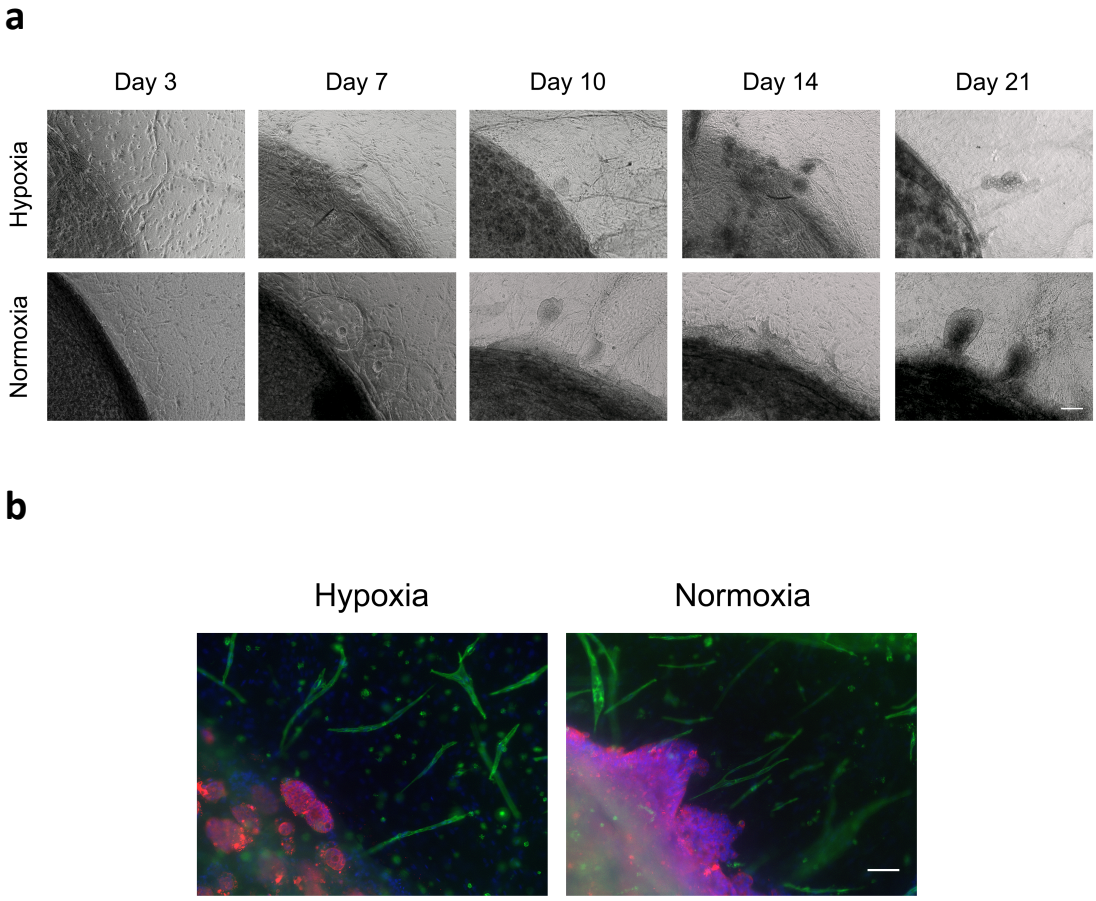

Figure 4.9: Morphological analysis of biomimetic tumouroid invasion and vascular network formation in normoxia and physiological hypoxia. HT29, HDF and HUVECs were co-cultured together over a 21-day period. Light microscope analysis confirmed HT29 aggregate and sheet invasion. CK20 (red) stained positively for HT29 cells while CD31 (green) established the presence of vascular networks in the cellular stroma. In hypoxia, cells invaded exclusively as aggregates whereas in normoxia, cell aggregates and sheets were present in the stromal surround. Scale bar (top) – 200µm, (bottom) – 100µm.

In normoxia, HUVECs formed tubule branches with a length and width of 456.8µm ± 136µm and 24.2µm ± 7µm in comparison to 388µm ± 124.5µm and 20.7µm ± 4.5µm for the hypoxic cultures (Figure 4.10). Although there were no significant differences in the length or width of the vascular networks, the number of tubule

branches, which had formed between normoxia and hypoxia, were significant (p=0.0031).

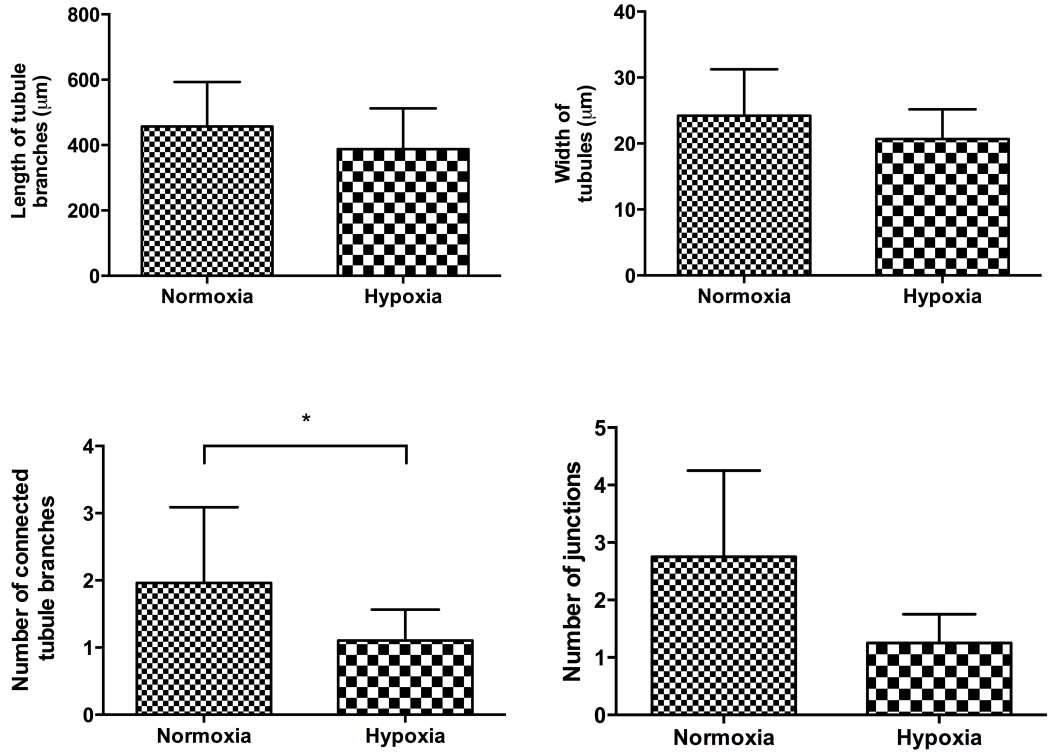

Figure 4.10: Vascular network analysis in biomimetic tumouroids. Biomimetic tumouroids were cultured for up 21 days, stained for the endothelial cell marker CD31 and quantified using ImageJ. Data is presented as mean ± SD (n = 6). *p = 0.0031.

Interestingly, the addition of HT29 cancer cells also led HUVECs to aggregate in a cobblestone pattern within the stroma of the normoxia cultures. In addition to the cobblestone morphology, HUVECs also formed disconnected, lengthy vascular branches (Figure 4.11). Cobblestone cells formed in large sheets on the apical side of the collagen gel forming a monolayer and strongly expressed membrane bound CD31. The cobblestone morphology of HUVECs is similar to the morphology routinely observed when expanding and culturing ECs in 2D monolayers[177]. On the

other hand, vascular networks contained a uniform intracellular expression level of CD31 throughout the entire tubule branch. Interestingly, the vascular networks observed were composed of multicellular structures, which appeared to wrap around in a three-dimensional configuration instead of simple end-to-end joining of single ECs (Figure 4.11, bottom right)

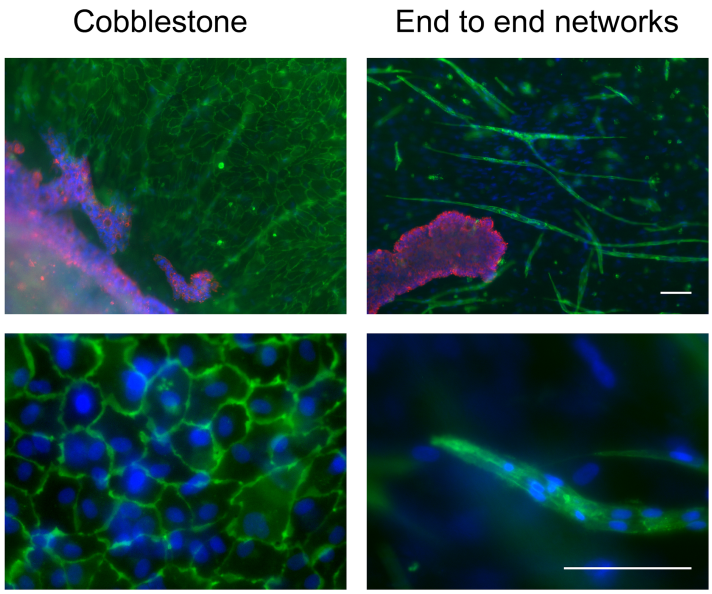

Figure 4.11: Endothelial cell morphologies in biomimetic tumouroids. HUVECs formed two distinct morphologies, cobblestone and end to end vascular networks, in the stroma as confirmed by immunofluorescence of CD31 (green). HT29 cells were stained for CK20 (red). (n=6). Scale bar – 100µm.

Once the stromal component was optimized, HT29 cancer cells were added to the tumouroid model and this illustrated key differences in the formation of end-to-end vascular networks within our tumouroids. While we observed vascular network formation in both the HDF-HUVEC co-cultures and the HT29-HDF-HUVEC co-cultures, there are striking differences between them. Figure 4.12 illustrates that the interactions of stromal cells with cancer epithelial cells in our tumouroids leads to the formation of significantly longer tubules than in the HDF and HUVEC co-

cultures alone (456.8µm ± 136µm compared to 197.4µm ± 87.5µm) ($p<0.0001$). While these tubules were over 2 times as long, they were significantly less interconnected ($p<0.0001$).

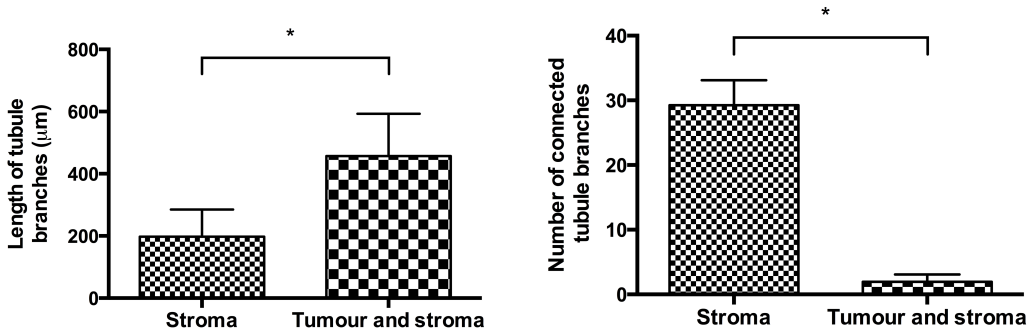

Figure 4.12: A comparative analysis of vascular network formation in HDF-HUVEC co-cultures and HT29-HDF-HUVEC co-cultures. ImageJ analysis was used to quantify and compare differences in vascular network formation in the presence and absence of cancer cells in HDF and HUVEC co-cultures. Data is presented as mean ± SD (n=6) *$p < 0.0001$.

4.3.6 Vascular network interaction with invading cancer cells

The metastatic cascade is initiated through a series of interactions between tumour cells and the nearby endothelium. While there is no functioning endothelium within our tumouroids, the same cell-cell interactions that take place within the *in vivo* microenvironment between cancer cells and ECs are present. Therefore, these experiments attempted to visualize some of these cell-cell interactions. HT29 cells and HUVECs were stained for CK20 and CD31 respectively. Figure 4.13 illustrates cell-cell specific interactions between the vascular networks and the cancer cells. While the vascular networks in the biomimetic tumouroids did not contain many junctions or highly branches networks, they appeared to fork into separate or diverging tubules that appeared to grow into the invading cell sheet (Figure 4.13, inset). Similarly, the vascular networks had a tendency to migrate towards the invaded cell aggregates within the stroma (Figure 4.13, bottom panel).

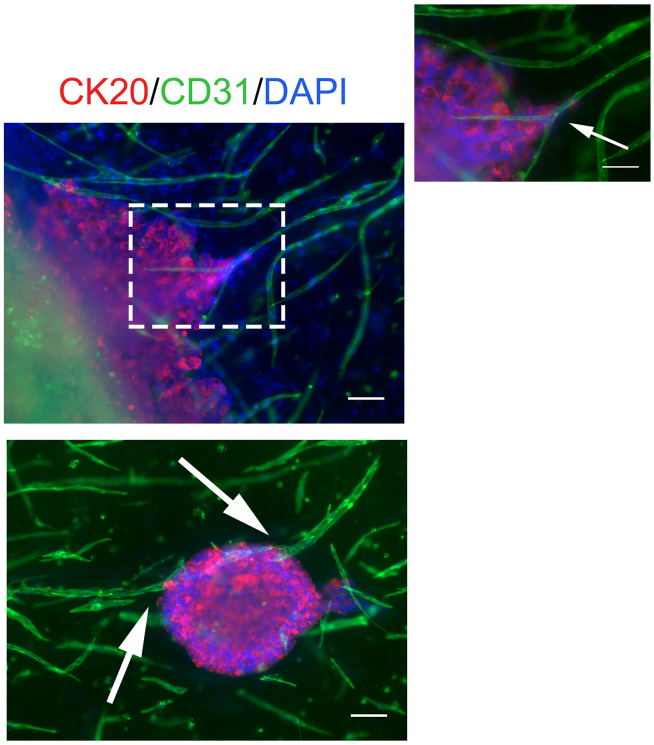

Figure 4.13: Cancer cell interaction with vascular network. Biomimetic tumouroids were cultured for up to 21 days and were stained for CK20 (red), CD31 (green) and DAPI (blue). Vascular networks appeared to migrate towards the aggressive invading cancer cell sheet edge where they diverged (white arrow, top right panel). Singular tubule branches also migrated towards the invaded aggregates within the stroma (white arrow, bottom panel). Scale bar – 100µm.

4.3.7 Loss of CK20 expression

While evaluating the interactions between cancer cells and the surrounding vascular networks, we observed the loss of CK20 in some of the invading cell sheets within the same tumouroid. However, this was strictly limited to the invaded epithelial sheets that had migrated the furthest distance from the ACM (Figure 4.14). HT29 aggregates within the ACM still expressed strong levels of CK20, highlighting the heterogeneity of protein expression within the same tumouroid (Figure 4.14, top left) Using ImageJ, we found that the loss of CK20 correlated strongly with the overall distance of invasion. CK20 negative sheets invaded an average distance of 516.6µm

± 224.3μm whereas HT29 cells that retained CK20 expression invaded 254.9μm ± 84.3μm (p=0.0089).

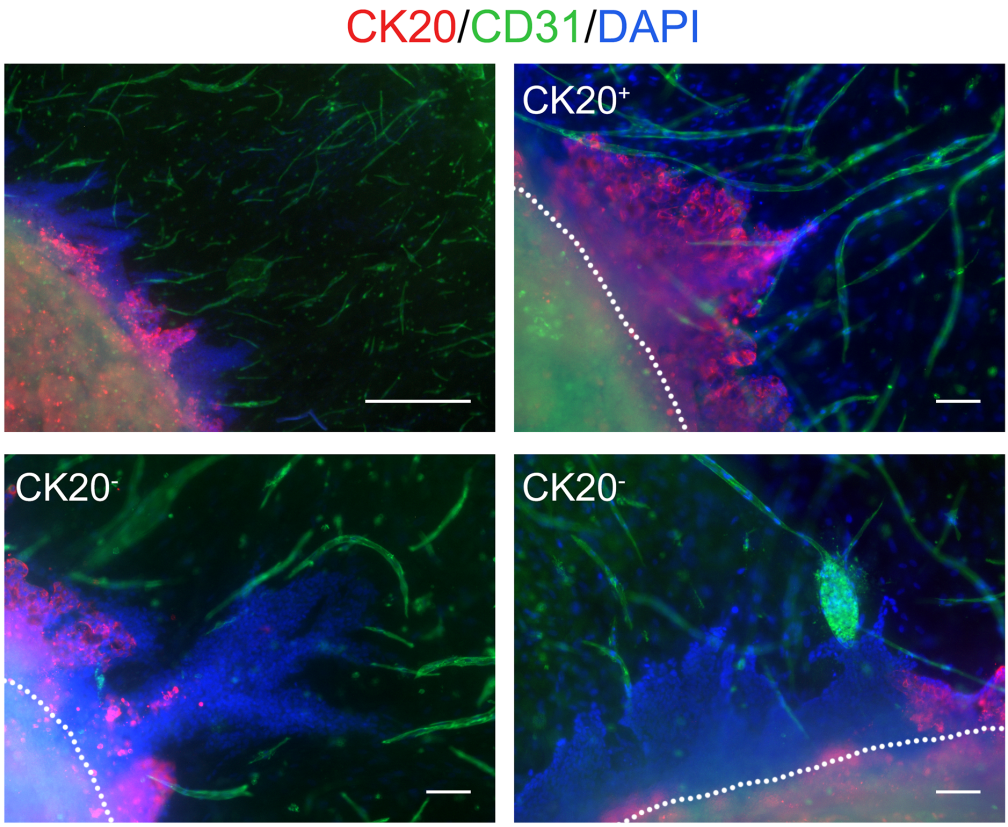

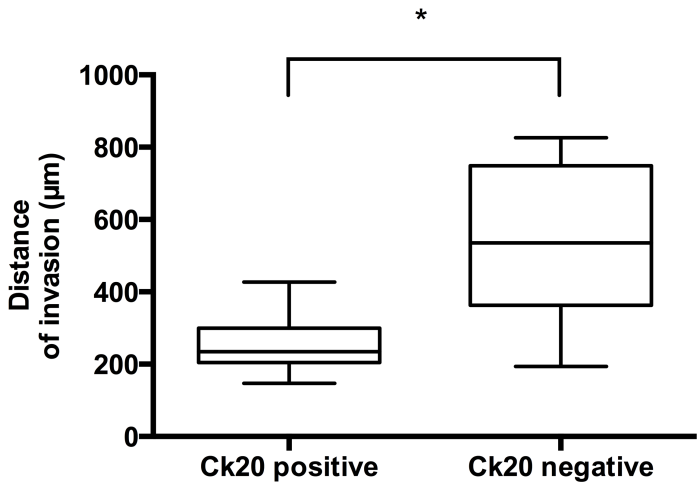

Figure 4.14: Loss of CK20 expression in biomimetic tumouroids. Biomimetic tumouroids were cultured for up to 21 days, fixed and stained for CK20 (red), CD31 (green) and DAPI (blue). The white dotted lines denote the boundary of the ACM and the stromal surround. The loss of CK20 correlated with the overall distance migrated of the invading epithelial cell sheet. Scale bar (top) – 1000µm, (bottom) – 100µm. Data is presented as mean ± SD (n = 6). *p = 0.0089.

4.4 Discussion

The work described in this Chapter explores the effect of the tumour stroma on cancer invasion and the effect of cancer cells on vascular network formation. Our laboratory has previously demonstrated the ability to direct ECs to form end to end vascular networks in collagen hydrogels[117,142]. The same research demonstrated that ECs do not survive when co-cultured with fibroblasts in plastically compressed collagen gels. Therefore, using a different method of removing the interstitial fluid of collagen hydrogels (via biocompatible absorbers), we aimed to investigate the effect of EC morphology within this dense collagen matrix. The hypothesis under test was that cancer cells would promote the development of lengthy 'leaky' irregular vascular networks, analogous to the *in vivo* scenario[178]. Furthermore, a large body of evidence demonstrated that the tumour stroma actively promotes the invasion of cancer cells[118]. We investigated the effect of stromal cells on cancer invasion.

4.4.1 The effect of stromal co-cultures on EC survival

There are various reports of EC co-cultures with different cell types. These can range from smooth muscle cells[179], astrocytes[125] to mesenchymal stem cells (MSCs) and fibroblasts[180]. For our tumouroid model we chose fibroblasts due to their significant presence within the local tumour microenvironment[181]. One of the main issues with co-cultures is optimizing the correct cell ratios of the different cell types without compromising cell phenotype, survival and cell behaviour[182]. It is important to ensure there are an adequate number of supplementary cells that release the correct range of concentration growth factors. While there is no general consensus on the optimum cell ratios, it will depend on each specific study. One study in 2013 which

investigated this was carried out by Rao and colleagues[183]. ECs and MSCs were co-cultured at a range of different ratios and the authors found that there was a threshold, which below MSC growth factors were inadequate to generate a sufficient cellular response. Therefore, the seeding densities and ratios should be carefully planned for each experiment. The ratio chosen for stromal component (2:1, ECs to fibroblasts) was adopted from previous work involving EC and fibroblast co-cultures in collagen hydrogels[142]. Contrary to previous reports, we found that ECs and fibroblasts survived in high numbers when co-cultured together in collagen gels. However, this could be due to the method of removal of interstitial fluid from collagen hydrogels to produce dense collagen matrices. Velazquez and colleagues demonstrated that the presence of fibroblasts promotes the survival, migration and differentiation of ECs into capillary networks via upregulation of some angiogenic factors[184]. They hypothesized that the differentiation of ECs into pre-mature vessels is not entirely mediated by VEGF/KDR pathway and that anti-apoptotic signals are provided by the fibroblasts in the co-cultures.

4.4.2 Normal fibroblasts promote cancer cell invasion

Fibroblasts are mainly responsible for the bulk synthesis, deposition and remodeling of the ECM within the surrounding stroma of a tumour[185]. It was originally thought that fibroblasts had a passive role in cancer but they are now recognized as having a well-established role in both the initiation and the progression of cancer[118,173,181]. Fibroblasts provide a large source of paracrine factors to both epithelial and endothelial cells. These factors include fibroblast growth factor (FGF), insulin-like

growth factor (IGF), EGF, hepatocyte growth factor (HGF) and the transforming growth factor-β (TGF-β) which contribute to an invasive phenotype[186,187].

In our tumouroids we observed that the presence of a cellular stroma (fibroblasts and ECs) enhanced the invasion of HT29 cells. In an acellular stroma, HT29 cells invaded at day 10 and in a cellular stroma invasion occurred at day 5. Interestingly, although the fibroblasts used in this study were healthy primary HDFs, we found that they still promoted the invasion of HT29 cells from the ACM. Other groups have reported similar findings. A recent study in 2015 by Knuchel and colleagues tested the invasive capacity of cancer cells co-cultured with CAFs, normal healthy colon fibroblasts and dermal fibroblasts[188]. The authors showed that similarly to CAFs, healthy fibroblasts induced cancer cell elongation, migration and invasion through direct cell-cell contact. This invasion was mediated via fibroblast cell surface associated FGF-2 and FGF receptors and integrin $\alpha_V\beta_5$ - SRC dependent signaling in cancer cells. Assessing the genetic profile between freshly isolated CAFs and normal colonic fibroblasts could identify novel biomarkers identifying specific genetic patterns between invasive and non-invasive tumours.

4.4.3 Normal and tumour vasculogenesis

In the previous Chapter, laminin was added to the stromal component to investigate the effect of the basement membrane on cancer invasion. During metastasis, cancer cells degrade the surround ECM and basement membrane before they reach the vascular supply to travel to distant organs. Therefore, it was decided that the incorporation of laminin is a vital constituent, due to the prerequisite for enhanced cancer invasion and the close proximity of ECs to the basement membrane *in*

vivo[189]. In the stromal only cultures, ECs formed extensive, highly branched end-to-end vascular networks whereas cultures without laminin formed significantly less interconnected vascular networks. This highlights the importance of matrix composition in regulating vasculogenesis. Stamati and colleagues demonstrated end-to-end networks in a model of vasculogenesis in collagen hydrogels using HUVECs and human bone marrow derived stem cells (HBMSCs)[117]. The authors identified an important link between increased VEGFR2 production on ECs, regulated by HBMSCs, which lead to key aggregation patterns in collagen gels in the presence of basement membrane components. It is likely that while no HBMSCs were used in this study, the HDFs provided the ECs with a cocktail of angiogenic growth factors to generate end-to-end networks. It is also interesting to note that laminin was not essential in producing vascular networks in the stromal cultures alone. Its absence lead to significantly longer and wider networks in comparison to the laminin and physiological hypoxia cultures. This could be due to the lack of interconnectivity in comparison to the laminin cultures that leads to longer tubule branches. The differences in width can be attributed to the mixed EC morphology within the collagen only cultures. ECs formed both cobblestones and end-to-end networks.

In biomimetic tumouroids, there were significant differences in the formation of end-to-end networks in comparison to the stromal cultures alone. Firstly, the presence of cancer cells leads to the formation of significantly longer networks in the stroma, albeit considerably less interconnected. These disorganized and broken up vascular tubules mimic the 'leaky' vasculature that is often present within a tumour and the surrounding microenvironment[71]. An interesting observation in biomimetic tumouroids was the reduced multicellular 'wrapping' morphology that was observed in the stromal cultures alone. This is comparable to the structural differences

between normal and tumour vasculature where tumour vessels have highly irregular diameters[190]. This indicates one of two things, or a combination of both; that there are specific cell-cell interactions between the cancer cells which signals ECs to form longer 'leaky' vessels or a chronic overexpression of pro-angiogenic factors secreted by the cancer cells into the surrounding microenvironment that drives these differences in tubule formation. Further work could investigate the release of growth factor release and quantify this in comparison to the absence of cancer cells to identify the exact mechanistic differences between tubule formation. Some groups have made progress in this field[191,192]. Pepin and colleagues have genetically profiled distinct expression profiles between two distinct tumour vasculature subtypes. They identified three genes, MET, ITGAV and PDGFRβ in one subtype and KDR/VEGFR2 in the other subtype that were upregulated. The authors were able to derive a vascular signature between these two distinct tumour vasculature subtypes that was associated to overall disease outcome[192].

Similar to the stromal cultures, two distinct EC morphologies were observed in both the biomimetic tumouroids – cobblestones and end-to-end networks. These two morphologies mimic developmental mechanisms for tubulogenesis[193]. The cobblestone morphology has several tubules that appear to grow out of the EC sheet as evident in the high magnification images in Figure 4.3. From a developmental perspective, this morphology is similar to budding whereby a group of cells from an existing sheet migrate out and form a new tube as the bud extends. On the other hand, the presence of laminin in both normoxia and physiological hypoxia appears to mimic either cell or cord hollowing. In both of these cellular processes, vacuoles or vesicles are involved in creating the lumen of the tubules[193]. In cell hollowing, vacuoles are present in the intracellular spaces between individual cells whereas

vacuoles in cord hollowing are found in the extracellular space of cells. Ultimately, the vacuoles fuse to form a luminal structure. These processes have been studied extensively by a number of groups both *in vitro* and *in vivo*[194,195]. It was not possible to observe whether the vascular networks either in the biomimetic tumouroids or the stromal cultures alone had hollow lumens. Real time imaging of ECs, may be sufficient enough to delineate the exact mechanism of end-to-end EC aggregation in 3D collagen gels. Interestingly, the biomimetic tumouroids cultured in normoxia had a mixed EC morphology within the stroma, again both cobblestones and end-to-end networks. Although it was not studied, it could be due to the upregulation of VEGF by cancer which our lab has previously shown in tumouroids cultured at lower matrix densities[145]. It is highly likely the chronic exposure to pro-angiogenic factors released by the cancer cells leads to the deregulation of the neo-vascularization process where mixed signals are sent to the ECs to form new blood vessels using any possible mechanism.

Biomimetic tumouroids cultured at physiological hypoxia showed no evidence of EC cobblestones. Differential gene expression by EC in the presence of limited oxygen conditions has been shown before indicating transcriptional activation of important angiogenic genes such as HIF-1α, HIF-2α, VEGF-A, Tie2, iNOS and PDGFRβ[196,197]. It is worthwhile noting that biomimetic tumouroids were cultured at physiological hypoxia which is 5% O_2, whereas these studies used 1% and 0.5% O_2 which is more closer to the *in vivo* hypoxia levels of a tumour.

4.4.4 Fibroblast self alignment in 3D collagen

The assembly of collagen type I hydrogels largely produces a randomly oriented fibril network. One of the disadvantages of using PC collagen includes a lack of control of this collagen fibril network. As a tumour develops, the surrounding ECM becomes deregulated and highly disorganized[198]. Cancer cells often lose their differentiation state, cell polarity and as they grow and migrate, come into contact with the surrounding stromal cells. This often leads to acquired mutations in the stroma that promotes the invasion of cancer cells. Our hypothesis was that the fibroblasts within the stromal compartment would be disorganized similarly to the *in situ* biomechanics of a tumour. We investigated the morphology of fibroblasts in the stromal component of our tumouroids. Fibroblast morphology appeared highly disorganized by day 10 as observed in the live/dead stain. However, by day 21, the expression of vimentin showed that fibroblasts appeared highly aligned. While this is surprising, this is not the first instance of cellular self-alignment in collagen gels. Georgiou et al. described the generation of self-aligned collagen gels with a stabilization step involving the removal of interstitial fluid for the development of engineered neural tissue[154]. The development of anisotropic biomaterials is highly desirable in nerve regeneration as it contributes to the nerve repair process. Although the presence of aligned fibroblasts was present in the stromal component, it is worth noting that the cell population used was healthy human dermal fibroblasts. Future work to investigate cellular alignment in our tumouroids would focus on using CAFs, which are known to have a rapid proliferation rate, enhanced collagen production and an upregulation of MMPs involved in ECM degradation[41,174]. The use of CAFs coupled with second harmonic generation (SHG) imaging may provide new insights into the deregulation of the ECM in tumours.

4.4.5 Tumour heterogeneity in tumouroids

As solid tumours grow in a 3D spatial configuration, the cells within a tumour are exposed to varying levels of oxygen and nutrients. This leads to physical and chemical stresses that regulate differential gene expression in cells in different regions within the same tumour. This intratumoural heterogeneity is more analogous to the *in vivo* situation where diffusion limitations result in regions of hypoxic and proliferating cells[199]. We investigated the expression of CK20 as a CRC marker, which is involved in the identification of normal intestinal epithelium and adenocarcinomas and is used routinely in the clinic[200]. In our HT29 tumouroids, we observed a loss of CK20 expression in the invading epithelial cell sheets. This strongly correlated with the overall distance migrated of the invading sheet indicating that loss of CK20 was associated with tumour aggressiveness. This has been recently observed before in a panel of CRC tumours which were immunohistochemically analyzed[201]. Kim and colleagues investigated the pathological and molecular features of microsatellite unstable CRC tumours with different CDX2/CK20 expression statuses. Caudal-type homeobox 2 (CDX2) is another highly specific marker for intestinal epithelial tumours and is involved in proliferation and differentiation of intestinal epithelial cells[202]. The authors found the loss of either CDX2, CK20 or the simultaneous loss of both was significantly related with poor survival between patients with MSI colorectal cancer. Interestingly, while the loss of CK20 is associated with a higher tumour grade and poor differentiation, this does not always imply a worse survival rate as some patients have moderately good prognosis. Lugli and colleagues found the loss of CK20 was associated with a greater number of intratumoural lymphocytes, which have a more favourable prognosis that CK20 positive CRC without intratumoural

lymphocytes[203]. This contradictory nature of The expression of CK20 as a prognostic marker needs to be examined further to determine its specific role in patient outcome, particularly in CRC metastases that may sometimes exhibit a CK20 positive phenotype[204].

While replicating tumour heterogeneity is one of the main aims of reproducing *in vitro* grown tumours, this is often poorly studied within cancer research. Although, the use of 3D cancer models is growing, very few studies have been able to recapitulate the heterogeneity observed within the same cultures. Most studies have focused on differences between cancer cells cultured in 2D and 3D[87,205,206]. This piece of work is the first to observe quantifiable and phenotypic differences in expression of proteins within the same population of cancer cells cultured for prolonged periods of time. While cell lines were only used, it still highlights the usefulness of using the tumouroid model as a suitable platform for intratumoural studies investigating tumour heterogeneity.

4.5 Conclusion

The results presented in this Chapter aimed at optimizing growth of the stromal component and investigating its effect on both cancer invasion and vasculogenesis. According to previous reports, ECs do not survive in co-culture with HDFs when cultured in low-density collagen gels. We have demonstrated that ECs survive in high numbers in dense collagen gels, reflecting the importance of matrix density on cell viability and function. The presence of laminin, the main constituent of the BM, significantly increased and produced the formation of interconnected end-to-end vascular networks in dense collagen gels. As expected, the addition of cancer cells disrupted the interconnectivity of these networks and produced end-to-end networks twice as long as in the stromal co-cultures, mimicking 'leaky' vasculature observed *in vivo*. Surprisingly, the invading HT29 cell sheets into the cellular stroma lost the expression of CK20, which correlated significantly with the overall distance of invasion. Clinical studies have demonstrated that the loss of CK20 by CRC cells corresponds to a higher tumour grade and ultimately a worse prognosis for patients. These results are the first to recapitulate these findings in a tissue-engineered 3D *in vitro* model of CRC.

Chapter Five

Therapeutic treatment in tumouroids

5.1 Introduction

While the majority of preclinical therapeutic testing is carried out in reductionist 2D monolayers, this does not typically mimic the *in vivo* tumour microenvironment scenario accurately. This is particularly relevant for gene expression profiles, which can affect drug efficacy, and oxygen and nutrient gradients that control drug pharmacokinetics. This Chapter outlines the therapeutic efficacy of the EGFR inhibitor cetuximab in HT29 and HCT116 cells cultured both in 2D monolayers and in 10% matrix tumouroids. EGFR is highly upregulated in a variety of solid tumours, particularly in the bowel[20]. The therapy used to target this receptor, the monoclonal antibody cetuximab raised against EGFR, is used extensively in the clinic to treat patients with CRC with relative success[25].

The two colorectal cancer cell lines used for therapeutic, HT29 and HCT116 have known mutational status, which affects the efficacy of cetuximab. HT29 cells, which are KRAS wild type, have been shown to respond to cetuximab therapy while HCT116 *KRAS* mutant are non-responders[207]. This is reflected in patients with KRAS mutant status[26,207,208].

The objective of this Chapter was to validate the use of tumouroids as a suitable drug-screening platform by choosing responder and non-responder cell lines in both 2D and 3D cultures. The expression of EGFR was investigated as a biomarker and compared between monolayers and tumouroids. Furthermore, the objective was to investigate whether the presence of an active stroma influenced the efficacy of cetuximab treatment.

5.2 Materials and Methods

5.2.1 Immunofluorescence

The morphology of HT29 and HCT116 cells was evaluated in 10% matrix tumouroids using immunofluorescence of the cytoskeletal proteins F-actin and tubulin. Briefly, 20,000 cells were seeded in tumouroids and cultured for 14 days. Tumouroids were fixed in 4% paraformaldehyde for 30 minutes and washed thoroughly in PBS (3 washes for 5 minutes each). The cultures were permeabilised with 1% Triton X-100 (TX-100) for 15 minutes and again washed thoroughly with PBS. This was followed by incubation with an anti-tubulin primary antibody solution (Abcam, Cambridge, UK; at 1:200 in a blocking solution of PBS containing 1% BSA and 0.2% TX-100) or CD44 antibody (Abcam, Cambridge, UK; 1:200) overnight at 4ºC. The samples were then washed 3 times in PBS for 5 minutes each and

incubated with a Cy3 conjugated secondary antibody (Jackson Immunoresearch, PA; 1:200), Alexa Fluor 488 conjugated Phalloidin (Invitrogen, Paisley, UK; 1:40) and DAPI diluted in the blocking solution for 2.5 hours at room temperature. The cultures were then washed 3 times with PBS for 5 minutes each and imaged using an Olympus IX71 inverted fluorescent microscope fitted with a Prior z-focus drive.

EGFR expression was also investigated in cells cultured in 2D. Briefly, 350,000 and 300,000 cells/well were seeded in a 6 well plate. Cells were cultured for 48h and fixed using 4% paraformaldehyde for 30 minutes at room temperature. As EGFR is a membrane bound receptor cells were not permeabilised. The staining process is the same as mentioned above for tumouroids. EGFR (Abcam, Cambridge, UK) was used at a concentration 1:1000 as per the manufacturers instructions and the secondary antibody was an Alexa Fluor 488 antibody used at 1:1000.

5.2.2 Cell culture and drug treatment in 2D monolayers and tumouroids

Cells were maintained and routinely passaged as previously described in Section 2.2. For 2D monolayer experiments, HT29 and HCT116 cells were seeded at a density of 32,000 and 30,000 cells/cm^2, respectively. Cells were allowed to grow overnight before being serum-starved for 24h in serum free DMEM. 10% matrix tumouroids were seeded at a density of 20,000 cells (1.96 x 10^6 cells/ml) for both HT29 and HCT116 cell lines. Tumouroids were cultured for 6 days before being serum-starved 24h prior to cetuximab treatment (on day 7). This was done to give the cells time to acclimatize to the new environment and for cellular aggregates to form. Cetuximab (Merck, Darmstadt, Germany) was diluted in serum-free DMEM over a range of concentrations (0.034 – 340nM) immediately prior to treatment and kept on ice. 2D

monolayers were incubated for 48h, while tumouroids were incubated for 72h and 144h in cetuximab. Tumouroids that were treated for 144h had fresh cetuximab added after the first 72h. Controls were treated with serum-free DMEM only. Biomimetic tumouroids were produced in the same manner as those outlined in S Section 4.2.2 and cetuximab treatment was carried out as summarized above.

5.2.3 Gene expression analysis

Gene expression levels of EGFR were measured with one-step quantitative polymerase chain reaction (qRT-PCR) using a LightCycler system (Roche, Hertfordshire, UK). Tumouroids were seeded at 100,000 cells per well (n=4). Cells were collected from 3D collagen gels by digestion in 100-units/ml collagenase (from Clostridium histolyticum) in Tris buffer (Sigma Aldrich, Dorset, UK) for 2 hours. RNA was extracted from cells in either 2D or 3D after 3 days in culture using the RNeasy mini kit (Qiagen, Crawley, UK) according to the manufacturer's instructions. Total RNA was quantified using a nanodrop spectrophotometer measuring at 260/280nm. The EGFR and GAPDH primers that were used are shown in the table below (Table 5.1).

Primer name	Length (Base pairs)	Primer sequence (5' to 3')	Melting point (°C)	GC content (%)
EGFR sense	16	ATCGCAAAGGGCATGA	61.5	50
EGFR antisense	19	CCAGCCCAAAATCTGTGAT	62.5	47.3
GAPDH sense	20	AGATCATCAGCAATGCCTCC	64.2	50
GAPDH antisense	21	AGTGATGGCATGGACTGTGGT	66.8	52.3

Table 5.1: Details and sequences of the primers used for qRT-PCR.

5.3 Results

5.3.1 Cancer cell morphology in tumouroids

The morphology of cells cultured in 10% matrix tumouroids was assessed by immunofluorescence of the cytoskeletal proteins F-actin and tubulin. Tubulin is involved in regulating microtubule based cellular functions such as cell division and intracellular trafficking while the actin filaments primarily drive cellular processes such as cell motility and the maintenance of cell junctions[209]. Figure 5.1 illustrates strikingly distinct morphological features between the cellular aggregates of HT29 and HCT116 cells. HT29 cells formed well-defined tightly bound aggregates with a distinct expression of F-actin at the cell-cell junctions. On the other hand, HCT116 cells formed consistently loose clusters of aggregates with a 'grape-like' phenotype with poor cell-cell adhesion in comparison to HT29 aggregates. The expression of tubulin within HCT116 aggregates was localized to the spindle fibers of dividing cells. The expression of the actin filaments was quantified and revealed a greater level of expression in HT29 aggregates in comparison to HCT116 aggregates (Figure 5.1) which further supports the compact morphology of the HT29 aggregates.

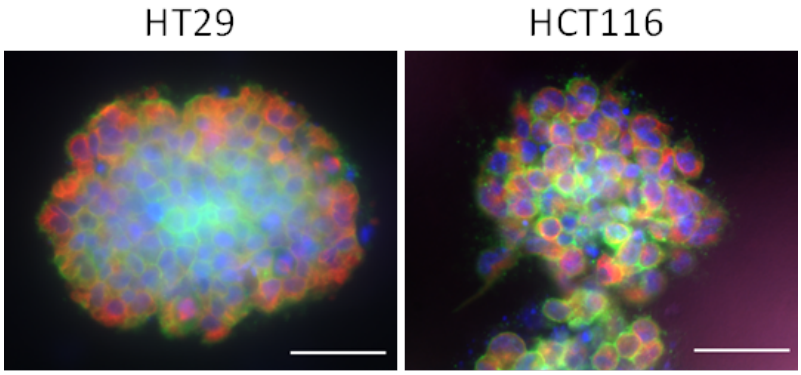

Figure 5.1: Immunofluorescent analysis of cytoskeletal proteins on colorectal cancer cultures. HT29 and HCT116 cells in 3D cultures were maintained for 14 days, fixed and stained for tubulin (red) and F-actin (green – phalloidin). Nuclei were stained with DAPI (blue). Scale bar – 50µm.

5.3.2 Over-expression of EGFR in tumouroids compared to 2D monolayers

Prior to cetuximab treatment, quantitative RT-PCR was carried out on the target receptor, EGFR to investigate any significant differences in mRNA levels between both cell lines cultured in 2D and in tumouroids. As the cells were seeded at different concentrations, which was both cell line dependent and 2D vs. 3D dependent, the EGFR mRNA copy numbers were standardized to 50,000 copies of G6PDH to ensure that likely differences in cell numbers did not interfere with expression levels. EGFR mRNA levels of cells cultured in 2D showed that HCT116 cells expressed double the EGFR level of the HT29 cells (Figure 5.2). This difference was further demonstrated in tumouroids cultured for 3 days, as EGFR expression levels were significantly upregulated in comparison to 2D monolayers. HT29 tumouroids expressed roughly twice the levels of EGFR in comparison to their monolayer counterparts ($p<0.05$). Similarly, HCT116 tumouroid EGFR expression increased approximately 3-fold in comparison to 2D ($p<0.01$).

Further analysis of EGFR expression was carried out using immunofluorescence to investigate whether the EGFR mRNA is translated to protein and expressed. Immunofluorescent analysis demonstrated in 2D that HCT116 cells expressed more EGFR than HT29 cells (Figure 5.2). Although this was also carried out in tumouroids, the staining was not successful after several attempts (Figure 5.2). As the mRNA levels confirmed that EGFR levels were significantly higher in tumouroids in comparison to 2D monolayers, these experiments aimed at comparing the translated protein levels of EGFR in both monolayers and tumouroids. While the immunofluorescent staining was successfully carried out in 2D monolayers, there were technical issues with the staining process in the tumouroids. HT29 and HCT116 cells were cultured in 10% matrix tumouroids for 14 days and immunofluorescently

stained for EGFR. The antibody failed to adequately stain both cell lines and was repeated on three separate occasions. Possible reasons for this are explained later in the discussion.

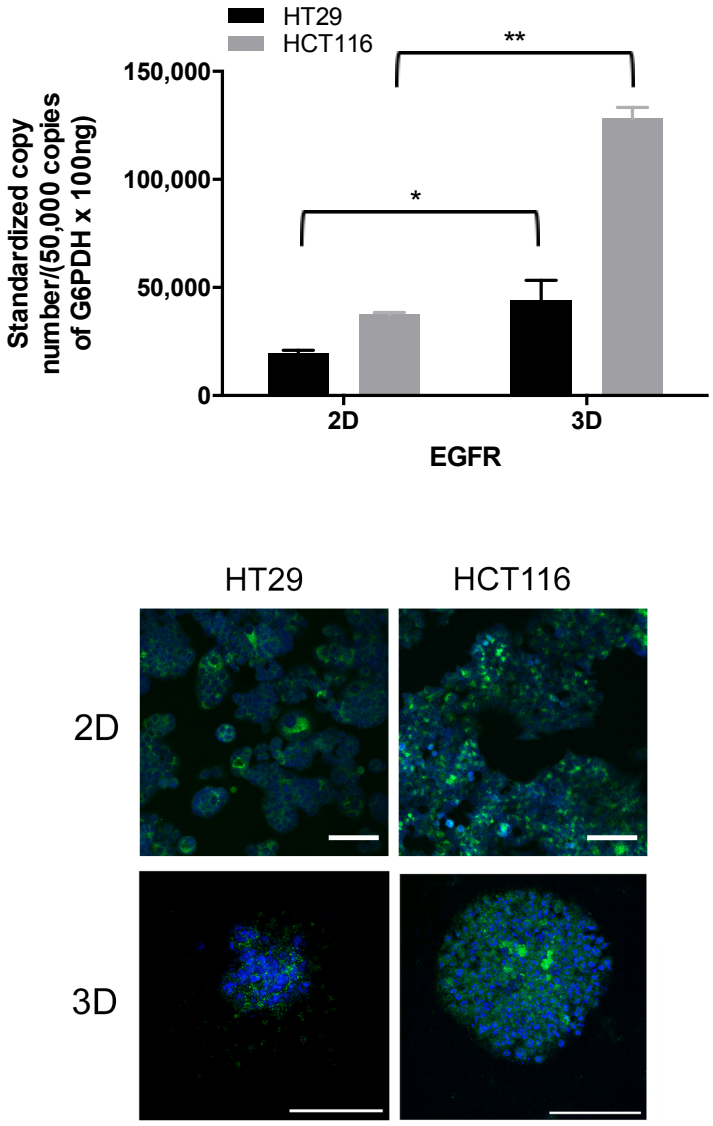

Figure 5.2: Quantitative RT-PCR analysis of EGFR mRNA levels in colorectal cancer cells and immunofluorescent expression of EGFR. HT29 and HCT116 cells were cultured for 3 days in either 2D or in 3D cultures. RNA was extracted, quantified and qRT-PCR was performed using G6PDH as a housekeeping gene. EGFR expression was also examined using immunofluorescence in 2D and tumouroids. HCT116 EGFR expression was higher than HT29 cells in monolayers while EGFR expression was not detected in tumouroids. Data is presented as the mean ± SD (n=3). * $p < 0.05$; ** $p < 0.01$. Scale bar – 100µm.

5.3.3 Cetuximab treatment in 2D monolayers and tumouroids

To determine cetuximab efficacy, HT29 and HCT116 cells cultured in 2D and in tumouroids were treated for 48h and 72h respectively and growth inhibition was assessed by the alamarBlue assay. The difference in time between treatments in 2D and 3D is due to the differences in pharmacokinetics of drugs on a flat monolayer of cells in comparison to a 3D structure, which acts as a physical barrier to the drug. It has also been shown previously that this timeline is the optimum time to instigate the maximum effect of the drug, particularly in 3D cultures[210].

In 2D monolayers, a concentration of 0.34nM of cetuximab resulted in a 60% reduction in proliferation of HT29 cells compared to untreated controls ($p<0.001$), while HCT116 cells appeared to be non-responsive (Figure 5.3). Interestingly, at higher concentrations (3.4nM), HCT116 cell proliferation increased slightly in response to cetuximab treatment; however this was not statistically significant. Cetuximab was significantly less effective in HT29 tumouroids demonstrating a maximum of 40% reduction in proliferation at 3.4nM ($p<0.01$) while again HCT116 tumouroids were non-responsive at all concentrations (Figure 5.4)

As a secondary measure response to cetuximab treatment, the sizes of cellular aggregates within the ACM were measured after treatment to assess the impact on cell proliferation (Figure 5.4). A dose dependent decrease in the surface area of cellular aggregates broadly correlated with treatment efficacy as measured by alamarBlue. At a concentration of 3.4nM, HT29 cellular aggregates were 35% smaller in size ($p<0.05$) in comparison to untreated controls. HCT116 aggregate size remained largely unaffected by cetuximab at any of the concentrations.

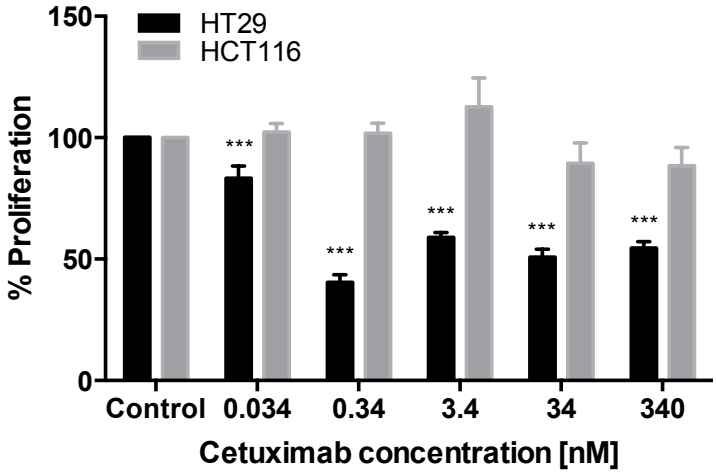

Figure 5.3: The efficacy of cetuximab on HT29 and HCT116 cells cultured in 2D. HT29 and HCT116 cells were treated with cetuximab at a range of concentrations for 48h and their proliferation was assessed by alamarBlue. Data is presented as the mean ± SD (n=4). *** $p<0.001$.

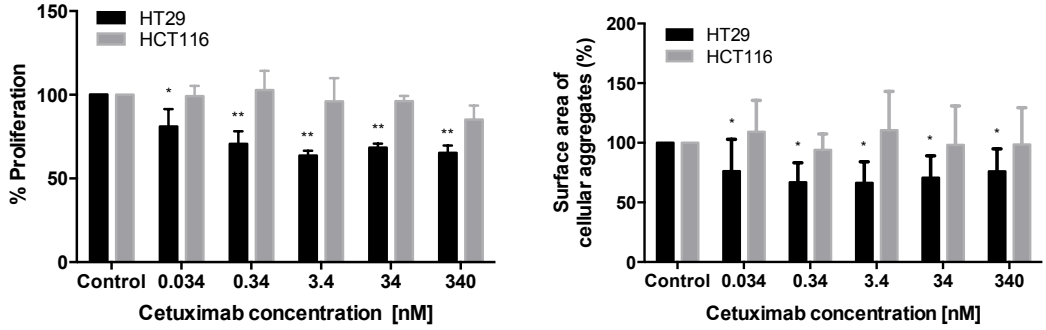

Figure 5.4: The inhibitory effect of cetuximab in tumouroids. HT29 and HCT116 tumouroids were cultured for 7 days before being treated with cetuximab for 72h with increasing concentrations of cetuximab. Tumouroids were then fixed and the surface area of 10 random cellular aggregates was measured using the ImageJ software and calculated as a percentage of the control. Data is presented as the mean ± SD. * $p < 0.05$, ** $p < 0.01$.

5.3.4 Drug treatment in biomimetic tumouroids

As HCT116 cells are KRAS mutant and resistant to cetuximab treatment, the following experiments were carried out in HT29 tumouroids with a cellular surround containing HDF and HUVEC cells. Biomimetic tumouroids were created as outlined in Section 4.2.2.

Biomimetic tumouroids were cultured for 6 days prior to 24h serum starvation and 72h and 144h cetuximab treatment. Cetuximab had a maximum inhibitory effect of 12% at 340nM (Figure 5.5) at 72h while the longer exposure at 144h had resulted in an overall of 7% reduction in proliferation. Although this appeared statistically significant ($p<0.0001$), cetuximab was largely ineffective at instigating a similar effect to the cancer cell only tumouroids in Section 5.3.3. The resistance of HT29 cells in this instance to cetuximab was further supported by the absence of dead cells at all concentrations (3.4nM-340nM) following a live/dead stain post treatment for 72h.

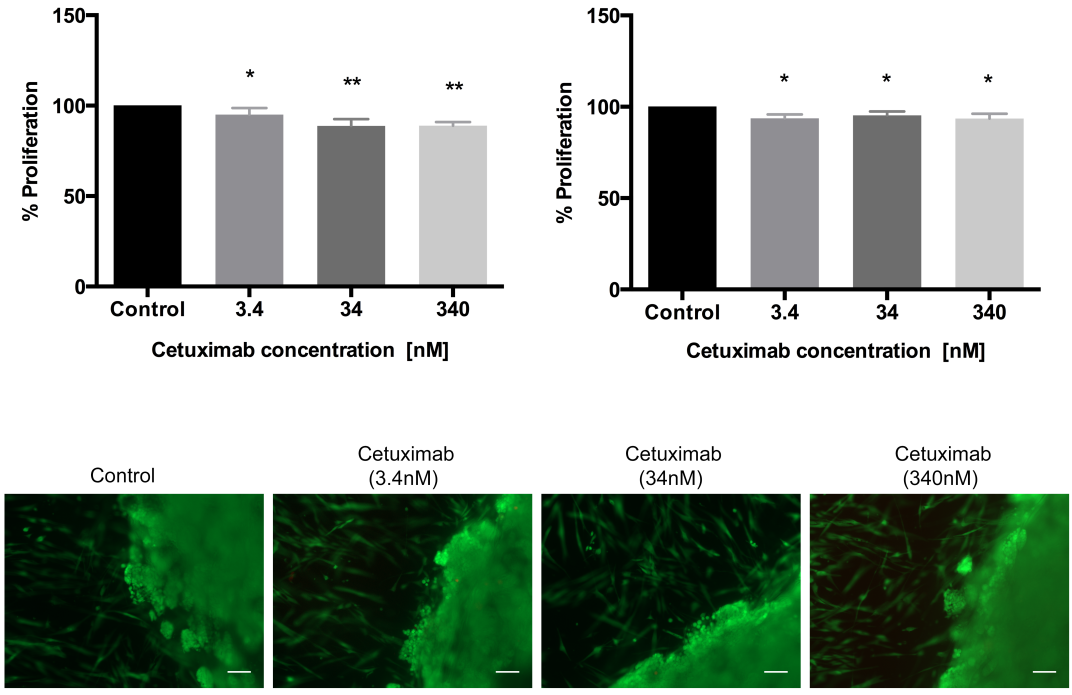

Figure 5.5: The effect of cetuximab on cellular stromal surround tumouroids. Tumouroids were treated with cetuximab for 72h or two consecutive doses of cetuximab for 72h and the metabolic activity was assessed by alamarBlue (n=8). A live/dead (green/red) stain was then used to further assess the inhibitory effect of tumouroids after treatment with cetuximab for 72h. Data is presented as the mean ± SD. Scale bar – 100µm. * $p < 0.05$; ** $p < 0.0001$

5.3.5 Cetuximab resistance in HT29 cells and overexpression of CD44 in tumouroids in comparison to 2D monolayers

Due to a lack of inhibition by cetuximab in Section 5.3.4, drug treatment was repeated again in 2D monolayers where there previously was a 60% inhibition of proliferation. Cetuximab failed to produce a similar inhibitory effect when treated at the same concentrations as Section 5.3.3 (Figure 5.6). Although the experiments were carried out at different times, it should still be expected to instigate a similar effect. Inhibition of proliferation by cetuximab between the concentrations 3.4nM – 340nM resulted in a maximum of 12% inhibition, which appeared to be statistically significant.

In order to further investigate the newly acquired resistance of HT29 cells to cetuximab, the expression of CD44 was explored as a possible mechanism of resistance due to its function as a cancer stem cell marker (Figure 5.6). CD44 was expressed in HT29 cells in both 2D and in tumouroids. However, there was a higher expression level in tumouroids in comparison to 2D. There was also a heterogeneous level of expression of CD44 within individual aggregates indicating different subpopulations of cancer stem cells residing within the tumouroids.

a

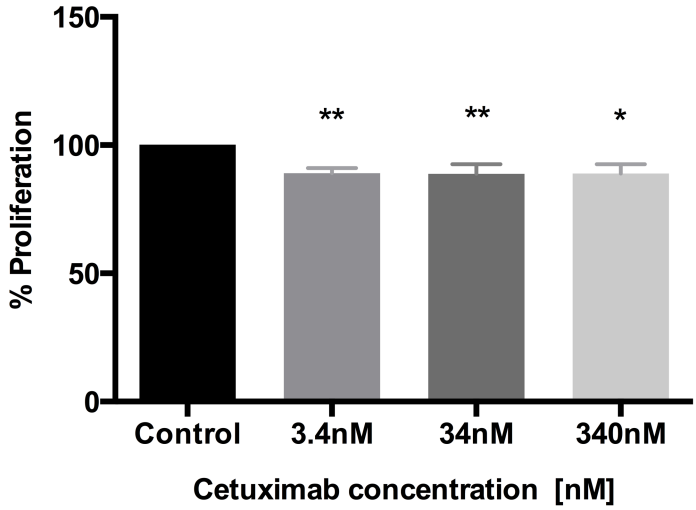

b

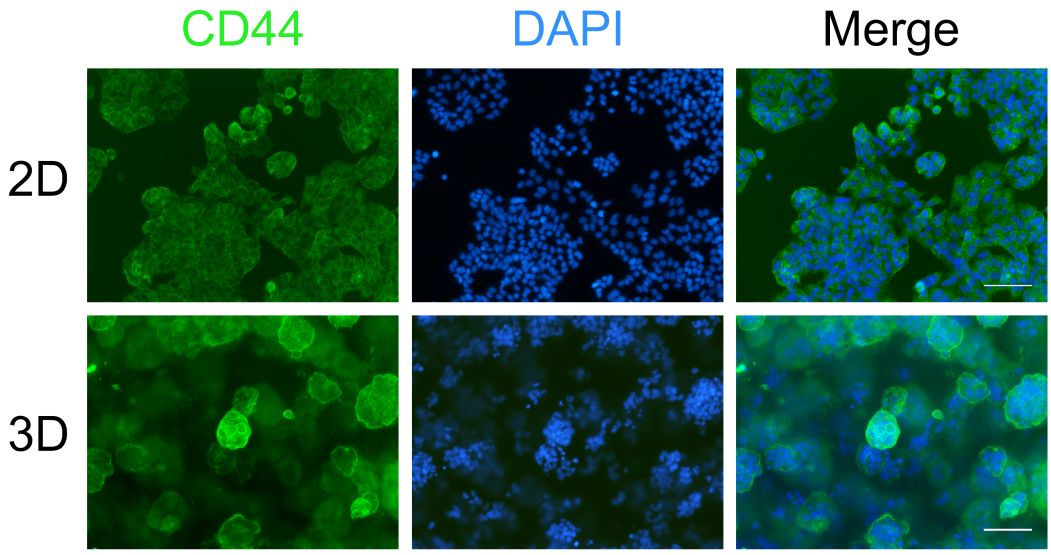

Figure 5.6: Cetuximab resistance in HT29 monolayers. (a) HT29 cells treated with cetuximab at 3.4nM – 340nM for 48h displayed and the alamarBlue assay was used to measure response to drug treatment. (b) The expression of CD44 was also investigated (green) in HT29 cells in 2D and 3D as a marker for cancer stem cells and cetuximab resistance. Data is presented as the mean ± SD (n=8). * $p < 0.05$; * $p < 0.01$. Scale bar – 100µm.

5.4 Discussion

The work in this Chapter focuses on translating the tumouroid model into a platform for testing anti-cancer therapeutics. The principal aim is to have an amenable, complex *in vitro* tumour model, which bridges the gap between 2D reductionist cell culture and animal models. Using these 3D tumour models will allow us to mimic certain *in vivo* parameters such as the stiffness of tumour microenvironment while maintaining the simplicity of *in vitro* cultures.

5.4.1 Invasive and non-invasive morphologies in colorectal cancer tumouroids

Prior to drug testing, the morphologies of both HT29 and HCT116 cells in 10% matrix tumouroids was evaluated by immunofluorescently staining the cytoskeletal proteins tubulin and F-actin. This was done to evaluate the organization of the actin filaments, which is involved in cell clustering during cell aggregate formation and also to establish whether these morphologies in EGFR positive cells play a role in cetuximab resistance.

HT29 and HCT116 cells formed moderately distinct cellular aggregates. HT29 cells formed tight compact cellular aggregates characterized by disorganized nuclei and strong cell-cell adhesion while HCT116 cells formed loosely bound clusters of cells with poor cell-cell adhesion. These two types of morphologies cells have been previously observed in a recent study investigating breast cancer cell morphology in 3D[211]. The authors cultured an extensive panel of breast cancer cell lines in 3D and characterized 4 distinct morphologies; round, mass, grape-like and stellate. In this instance the HT29 and HCT116 cells formed mass and grape-like morphologies respectively. The expression of tubulin was localized to the outer periphery of the

HT29 cellular aggregates, indicating a more heterogeneous expression than HCT116 cells. However, this may represent an inability of the antibody to penetrate thoroughly into the cellular aggregates, as they appear tightly bound. The penetration of antibodies and large molecules in both 3D *in vitro* culture systems and *in situ* tissues has always poised significant issues. Xiang *et al.* have investigated this extensively by treating a spheroid model of mesothelioma with a fluorescently labeled SS1P immunotoxin antibody and tracked its penetration over 16h. They reported the restricted penetration of SS1P, which was localized to the outer periphery of the spheroids following the first 4h of treatment, indicating inadequate infiltration to the core.

Kenny and colleagues found that eight of the nine breast cancer cells that formed a grape-like phenotype similar to the HCT116 cells were isolated from invasive tumour metastases. This indicates an acquired ability to metastasize to other tissues over the course of their evolution. This supports the reported invasive behaviour of HCT116 cells in comparison to HT29 cells[146]. This is further supported by the presence of cellular protrusions in HCT116 aggregates which are involved in cell migration[212]. Occasionally these migratory fronts are driven by chemotactic responses that can stimulate intracellular pathways such as EGFR. A recent study by Patsialou *et al.* determined macrophage dependent invasion of breast cancer cells in a mouse model driven by an EGF/CSF-1 paracrine loop between cancer cells and macrophages[213]. The implication of these cellular protrusions in our 3D tumouroid model may signify underlying autocrine signaling pathways involved in the migration of HCT116 cells in stiff collagen matrices.

5.4.2 EGFR overexpression in tumouroids

When cetuximab was first developed, it was assumed that the expression of EGFR would be taken as pre-requisite for cetuximab therapy. It is now known that this is not the case[26]. However, the mRNA and protein levels of EGFR were still evaluated in our tumouroids and in 2D monolayers. HT29 and HCT116 (low and high expressing cell lines respectively) mRNA expression of EGFR were compared and were greatly enhanced in 3D culture in comparison to 2D monolayers. This was also confirmed by immunofluorescence of EGFR in 2D. Immunofluorescence of EGFR in tumouroids was not possible due to an inability of the antibody to stain the cells and ultimately did not show up any expression.

These results suggest that in 3D, the EGFR levels are upregulated due to intrinsic features present within the microenvironment of the tumouroids. This may be due to the strong presence of cell-cell or cell-matrix interactions in addition to the presence of hypoxia that may stimulate a signaling cascade to upregulate EGFR levels in response to low oxygen conditions to encourage cell proliferation. There have been conflicting results with regards to EGFR expression in 2D and 3D cultures. One such study by Franovic *et al.* demonstrated tangible increases in EGFR levels in 3D compared to 2D dependent on both the use of 3D cultures and oxygen levels in a range of brain, prostate and breast cancer cell lines[214]. Another study carried out by Luca and colleagues in colorectal cancer cells found that several genes involved in proliferation were downregulated in 3D including EGFR[205]. The authors postulated this could be due to microenvironmental factors impairing the expression of proliferation genes such as those of the EGF family. While these differences exist and there is no clear solution, it is important to note that cetuximab efficacy is not

dependent on EGFR expression and this should be taken into consideration prior to cetuximab treatment[215].

5.4.3 Cetuximab efficacy in tumouroids and 2D monolayers

In order to explore the therapeutic potential of tumouroids for drug screening, tumouroids were cultured as described in Section 5.2.2 and treated with increasing concentrations of cetuximab. Alongside the proliferation assay, alamarBlue, the surface area of cellular aggregates was used a secondary measure of drug efficacy. We have already determined that HT29 and HCT116 cells express low and high levels of EGFR respectively. The next step was to evaluate their response to the anti-EGFR therapy, cetuximab.

In recent years it has become more apparent *KRAS* mutant status is a much more effective indicator of response to cetuximab treatment[26]. The HT29 cell line has a positive EGFR status and wild-type *KRAS* status whereas the HCT116 cell line is *KRAS* mutant. As expected, cetuximab was effective on HT29 cells in both 2D and in tumouroids displaying a maximum 60% inhibition in 2D and 40% in 3D. However the inhibitory effect was limited at high concentrations under both conditions. This could be due to several reasons. It has been suggested that cetuximab functions through immune dependent mechanisms, which increases the overall efficacy of cetuximab *in vivo*[216]. Therefore, the reported efficacy of cetuximab here may be lessened due to the lack of a functional immune component within the tumouroids. Hsu *et al.* demonstrated in a xenograft model of non-small cell lung cancer that increased cetuximab toxicity was driven by an immune dependent mechanism known as antibody dependent cellular cytotoxicity (ADCC). They postulated that it was due

to complement-dependent cytotoxicity, which releases anaphylatoxins such as C5a that increases the recruitment and activation of effector cells to the tumour site.

Interestingly, therapeutic treatment in both 2D monolayers and in tumouroids illustrates that cetuximab does not follow a conventional linear drug inhibition curve with drug inhibition limited at increasing concentrations. This is well established and has been previously observed in both clinical trials and *in vitro* studies[24,217]. While there is no reason given for the *in vitro* scenario, it has been postulated that cetuximab follows non-linear, dose dependent pharmacokinetics due to reaching saturation levels in the serum. EGFR antibodies such as cetuximab and panitumumab are subject to a saturable antigen-specific elimination process based on the internalization of the EGF ligand-receptor complex and are subsequently removed from circulation[218].

As anticipated, cetuximab was less effective in 3D than in 2D. Drug pharmacokinetics plays an important role in the delivery mechanism of most anti-cancer therapeutics, particularly within 3D cultures and *in vivo* tumour models. Tumouroids displayed a degree of 'resistance' to drug treatment in comparison to 2D monolayers. The formation of 3D cellular structures in the tumouroids can function to obstruct the penetration of large molecules and antibodies into the core of the aggregates, mimicking the *in vivo* drug barrier present in tissues. Hence, improving the penetration or relying on more targeted treatments such as nanoparticles will be vital in maximizing the therapeutic potential while minimizing the toxicity of these agents to surrounding healthy tissue[87,219].

In line with the *KRAS* mutant status, HCT116 cells were resistant in both 2D monolayers and tumouroids to cetuximab treatment. Interestingly, at 0.34nM, cetuximab appeared to stimulate the proliferation of HCT116 cells in tumouroids.

However, this growth was very limited and did not appear to be statistically significant. The increases were not substantial enough to lead us to investigate this further, however this may be due to paradoxical activation of the *MAPK* pathway. Normally, in BRAF (V600E) tumours, inhibitors of the MAPK pathway block downstream signaling and prevent cell proliferation decreasing overall tumour growth. A recent study by Hatzivassiliou and colleagues showed that RAF inhibitors used in *KRAS* mutant tumours activate the RAF-MEK-ERK pathway in a *RAS* dependent manner thus increasing tumour growth in some models of cancer[220]. This was due to direct conformational changes of inhibitors on the RAF kinase domain, which in some instances can have the opposite of intended effect. It is interesting to note, there was no such pattern observed in the 2D HCT116 cultures, highlighting further potential advantages of using more relevant 3D *in vitro* models.

5.4.4 Drug treatment in biomimetic tumouroids and resistance to cetuximab

The following experiments were carried out only in the HT29 cell lines due to the non-responsive nature of HCT116 cells to cetuximab. Tumouroids were constructed using the HT29 cell lines in the ACM and HDF and HUVEC cells in the stromal surround as outlined in Section 4.2.2. The aim of these experiments was to investigate whether the presence of a biomimetic stroma influenced the efficacy of drug treatment. Tumouroids were allowed to mature for 7 days before either 72h or 144h treatment of cetuximab at increasing concentrations. Although the initial response to cetuximab was promising, these more recent results provide some conflicting data. Treatment with cetuximab for 72h displayed high levels of resistance at all concentrations with a maximum of 12% inhibition at the highest

concentration (340nM). This was further supported by the absence of dead cells in live/dead stain carried out on treated cultures in addition to prominent invasion witnessed at day 10. The next step was to investigate the effect of long-term drug exposure (144h) on tumouroids. This is particularly difficult in 2D monolayer due to fast growing nature of cells as they reach confluency in a much shorter period due to contact inhibition. Surprisingly, cetuximab treatment at 144h elicited less of a response than 72h with a maximum inhibition of 7%. Although this appeared statistically significant, this is most likely due to a high number of repeats which appeared to skew the p values below 0.05. To ensure this was not an artifact caused by the presence of stromal cells, cetuximab treatment was repeated in 2D monolayers to ensure efficacy in HT29 cells. Again, HT29 cells were resistant in 2D indicating a newly acquired mechanism of resistance within these cells independent of 2D or 3D culture.

There could be several reasons due to this new mechanism of cetuximab resistance. Firstly, HT29 cells are a BRAF V600E mutation cell line, which has been shown to be associated with a lack of response in wild type *KRAS* tumours in patients with colorectal cancer[25,30,221]. It is important to note that the cetuximab sensitive and resistant experiments were carried out at different times during the course of this work and over time the cell line may have mutated to become more resistant. In contrast to the presence of the V600E mutation, there have been numerous groups, which have reported HT29 response to cetuximab[24,222]. Although this data is conflicting, there has been no hypothesis put forward to the contrasting nature of cetuximab in HT29 cells.

The next step was to investigate a mechanism, which may contribute to the resistance of HT29 cells to cetuximab. CD44 was investigated as a possible biomarker of

resistance due to its functional role as an important cancer stem cell marker[223]. It is regulated via the β-catenin/Tcf-4 signaling pathway and is particularly upregulated in colorectal cancer precursor legions indicating a role in intestinal tumourigenesis and EMT induction[224]. We found that CD44 was expressed in HT29 cells both in 2D and in tumouroids. However, it is interesting to note that CD44 was highly expressed in tumouroids, particularly within specific sub-populations of cellular aggregates. La Fleur and colleagues investigated the emergence of drug resistance in a model of head and neck squamous cell carcinoma (HNSCC) by identifying $CD44^{low}$, $CD44^{high}/EGFR^{high}$ and $CD44^{high}/EGFR^{low}$ cell sub-populations[225]. The authors found that $CD44^{high}/EGFR^{low}$ expressing cells displayed a degree of resistance to the anti-EGFR therapies cetuximab and gefitinib. It was postulated that the cells with this phenotype modulate cell signaling by the BCR/ABL and Src family tyrosine kinases due to their sensitivity to dasatinib. While it is important to reiterate this work was carried out in HNSCC, it is likely that the same mechanism may contribute to cetuximab resistance in HT29 cells.

5.5 Conclusion

The results presented in this Chapter describe and validate the use of our tissue-engineered tumouroids as a suitable drug-screening platform. Cancer cells form tumour-like cellular aggregates with visible cell-cell junctions *in vitro*, similarly to the *in vivo* scenario. The expression of the biomarker, EGFR, was examined and found to have significantly elevated mRNA levels in tumouroids in comparison to monolayers. HT29 and HCT116 cells responded to cetuximab treatment in accordance with their *KRAS* status. Cetuximab treatment was more effective in 2D monolayers than in 3D tumouroids. When the cellular stroma containing fibroblasts and ECs was incorporated, HT29 cells became resistant to cetuximab treatment. However, this appeared to be attributed to the reported *BRAF* mutant status of HT29 cells in addition to the upregulation of the CSC marker CD44 that contributes significantly to cetuximab resistance in CRC.

Chapter Six

Conclusions

The research presented in this thesis has made significant contributions in developing a biomimetic 3D *in vitro* tumour model. While 2D cell culture remains the current gold standard for delineating biochemical and molecular mechanisms of cancer cells, it does not factor in the vital role of the ECM in cancer progression. Although our tumouroids lack the full complexity of animal models, this model is cost and time effective, allows for easy manipulation of cell and matrix densities and exhibits characteristics of the native *in vivo* tumour microenvironment. The research presented here shows for the first time behavioural characteristics of cancer cells in physiologically relevant collagen matrices. Furthermore, the presence of a reactive stroma populated with both fibroblasts and ECs incorporates the influence of the stroma in both cancer invasion and the formation of vascular networks.

This research investigated the effect of ECM density and composition on cancer invasion. The novelty of this tumour model is its compartmentalization, mimicking

both the cancer mass and the stroma of a tumour. The research presented here is the first to investigate the migration of cancer cells from a 'dense' cancer mass of collagen I into an engineered stroma composed of collagen I of varying densities and known concentrations of basement membrane components. We are the first to describe changes in the invasion pattern of cancer cells, from spherical cell aggregates to cell sheets, dependent upon the stromal composition and density. These changes in cell morphology were associated with an epithelial to mesenchymal transition of cancer cells.

Furthermore, the incorporation of a cellular stroma highlights the importance of the presence of 'healthy' cells in the local tumour microenvironment. The development of a vascular network, although non-functioning in this instance, is essential to a growing tumour. The presence of normal HDFs was shown to promote the formation of these vascular networks. We have shown here for the first time, differences in the aggregation of ECs driven by both matrix composition and the presence of cancer cells. Cancer cells lead to disconnected end-to-end vascular networks with irregular diameters, mimicking leaky vasculature, often a defining characteristic of *in vivo* tumour vasculature. The loss of expression of important colorectal epithelial markers such as CK20 by invading cancer cells also highlights the heterogeneity of the tumouroids. The loss of CK20 is observed widely in the clinic and to date, this model is the only one to recapitulate sophisticated cellular behaviours and to correlate it with tumour aggressiveness.

Targeting tumours in a 3D environment is one of the main goals of developing more biomimetic *in vitro* models. Investigating the effect of therapeutic agents on cancer cells in a 3D spatial configuration is vital to developing more targeted and efficient therapies. Using cetuximab, we have shown major differences in the efficacy

between 2D monolayers and 3D tumouroids, independent of EGFR expression levels. This hindrance of the stiff collagen matrix in addition to the cell aggregates may have acted as a barrier to hinder the penetration of cetuximab mimicking the *in vivo* drug barrier in tissues.

Further development of the tumouroid model would include the incorporation of an immune component. It has become increasingly that certain immunotherapies are more effective when cells such as lymphocytes are present. While cell lines provide an invaluable amount of information, the use of patient derived cells would also help to recapitulate the *in vivo* scenario even more closely. This could include the effect of CAFs and their function in promoting cancer invasion. Delineating the molecular mechanisms of end-to-end aggregation of ECs will also provide new information to possibly target the tumour vasculature by developing inhibitors that may disrupt neovascularization mechanisms hijacked by cancer cells during tumourigenesis.

In summary, the work presented in this thesis has positively contributed to our understanding of the ECM and its role in cancer progression. Establishing the foundation of cancer cell behaviour in a biomimetic environment will prove fundamental in paving the route for personalized medicine as a realistic alternative in cancer therapy.

Chapter Seven

Bibliography

[1] Torre LA, Bray F, Siegel RL, Ferlay J, Lortet-tieulent J, Jemal A. Global Cancer Statistics, 2012. CA a cancer J Clin. 2015;65(2):87–108.

[2] Center MM, Jemal a., Smith R a., Ward E. Worldwide variations in colorectal cancer. Dis Colon Rectum. 2010;53:1099.

[3] Boyle P, Langman JS. ABC of colorectal cancer: Epidemiology. BMJ. 2000;321(7264):805–8.

[4] Lipkin M. Phase 1 and phase 2 proliferative lesions of colonic cells in diseases leading to colonic cancer. Cancer. 1974;(34):878–88.

[5] Anti M, Marra G, Armelao F, Percesepe A, Ficarelli R, Ricciuto GM, et al. Rectal epithelial cell proliferation patterns as predictors of adenomatous colorectal polyp recurrence. Gut. 1993;34:525–30.

[6] Hill MJ, Morson BC, Bussey HJ. Aetiology of adenoma--carcinoma sequence in large bowel. Lancet. 1978;1:245–7.

[7] Bosman F, Yan P. Molecular pathology of colorectal cancer. Pol J Pathol. 2014;65(4):257–66.

[8] Muleris M, Salmon RJ, Dutrillaux AM, Vielh P, Zafrani B, Girodet J, et al. Characteristic chromosomal imbalances in 18 near-diploid colorectal tumors. Cancer Genet Cytogenet. 1987;29(2):289–301.

[9] Vasen HFA, Möslein G, Alonso A, Aretz S, Bernstein I, Bertario L, et al. Guidelines for the clinical management of familial adenomatous polyposis (FAP). Gut. 2008;57(5):704–13.

[10] Fodde R, Smits R, Clevers H. APC, signal transduction and genetic instability in colorectal cancer. Nat Rev Cancer. 2001;1(1):55–67.

[11] Lynch HT, Lynch JF, Lynch PM, Attard T. Hereditary colorectal cancer syndromes: molecular genetics, genetic counseling, diagnosis and management. Fam Cancer. 2008;7(1):27–39.

[12] Rubinfeld B, Albert I, Porfiri E, Fiol C, Munemitsu S, Polakis P. Binding of GSK3b to the APC-b-catenin complex and regulation of complex assembly. Science (80-). 1996;272(5264):1023–6.

[13] Fevr T, Robine S, Louvard D, Huelsken J. Wnt/beta-catenin is essential for intestinal homeostasis and maintenance of intestinal stem cells. Mol Cell Biol. 2007;27(21):7551–9.

[14] Logan CY, Nusse R. The Wnt Signaling Pathway in Development and Disease. Annu Rev Cell Dev Biol. 2004;20(1):781–810.

[15] Komiya Y, Habas R. Wnt signal transduction pathways. Organogenesis. 2008;4(2):68–75.

[16] Mead LJ, Jenkins MA, Young J, Royce SG, Smith L, St. John DJB, et al. Microsatellite Instability Markers for Identifying Early-Onset Colorectal Cancers Caused by Germ-Line Mutations in DNA Mismatch Repair Genes.

Clin Cancer Res. 2007;13(10):2865–9.

[17] Cunningham JM, Christensen ER, Tester DJ, Kim CY, Roche PC, Burgart LJ, et al. Hypermethylation of the hMLH1 promoter in colon cancer with microsatellite instability. Cancer Res. 1998;58(15):3455–60.

[18] Messa C, Russo F, Caruso MG, Leo A Di. EGF, TGF-a, and EGF-R in Human Colorectal Adenocarcinoma. Acta Oncol (Madr). 1998;37(3):285–9.

[19] Citri A, Yarden Y. EGF–ERBB signalling: towards the systems level. Nat Rev Mol Cell Biol. 2006;7(7):505–16.

[20] Nicholson R., Gee JM., Harper M. EGFR and cancer prognosis. Eur J Cancer. 2001 Sep;37:9–15.

[21] Resnick MB, Routhier J, Konkin T, Sabo E, Pricolo VE. Epidermal growth factor receptor, c-MET, beta-catenin, and p53 expression as prognostic indicators in stage II colon cancer: a tissue microarray study. Clin Cancer Res. 2004;10(9):3069–75.

[22] Spano JP, Fagard R, Soria J-C, Rixe O, Khayat D, Milano G. Epidermal growth factor receptor signaling in colorectal cancer: preclinical data and therapeutic perspectives. Ann Oncol. 2005;16(2):189–94.

[23] Lee J, Lee I, Han B, Park JO, Jang J, Park C, et al. Effect of simvastatin on cetuximab resistance in human colorectal cancer with KRAS mutations. J Natl Cancer Inst. 2011 Apr 20;103(8):674–88.

[24] Matsuo T, Nishizuka SS, Ishida K, Iwaya T, Ikeda M, Wakabayashi G. Analysis of the anti-tumor effect of cetuximab using protein kinetics and mouse xenograft models. BMC Res Notes. 2011 Jan;4(1):140.

[25] Di Nicolantonio F, Martini M, Molinari F, Sartore-Bianchi A, Arena S, Saletti P, et al. Wild-Type BRAF Is Required for Response to Panitumumab or Cetuximab in Metastatic Colorectal Cancer. J Clin Oncol. 2008;26(35):5705–

12.

[26] Lièvre A, Bachet J-B, Le Corre D, Boige V, Landi B, Emile J-F, et al. KRAS mutation status is predictive of response to cetuximab therapy in colorectal cancer. Cancer Res. 2006 Apr 15;66(8):3992–5.

[27] Imamura Y, Morikawa T, Liao X, Lochhead P, Kuchiba A, Yamauchi M, et al. Specific Mutations in KRAS Codons 12 and 13, and Patient Prognosis in 1075 BRAF Wild-Type Colorectal Cancers. Clin Cancer Res. 2012;18(17):4753–63.

[28] Vaughn CP, Zobell SD, Furtado L V., Baker CL, Samowitz WS. Frequency of KRAS, BRAF, and NRAS mutations in colorectal cancer. Genes Chromosom Cancer. 2011;50(1):307–12.

[29] Wellbrock C, Karasarides M, Marais R. The RAF proteins take centre stage. Nat Rev Mol Cell Biol. 2004;5(11):875–85.

[30] Pietrantonio F, Petrelli F, Coinu A, Bartolomeo M Di, Borgonovo K, Maggi C, et al. Predictive role of BRAF mutations in patients with advanced colorectal cancer receiving cetuximab and panitumumab: A meta-analysis. Eur J Cancer. 2015;51(5):587–94.

[31] Peddareddigari VG, Wang D, Dubois RN. The tumor microenvironment in colorectal carcinogenesis. Cancer Microenviron. 2010;3(1):149–66.

[32] Landskron G, De la Fuente M, Thuwajit P, Thuwajit C, Hermoso MA. Chronic inflammation and cytokines in the tumor microenvironment. J Immunol Res. 2014;2014:149185.

[33] Valiathan RR, Marco M, Leitinger B, Kleer CG, Fridman R. Discoidin domain receptor tyrosine kinases: new players in cancer progression. Cancer Metastasis Rev. 2012;31(1-2):295–321.

[34] Lu P, Takai K, Weaver VM, Werb Z. Extracellular matrix degradation and

remodeling in development and disease. Cold Spring Harb Perspect Biol. 2011;3(12).

[35] de Visser KE, Eichten A, Coussens LM. Paradoxical roles of the immune system during cancer development. Nat Rev Cancer. 2006;6(1):24–37.

[36] Ween MP, Oehler MK, Ricciardelli C. Role of versican, hyaluronan and CD44 in ovarian cancer metastasis. Int J Mol Sci. 2011;12:1009–29.

[37] Yu H, Mouw JK, Weaver VM. Forcing form and function: biomechanical regulation of tumor evolution. Trends Cell Biol. 2011;21(1):47–56.

[38] Calvo F, Ege N, Grande-Garcia A, Hooper S, Jenkins RP, Chaudhry SI, et al. Mechanotransduction and YAP-dependent matrix remodelling is required for the generation and maintenance of cancer-associated fibroblasts. Nat Cell Biol. 2013;15(6):637–46.

[39] Turley SJ, Cremasco V, Astarita JL. Immunological hallmarks of stromal cells in the tumour microenvironment. Nat Rev Immunol. 2015;15(11):669–82.

[40] Haggar FA, Boushey RP. Colorectal cancer epidemiology: Incidence, mortality, survival, and risk factors. Clin Colon Rectal Surg. 2009;22(4):191–7.

[41] Catalano V, Turdo A, Di Franco S, Dieli F, Todaro M, Stassi G. Tumor and its microenvironment: a synergistic interplay. Semin Cancer Biol. 2013 Dec;23(6 Pt B):522–32.

[42] Thiery JP, Acloque H, Huang RYJ, Nieto MA. Epithelial-mesenchymal transitions in development and disease. Cell. 2009 Nov 25;139(5):871–90.

[43] Mendez MG, Kojima S-I, Goldman RD. Vimentin induces changes in cell shape, motility, and adhesion during the epithelial to mesenchymal transition. FASEB J. 2010 Jun;24(6):1838–51.

[44] Sahai E. Mechanisms of cancer cell invasion. Curr Opin Genet Dev. 2005;15(1):87–96.

[45] Sun C, Zargham R, Shao Q, Gui X, Marcus V, Lazaris A, et al. Association of CD98, integrin β1, integrin β3 and Fak with the progression and liver metastases of colorectal cancer. Pathol Res Pract. 2014;1–7.

[46] Lai Y-H, Wu L-C, Li P-S, Wu W-H, Yang S-B, Xia P, et al. Tumour budding is a reproducible index for risk stratification of patients with Stage II colon cancer. Colorectal Dis. 2014 Apr;16(4):259–64.

[47] Mitrovic B, Schaeffer DF, Riddell RH, Kirsch R. Tumor budding in colorectal carcinoma: time to take notice. Mod Pathol. 2012;25(10):1315–25.

[48] Nabeshima K. Cohort migration of carcinoma cells: Differentiated colorectal carcinoma cells move as coherent cell clusters or sheets. Histology and Histopathology. 1999. p. 1183–97.

[49] Sood a K, Seftor E a, Fletcher MS, Gardner LM, Heidger PM, Buller RE, et al. Molecular determinants of ovarian cancer plasticity. Am J Pathol. 2001 Apr;158(4):1279–88.

[50] Chapnick D a, Liu X. Leader cell positioning drives wound-directed collective migration in TGFβ-stimulated epithelial sheets. Mol Biol Cell. 2014 May;25(10):1586–93.

[51] Polistena A, Cucina A, Dinicola S. MMP7 expression in colorectal tumours of different stages. In Vivo (Brooklyn). 2014;110:105–10.

[52] Wilson CL, Heppner KJ, Labosky PA, Hogan BL, Matrisian LM. Intestinal tumorigenesis is suppressed in mice lacking the metalloproteinase matrilysin. Proc Natl Acad Sci USA. 1997;94(4):1402–7.

[53] Wolf K, Mazo I, Leung H, Engelke K, Von Andrian UH, Deryugina EI, et al. Compensation mechanism in tumor cell migration: Mesenchymal-amoeboid

transition after blocking of pericellular proteolysis. J Cell Biol. 2003;160(2):267–77.

[54] Wyckoff JB, Jones JG, Condeelis JS, Segall JE. A critical step in metastasis: In vivo analysis of intravasation at the primary tumor. Cancer Res. 2000;60(9):2504–11.

[55] Friedl P, Borgmann S, Bröcker EB. Amoeboid leukocyte crawling through extracellular matrix: lessons from the Dictyostelium paradigm of cell movement. J Leukoc Biol. 2001;70(4):491–509.

[56] Vicker MG. F-actin assembly in Dictyostelium cell locomotion and shape oscillations propagates as a self-organized reaction-diffusion wave. FEBS Lett. 2002;510(1-2):5–9.

[57] Friedl P, Wolf K. Tumour-cell invasion and migration: diversity and escape mechanisms. Nat Rev Cancer. 2003;3(5):362–74.

[58] Carmeliet P, Jain RK. Molecular mechanisms and clinical applications of angiogenesis. Nature. 2011;473(7347):298–307.

[59] Drake CJ, Hungerford JE, Little CD. Morphogenesis of the first blood vessels. Ann N Y Acad Sci. 1998;857:155–79.

[60] Hanahan D. Signaling Vascular Morphogenesis and Maintenance. Science (80-). 1997;2:48–50.

[61] Carmeliet P, Ferreira V, Breier G, Pollefeyt S, Kieckens L, Gertsenstein M, et al. Abnormal blood vessel development and lethality in embryos lacking a single VEGF allele. Nature. 1996. p. 435–9.

[62] Fong GH, Rossant J, Gertsenstein M, Breitman ML. Role of the Flt-1 receptor tyrosine kinase in regulating the assembly of vascular endothelium. Nature. 1995. p. 66–70.

[63] Suri C, Jones PF, Patan S, Bartunkova S, Maisonpierre PC, Davis S, et al. Requisite role of angiopoietin-1, a ligand for the TIE2 receptor, during embryonic angiogenesis. Cell. 1996;87(7):1171–80.

[64] Bouvard D, Brakebusch C, Gustafsson E, Aszódi a, Bengtsson T, Berna a, et al. Functional consequences of integrin gene mutations in mice. Circ Res. 2001;89(3):211–23.

[65] Potente M, Gerhardt H, Carmeliet P. Basic and therapeutic aspects of angiogenesis. Cell. 2011;146(6):873–87.

[66] Carmeliet P. Mechanisms of angiogenesis and arteriogenesis. Nat Med. 2000;6(4):389–95.

[67] Phng LK, Gerhardt H. Angiogenesis: A Team Effort Coordinated by Notch. Dev Cell. 2009;16(2):196–208.

[68] Hellström M, Kalén M, Lindahl P, Abramsson A, Betsholtz C. Role of PDGF-B and PDGFR-beta in recruitment of vascular smooth muscle cells and pericytes during embryonic blood vessel formation in the mouse. Development. 1999;126:3047–55.

[69] Jain RK. Normalization of tumor vasculature: an emerging concept in antiangiogenic therapy. Science (80-). 2005;307(5706):58–62.

[70] Abdollahi A, Hahnfeldt P, Maercker C, Gröne H-J, Debus J, Ansorge W, et al. Endostatin's antiangiogenic signaling network. Mol Cell. 2004;13(5):649–63.

[71] Siemann DW. The unique characteristics of tumor vasculature and preclinical evidence for its selective disruption by Tumor-Vascular Disrupting Agents. Cancer Treat Rev. 2011;37(1):63–74.

[72] Morikawa S, Baluk P, Kaidoh T, Haskell A, Jain RK, McDonald DM. Abnormalities in pericytes on blood vessels and endothelial sprouts in tumors. Am J Pathol. 2002;160(3):985–1000.

[73] Hashizume H, Baluk P, Morikawa S, McLean JW, Thurston G, Roberge S, et al. Openings between defective endothelial cells explain tumor vessel leakiness. Am J Pathol. 2000;156(4):1363–80.

[74] Boucher Y, Baxter LT, Jain RK. Interstitial pressure gradients in tissue-isolated and subcutaneous tumours: implications for therapy. Cancer Res. 1990;50:4478–84.

[75] Fukumura D, Duda DG, Munn LL, Jain RK. Tumor microvasculature and microenvironment: novel insights through intravital imaging in pre-clinical models. Microcirculation. 2010;17(3):206–25.

[76] Helmlinger G, Yuan F, Dellian M, Jain RK. Interstitial pH and pO2 gradients in solid tumors in vivo: high-resolution measurements reveal a lack of correlation. Nat Med. 1997;3(2):177–82.

[77] Rohwer N, Cramer T. Hypoxia-mediated drug resistance: Novel insights on the functional interaction of HIFs and cell death pathways. Drug Resist Updat. 2011;14(3):191–201.

[78] Pires IM, Olcina MM, Anbalagan S, Pollard JR, Reaper PM, Charlton P a, et al. Targeting radiation-resistant hypoxic tumour cells through ATR inhibition. Br J Cancer. 2012;107(2):291–9.

[79] Lin C, McGough R, Aswad B, Block J a, Terek R. Hypoxia induces HIF-1α and VEGF expression in chondrosarcoma cells and chondrocytes. J Orthop Res. 2004;22:1175–81.

[80] Senger DR. Vascular endothelial growth factor: much more than an angiogenesis factor. Mol Biol Cell. 2010;21(3):377–9.

[81] Bouvet M, Ellis LM, Nishizaki M, Fujiwara T, Liu W, Bucana CD, et al. Adenovirus-mediated wild-type p53 gene transfer down-regulates vascular endothelial growth factor expression and inhibits angiogenesis in human colon cancer. Cancer Res. 1998;58(11):2288–92.

[82] Pal S, Datta K, Mukhopadhyay D. Central role of p53 on regulation of vascular permeability factor/vascular endothelial growth factor (VPF/VEGF) expression in mammary carcinoma. Cancer Res. 2001;61(18):6952–7.

[83] Dias S, Hattori K, Zhu Z, Heissig B, Choy M, Lane W, et al. Autocrine stimulation of VEGFR-2 activates human leukemic cell growth and migration. J Clin Invest. 2000;106(4):511–21.

[84] Fan F, Wey JS, McCarty MF, Belcheva A, Liu W, Bauer TW, et al. Expression and function of vascular endothelial growth factor receptor-1 on human colorectal cancer cells. Oncogene. 2005;24(16):2647–53.

[85] Hicklin DJ, Ellis LM. Role of the Vascular Endothelial Growth Factor Pathway in Tumor Growth and Angiogenesis. J Clin Oncol. 2005;23(5):1011–27.

[86] Peck Y, Wang D. Three-dimensionally engineered biomimetic tissue models for in vitro drug evaluation: delivery, efficacy and toxicity. Expert Opin Drug Deliv. 2013;10(3):369–83.

[87] Xu X, Sabanayagam CR, Harrington D a., Farach-Carson MC, Jia X. A hydrogel-based tumor model for the evaluation of nanoparticle-based cancer therapeutics. Biomaterials. 2014;35(10):3319–30.

[88] Yang Z, Zhao X. A 3D model of ovarian cancer cell lines on peptide nanofiber scaffold to explore the cell-scaffold interaction and chemotherapeutic resistance of anticancer drugs. Int J Nanomedicine. 2011 Jan;6:303–10.

[89] Zschenker O, Streichert T, Hehlgans S, Cordes N. Genome-wide gene expression analysis in cancer cells reveals 3D growth to affect ECM and processes associated with cell adhesion but not DNA repair. PLoS One. 2012 Jan;7(4):e34279.

[90] Cho A, Howell VM, Colvin EK. The Extracellular Matrix in Epithelial Ovarian Cancer – A Piece of a Puzzle. Front Oncol. 2015;5(November):245.

[91] Pirilä E, Sharabi A, Salo T, Quaranta V, Tu H, Heljasvaara R, et al. Matrix metalloproteinases process the laminin-5 γ 2-chain and regulate epithelial cell migration. Biochem Biophys Res Commun. 2003;303:1012–7.

[92] Fidler IJ. Tumor Heterogeneity and the Biology of Cancer Invasion and Metastasis. Cancer Res. 1978;38:2651–60.

[93] Minchinton AI, Tannock IF. Drug penetration in solid tumours. Nat Rev Cancer. 2006 Aug;6(8):583–92.

[94] Cukierman E, Pankov R, Stevens DR, Yamada KM. Taking cell-matrix adhesions to the third dimension. Science. 2001 Nov 23;294(5547):1708–12.

[95] Hutmacher DW. Biomaterials offer cancer research the third dimension. Nat Mater. 2010;9(2):90–3.

[96] Mseka T, Bamburg JR, Cramer LP. ADF/cofilin family proteins control formation of oriented actin-filament bundles in the cell body to trigger fibroblast polarization. J Cell Sci. 2007;120(Pt 24):4332–44.

[97] Weaver VM, Lelievre S, Lakins JN, Chrenek MA, Jones JCR, Giancotti F, et al. β4 integrin-dependent formation of polarized three-dimensional architecture confers resistance to apoptosis in normal and malignant mammary epithelium. Cancer Cell. 2002;2(3):205–16.

[98] Adams RH, Alitalo K. Molecular regulation of angiogenesis and lymphangiogenesis. Nat Rev Mol Cell Biol. 2007;8(6):464–78.

[99] Hirschhaeuser F, Menne H, Dittfeld C, West J, Mueller-Klieser W, Kunz-Schughart L a. Multicellular tumor spheroids: an underestimated tool is catching up again. J Biotechnol. 2010 Jul 1;148(1):3–15.

[100] Friedrich J, Ebner R, Kunz-Schughart L a. Experimental anti-tumor therapy in 3-D: spheroids--old hat or new challenge? Int J Radiat Biol. 2007;83(11-12):849–71.

[101] Pickl M, Ries CH. Comparison of 3D and 2D tumor models reveals enhanced HER2 activation in 3D associated with an increased response to trastuzumab. Oncogene. 2009 Jan 22;28(3):461–8.

[102] Phung YT. Rapid Generation of In Vitro Multicellular Spheroids for the Study of Monoclonal Antibody Therapy. J Cancer. 2011;2(1):507.

[103] Vinci M, Gowan S, Boxall F, Patterson L, Zimmermann M, Court W, et al. Advances in establishment and analysis of three-dimensional tumor spheroid-based functional assays for target validation and drug evaluation. BMC Biol. 2012 Jan;10(1):29.

[104] Stadler M, Walter S, Walzl A, Kramer N, Unger C, Scherzer M, et al. Increased complexity in carcinomas: Analyzing and modeling the interaction of human cancer cells with their microenvironment. Semin Cancer Biol. 2015;35:107–24.

[105] Santini MT, Rainaldi G, Indovina PL. Multicellular tumour spheroids in radiation biology. Int J Radiat Biol. 1999;75(7):787–99.

[106] Tung Y-C, Hsiao AY, Allen SG, Torisawa Y, Ho M, Takayama S. High-throughput 3D spheroid culture and drug testing using a 384 hanging drop array. Analyst. 2011 Feb 7;136(3):473–8.

[107] Woods ML, Koch CJ, Lord EM. Detection of individual hypoxic cells in multicellular spheroids by flow cytometry using the 2-nitroimidazole, EF5, and monoclonal antibodies. Int J Radiat Oncol Biol Phys. 1996;34(1):93–101.

[108] Alekseeva, T., Unger, R.E., Brochhausen, C., Brown, R.D., Kirkpatrick JC. Engineering a micro-vascular capillary bed in a tissue-like collagen construct. Tissue Eng Part A. 2013;20:1–36.

[109] Longati P, Jia X, Eimer J, Wagman A, Witt M-R, Rehnmark S, et al. 3D pancreatic carcinoma spheroids induce a matrix-rich, chemoresistant phenotype offering a better model for drug testing. BMC Cancer.

2013;13(1):95.

[110] Xiang X, Phung Y, Feng M, Nagashima K, Zhang J, Broaddus VC, et al. The development and characterization of a human mesothelioma in vitro 3D model to investigate immunotoxin therapy. PLoS One. 2011 Jan;6(1):e14640.

[111] De Witt Hamer PC, Jonker A, Leenstra S, Ruijter JM, Van Noorden CJF. Quantification of viability in organotypic multicellular spheroids of human malignant glioma using lactate dehydrogenase activity: a rapid and reliable automated assay. J Histochem Cytochem. 2005 Jan;53(1):23–34.

[112] Friedrich J, Eder W, Castaneda J, Doss M, Huber E, Ebner R, et al. A reliable tool to determine cell viability in complex 3-d culture: the acid phosphatase assay. J Biomol Screen. 2007 Oct;12(7):925–37.

[113] Suri S, Schmidt CE. Cell-laden hydrogel constructs of hyaluronic acid, collagen, and laminin for neural tissue engineering. Tissue Eng Part A. 2010 May;16(5):1703–16.

[114] Doillon CJ, Gagnon E, Paradis R, Koutsilieris M. Three-dimensional culture system as a model for studying cancer cell invasion capacity and anticancer drug sensitivity. Anticancer Res. 2004;24(4):2169–77.

[115] Brien FJO. Biomaterials and scaffolds for tissue engineering. Mater Today. 2011;14(3).

[116] Dalgleish R. The human type I collagen mutation database. Nucleic Acids Res. 1997;25(1):181–7.

[117] Stamati K, Priestley J V, Mudera V, Cheema U. Laminin promotes vascular network formation in 3D in vitro collagen scaffolds by regulating VEGF uptake. Exp Cell Res. 2014 Sep 10;327(1):68–77.

[118] Holliday DL, Brouilette KT, Markert A, Gordon L a, Jones JL. Novel multicellular organotypic models of normal and malignant breast: tools for

dissecting the role of the microenvironment in breast cancer progression. Breast Cancer Res. 2009 Jan;11(1):R3.

[119] Chow CR, Ebine K, Knab LM, Bentrem DJ, Kumar K, Munshi HG. Cancer Cell Invasion in 3D collagen is Differentially Regulated by Gα13 and Discoidin Domain Receptor 1-Par3 Signaling. J Biol Chem. 2015;jbc.M115.669606.

[120] Brown R a, Wiseman M, Chuo C-B, Cheema U, Nazhat SN. Ultrarapid engineering of biomimetic materials and tissues: Fabrication of nano- and microstructures by plastic compression. Adv Funct Mater. 2005 Nov;15(11):1762–70.

[121] Addad S, Exposito JY, Faye C, Ricard-Blum S, Lethias C. Isolation, characterization and biological evaluation of jellyfish collagen for use in biomedical applications. Mar Drugs. 2011;9(6):967–83.

[122] Lokeshwar VB, Mirza S, Jordan A. Targeting Hyaluronic Acid Family for Cancer Chemoprevention and Therapy. 1st ed. Hyaluronan signaling and turnover. 2014. 35-65 p.

[123] Toole BP. Hyaluronan: from extracellular glue to pericellular cue. Nat Rev Cancer. 2004;4(7):528–39.

[124] Florczyk SJ, Wang K, Jana S, Wood DL, Sytsma SK, Sham JG, et al. Porous chitosan-hyaluronic acid scaffolds as a mimic of glioblastoma microenvironment ECM. Biomaterials. 2013;34(38):10143–50.

[125] Li G, Simon MJ, Cancel LM, Shi Z-D, Ji X, M. JT, et al. Permeability of Endothelial and Astrocyte Cocultures: In Vitro Blood–Brain Barrier Models for Drug Delivery Studies. Biotechnol Adv. 2011;29(6):997–1003.

[126] Fischbach C, Chen R, Matsumoto T, Schmelzle T, Brugge JS, Polverini PJ, et al. Engineering tumors with 3D scaffolds. Nat Methods. 2007 Oct;4(10):855–60.

[127] Hughes CS, Postovit LM, Lajoie GA. Matrigel: A complex protein mixture required for optimal growth of cell culture. Proteomics. 2010;10(9):1886–90.

[128] Staton CA, Reed MWR, Brown NJ. A critical analysis of current in vitro and in vivo angiogenesis assays. Int J Exp Pathol. 2009;90(3):195–221.

[129] Arnaoutova I, Kleinman HK. In vitro angiogenesis: endothelial cell tube formation on gelled basement membrane extract. Nat Protoc. 2010;5(4):628–35.

[130] Sung KE, Su X, Berthier E, Pehlke C, Friedl A, Beebe DJ. Understanding the Impact of 2D and 3D Fibroblast Cultures on In Vitro Breast Cancer Models. PLoS One. 2013;8(10):1–13.

[131] Shekhar MP V, Werdell J, Santner SJ, Pauley RJ, Tait L. Breast Stroma Plays a Dominant Regulatory Role in Breast Epithelial Growth and Differentiation : Implications for Tumor Development and Progression. Cancer Res. 2001;(61):1320–6.

[132] Fu Y, Xu K, Zheng X, Giacomin AJ, Mix AW, Kao WJ. 3D cell entrapment in crosslinked thiolated gelatin-poly(ethylene glycol) diacrylate hydrogels. Biomaterials. 2012;33(1):48–58.

[133] Greiner AM, Richter B, Bastmeyer M. Micro-engineered 3D scaffolds for cell culture studies. Macromol Biosci. 2012;12(10):1301–14.

[134] Fong ELS, Lamhamedi-Cherradi S-E, Burdett E, Ramamoorthy V, Lazar AJ, Kasper FK, et al. Modeling Ewing sarcoma tumors in vitro with 3D scaffolds. Proc Natl Acad Sci U S A. 2013;110(16):6500–5.

[135] Cunliffe D, Pennadam S, Alexander C. Synthetic and biological polymers—merging the interface. Eur Polym J. 2004;40(1):5–25.

[136] Frantz C, Stewart KM, Weaver VM. The extracellular matrix at a glance. J Cell Sci. 2010;123:4195–200.

[137] Loessner D, Stok KS, Lutolf MP, Hutmacher DW, Clements J a., Rizzi SC. Bioengineered 3D platform to explore cell-ECM interactions and drug resistance of epithelial ovarian cancer cells. Biomaterials. 2010;31(32):8494–506.

[138] Soman P, Kelber J a., Lee JW, Wright TN, Vecchio KS, Klemke RL, et al. Cancer cell migration within 3D layer-by-layer microfabricated photocrosslinked PEG scaffolds with tunable stiffness. Biomaterials. 2012;33(29):7064–70.

[139] Guzman A, Ziperstein MJ, Kaufman LJ. The effect of fibrillar matrix architecture on tumor cell invasion of physically challenging environments. Biomaterials. 2014 Aug;35(25):6954–63.

[140] Horning JL, Sahoo SK, Vijayaraghavalu S, Dimitrijevic S, Vasir JK, Jain TK, et al. 3-D tumor model for in vitro evaluation of anticancer drugs. Mol Pharm. 2008;5(5):849–62.

[141] Nicosia RF, Bonanno E, Smith M, Yurchenco P. Modulation of angiogenesis in vitro by laminin-entactin complex. Developmental biology. 1994. p. 197–206.

[142] Stamati K. In vitro vasculogenesis in 3D. PhD Thesis. 2014;

[143] Ricketts KPM, Cheema U, Nyga A, Castoldi A, Guazzoni C, Magdeldin T, et al. A 3D In Vitro Cancer Model as a Platform for Nanoparticle Uptake and Imaging Investigations. Small. 2014 Jul 2;(19):3954–61.

[144] Magdeldin T, López-Dávila V, Villemant C, Cameron G, Drake R, Cheema U, et al. The efficacy of cetuximab in a tissue-engineered three-dimensional in vitro model of colorectal cancer. J Tissue Eng. 2014 Jul 23;5:1–9.

[145] Nyga A, Loizidou M, Emberton M, Cheema U. A novel tissue engineered three-dimensional in vitro colorectal cancer model. Acta Biomater. 2013 Aug;9(8):7917–26.

[146] Chowdhury S, Ongchin M, Sharratt E, Dominguez I, Wang J, Brattain MG, et al. Intra-tumoral heterogeneity in metastatic potential and survival signaling between iso-clonal HCT116 and HCT116b human colon carcinoma cell lines. PLoS One. 2013 Jan;8(4):e60299.

[147] Mori M, Barnard GF, Mimori K, Ueo H, Akiyoshi T, Sugimachi K. Overexpression of matrix metalloproteinase-7 mRNA in human colon carcinomas. Cancer. 1995;75(6):1516–9.

[148] McDonnell S, Navre M, Coffey RJ, Matrisian LM. Expression and localization of the matrix metalloproteinase pump-1 (MMP-7) in human gastric and colon carcinomas. Mol Carcinog. 1991;4(6):527–33.

[149] Wilson CL, Matrisian LM. Matrilysin: An epithelial matrix metalloproteinase with potentially novel functions. Int J Biochem Cell Biol. 1996;28(2):123–36.

[150] Remy L, Trespeuch C, Bachy S, Scoazec JY, Rousselle P. Matrilysin 1 influences colon carcinoma cell migration by cleavage of the laminin-5 β3 chain. Cancer Res. 2006;66(23):11228–37.

[151] Tan NS, Alekseeva T, Brown RA. Roofed grooves: Rapid layer engineering of perfusion channels in collagen tissue models. J Biomater Appl. 2014;29(4):605–16.

[152] Sapudom J, Rubner S, Martin S, Kurth T, Riedel S, Mierke CT, et al. The phenotype of cancer cell invasion controlled by fibril diameter and pore size of 3D collagen networks. Biomaterials. 2015;52:367–75.

[153] Guo C, Kaufman LJ. Flow and magnetic field induced collagen alignment. Biomaterials. 2007;28(6):1105–14.

[154] Georgiou M, Bunting SCJ, Davies H a, Loughlin AJ, Golding JP, Phillips JB. Engineered neural tissue for peripheral nerve repair. Biomaterials. 2013 Oct;34(30):7335–43.

[155] Knight DP, Nash L, Hu XW, Haffegee J, Ho MW. In vitro formation by reverse dialysis of collagen gels containing highly oriented arrays of fibrils. J Biomed Mater Res. 1998;41(2):185–91.

[156] Burdett E, Kasper FK, Mikos AG, Ludwig J a. Engineering tumors: a tissue engineering perspective in cancer biology. Tissue Eng Part B Rev. 2010;16(3):351–9.

[157] Laurent J, Frongia C, Cazales M, Mondesert O, Ducommun B, Lobjois V. Multicellular tumor spheroid models to explore cell cycle checkpoints in 3D. BMC Cancer. 2013;13(1):73.

[158] Zlobec I, Hädrich M, Dawson H, Koelzer VH, Borner M, Mallaev M, et al. Intratumoural budding (ITB) in preoperative biopsies predicts the presence of lymph node and distant metastases in colon and rectal cancer patients. Br J Cancer. 2014 Feb 18;110(4):1008–13.

[159] Fleming M, Ravula S, Tatishchev SF, Wang HL. Colorectal carcinoma: Pathologic aspects. J Gastrointest Oncol. 2012 Sep;3(3):153–73.

[160] Kitamura T, Kometani K, Hashida H, Matsunaga A, Miyoshi H, Hosogi H, et al. SMAD4-deficient intestinal tumors recruit CCR1+ myeloid cells that promote invasion. Nat Genet. 2007;39(4):467–75.

[161] Haage A, Schneider IC. Cellular contractility and extracellular matrix stiffness regulate matrix metalloproteinase activity in pancreatic cancer cells. FASEB J. 2014 Aug;28(8):3589–99.

[162] Bayless KJ, Kwak H-I, Su S-C. Investigating endothelial invasion and sprouting behavior in three-dimensional collagen matrices. Nat Protoc. 2009;4(12):1888–98.

[163] Gonzalez AM, Gonzales M, Herron GS, Nagavarapu U, Hopkinson SB, Tsuruta D, et al. Complex interactions between the laminin alpha 4 subunit and integrins regulate endothelial cell behavior in vitro and angiogenesis in

vivo. Proc Natl Acad Sci U S A. 2002;99(25):16075–80.

[164] Pyke C, Salo S, Ralfkiaer E, Romer J, Dano K, Tryggvason K. Laminin-5 is a marker of invading cancer cells in some human carcinomas and is coexpressed with the receptor for urokinase plasminogen activator in budding cancer cells in colon adenocarcinomas. Cancer Res. 1995;55:4132–9.

[165] Hamasaki H, Koga K, Aoki M, Hamasaki M, Koshikawa N, Seiki M, et al. Expression of laminin 5-γ2 chain in cutaneous squamous cell carcinoma and its role in tumour invasion. Br J Cancer. 2011;105(6):824–32.

[166] Hlubek F, Jung a., Kotzor N, Kirchner T, Brabletz T. Expression of the invasion factor laminin γ2 in colorectal carcinomas is regulated by β-catenin. Cancer Res. 2001;61:8089–93.

[167] Sordat I, Rousselle P, Chaubert P, Petermann O, Aberdam D, Bosman FT, et al. Tumor cell budding and laminin-5 expression in colorectal carcinoma can be modulated by the tissue micro-environment. Int J Cancer. 2000;88(5):708–17.

[168] Deryugina EI, Bourdon M a, Reisfeld R a, Strongin a. Remodeling of collagen matrix by human tumor cells requires activation and cell surface association of matrix metalloproteinase-2. Cancer Res. 1998;58:3743–50.

[169] Li J, Liu J, Li P, Mao X, Li W, Yang J, et al. Loss of LKB1 disrupts breast epithelial cell polarity and promotes breast cancer metastasis and invasion. J Exp Clin Cancer Res. 2014;33:70.

[170] Cheung KJ, Gabrielson E, Werb Z, Ewald AJ. Collective invasion in breast cancer requires a conserved basal epithelial program. Cell. 2013;155(7):1639–51.

[171] Friedl P, Alexander S. Cancer invasion and the microenvironment: plasticity and reciprocity. Cell. 2011 Nov 23;147(5):992–1009.

[172] Nabha SM, dos Santos EB, Yamamoto HA, Belizi A, Dong Z, Meng H, et al. Bone marrow stromal cells enhance prostate cancer cell invasion through type I collagen in an MMP-12 dependent manner. Int J Cancer. 2008 Jun 1;122(11):2482–90.

[173] Olsen CJ, Moreira J, Lukanidin EM, Ambartsumian NS. Human mammary fibroblasts stimulate invasion of breast cancer cells in a three-dimensional culture and increase stroma development in mouse xenografts. BMC Cancer. 2010;10:444.

[174] Madar S, Goldstein I, Rotter V. "Cancer associated fibroblasts" - more than meets the eye. Trends Mol Med. 2013 Aug;19(8):447–53.

[175] Ivanovic Z. Hypoxia or in situ normoxia: The stem cell paradigm. J Cell Physiol. 2009;219(2):271–5.

[176] Moll R, Schiller DL, Franke WW. Identification of protein IT of the intestinal cytoskeleton as a novel type I cytokeratin with unusual properties and expression patterns. J Cell Biol. 1990;111(2):567–80.

[177] Grant DS, Kleinman HK, Martin GR. The role of basement membranes in vascular development. Ann N Y Acad Sci. 1990;588:61–72.

[178] Dudley AC. Tumor endothelial cells. Cold Spring Harb Perspect Med. 2012;2(3):1–18.

[179] Truskey GA. Endotheliar cell vascular smooth muscle co-culture assay for high throughput screening assays. Int J high throughput screen. 2011;2010(1):171–81.

[180] Saleh F a, Whyte M, Genever PG. Effects of endothelial cells on human mesenchymal stem cell activity in a three-dimensional in vitro model. Eur Cell Mater. 2011;22:242–57.

[181] Kalluri R, Zeisberg M. Fibroblasts in cancer. Nat Rev Cancer. 2006;6(5):392–

401.

[182] Kirkpatrick CJ, Fuchs S, Unger RE. Co-culture systems for vascularization — Learning from nature. Adv Drug Deliv Rev. 2011;63(4-5):291–9.

[183] Rao RR, Peterson AW, Ceccarelli J, Putnam AJ, Stegemann JP. Matrix composition regulates three-dimensional network formation by endothelial cells and mesenchymal stem cells in collagen/fibrin materials. Angiogenesis. 2012;15(2):253–64.

[184] Velazquez OC, Snyder R, Liu ZJ, Fairman RM, Herlyn M. Fibroblast-dependent differentiation of human microvascular endothelial cells into capillary-like, three-dimensional networks. FASEB J. 2002;16:1316–8.

[185] Rhee S. Fibroblasts in three dimensional matrices: cell migration and matrix remodeling. Exp Mol Med. 2009;41(12):858.

[186] Turner N, Grose R. Fibroblast growth factor signalling: from development to cancer. Nat Rev Cancer. 2010;10(2):116–29.

[187] Rajski M, Zanetti-Dällenbach R, Vogel B, Herrmann R, Rochlitz C, Buess M. IGF-I induced genes in stromal fibroblasts predict the clinical outcome of breast and lung cancer patients. BMC Med. 2010;8:1.

[188] Knuchel S, Anderle P, Werfelli P, Diamantis E, Rüegg C. Fibroblast surface-associated FGF-2 promotes contact-dependent colorectal cancer cell migration and invasion through FGFR-SRC signaling and integrin αvβ5-mediated adhesion. Oncotarget. 2015;6(16):14300–17.

[189] Yurchenco PD. Basement membranes: Cell scaffoldings and signaling platforms. Cold Spring Harb Perspect Biol. 2011;3(2):1–27.

[190] Azzi S, Hebda JK, Gavard J. Vascular permeability and drug delivery in cancers. Front Oncol. 2013;3(August):211.

[191] Buckanovich RJ, Sasaroli D, O'Brien-Jenkins A, Botbyl J, Hammond R, Katsaros D, et al. Tumor Vascular Proteins As Biomarkers in Ovarian Cancer. J Clin Oncol. 2007;25(7):852–61.

[192] Pepin F, Bertos N, Laferrière J, Sadekova S, Souleimanova M, Zhao H, et al. Gene-expression profiling of microdissected breast cancer microvasculature identifies distinct tumor vascular subtypes. Breast Cancer Res. 2012;14(4):R120.

[193] Lubarsky B, Krasnow M a. Tube morphogenesis: Making and shaping biological tubes. Cell. 2003;112(1):19–28.

[194] Iruela-Arispe ML, Davis GE. Cellular and Molecular Mechanisms of Vascular Lumen Formation. Dev Cell. 2009;16(2):222–31.

[195] Davis GE, Kon W, Stratman AN. Mechanisms controlling human endothelial lumen formation and tube assembly in three-dimensional extracellular matrices. Birth Defects Res Part C - Embryo Today Rev. 2007;81(4):270–85.

[196] Nilsson I, Shibuya M, Wennström S. Differential activation of vascular genes by hypoxia in primary endothelial cells. Exp Cell Res. 2004;299(2):476–85.

[197] Namiki A, Brogi E, Kearney M, Kim EA, Wu T, Couffinhal T, et al. Hypoxia induces vascular endothelial growth factor in cultured human endothelial cells. J Biol Chem. 1995;271(52):31189–95.

[198] Lu P, Weaver VM, Werb Z. The extracellular matrix: A dynamic niche in cancer progression. J Cell Biol. 2012;196(4):395–406.

[199] Thoma CR, Zimmermann M, Agarkova I, Kelm JM, Krek W. 3D cell culture systems modeling tumor growth determinants in cancer target discovery. Adv Drug Deliv Rev. 2014;69-70:29–41.

[200] Cerna M, Holubec L, Pesta M, Kormunda S, Topolcan O, Cerny R. Quantitative estimation of CEA and CK20 expression in tumour tissue of

colorectal cancer and its liver metastases with reverse transcription and real-time PCR. Anticancer Res. 2006;26(1B):803–8.

[201] Kim JH, Rhee Y, Bae JM, Cho N, Kang GH. Loss of CDX2/CK20 expression is associated with poorly differentiated carcinoma, the CpG island methylator phenotype, and adverse prognosis in microsatellite-unstable colorectal cancer. Am J Surg Pathol. 2013;37(10):1532–41.

[202] Werling RW, Yaziji H, Bacchi CE, Gown AM. CDX2, a highly sensitive and specific marker of adenocarcinomas of intestinal origin: an immunohistochemical survey of 476 primary and metastatic carcinomas. Am J Surg Pathol. 2003;27(3):303–10.

[203] Lugli A, Tzankov A, Zlobec I, Terracciano LM. Differential diagnostic and functional role of the multi-marker phenotype CDX2/CK20/CK7 in colorectal cancer stratified by mismatch repair status. Mod Pathol. 2008;21(11):1403–12.

[204] Park SY, Kim HS, Hong EK, Kim WH. Expression of cytokeratins 7 and 20 in primary carcinomas of the stomach and colorectum and their value in the differential diagnosis of metastatic carcinomas to the ovary. Hum Pathol. 2002;33(11):1078–85.

[205] Luca AC, Mersch S, Deenen R, Schmidt S, Messner I, Schäfer K-L, et al. Impact of the 3D microenvironment on phenotype, gene expression, and EGFR inhibition of colorectal cancer cell lines. PLoS One. 2013;8(3):e59689.

[206] Windus LCE, Kiss DL, Glover T, Avery VM. In vivo biomarker expression patterns are preserved in 3D cultures of Prostate Cancer. Exp Cell Res. 2012;318(19):2507–19.

[207] Dunn EF, Iida M, Myers R a, Campbell D a, Hintz K a, Armstrong E a, et al. Dasatinib sensitizes KRAS mutant colorectal tumors to cetuximab. Oncogene. 2011 Feb 3;30(5):561–74.

[208] Amado RG, Wolf M, Peeters M, Van Cutsem E, Siena S, Freeman DJ, et al. Wild-type KRAS is required for panitumumab efficacy in patients with metastatic colorectal cancer. J Clin Oncol. 2008 Apr 1;26(10):1626–34.

[209] Fourest-Lieuvin A, Peris L, Gache V, Garcia-Saez I, Juillan-Binard C, Lantez V, et al. Microtubule regulation in mitosis: tubulin phosphorylation by the cyclin-dependent kinase Cdk1. Mol Biol Cell. 2006;17(3):1041–50.

[210] Hu M, Zhao M, An C, Yang M, Li Q, Zhang Y, et al. Real-time imaging of apoptosis induction of human breast cancer cells by the traditional Chinese medicinal herb tubeimu. Anticancer Res. 2012;32(7):2509–14.

[211] Kenny P a, Lee GY, Myers C a, Neve RM, Semeiks JR, Spellman PT, et al. The morphologies of breast cancer cell lines in three-dimensional assays correlate with their profiles of gene expression. Mol Oncol. 2007 Jun;1(1):84–96.

[212] Yamaguchi H, Condeelis J. Regulation of the actin cytoskeleton in cancer cell migration and invasion. Biochim Biophys Acta. 2007 May;1773(5):642–52.

[213] Patsialou A, Wyckoff J, Wang Y. Invasion of human breast cancer cells in vivo requires both paracrine and autocrine loops involving the colony-stimulating factor-1 receptor. Cancer Res. 2009;69(24):9498–506.

[214] Franovic A, Gunaratnam L, Smith K, Robert I, Patten D, Lee S. Translational up-regulation of the EGFR by tumor hypoxia provides a nonmutational explanation for its overexpression in human cancer. Proc Natl Acad Sci U S A. 2007;104(32):13092–7.

[215] Wild R, Fager K, Flefleh C, Kan D, Inigo I, Castaneda S, et al. Cetuximab preclinical antitumor activity (monotherapy and combination based) is not predicted by relative total or activated epidermal growth factor receptor tumor expression levels. Mol Cancer Ther. 2006 Jan;5(1):104–13.

[216] Hsu Y-F, Ajona D, Corrales L, Lopez-Picazo JM, Gurpide A, Montuenga LM,

et al. Complement activation mediates cetuximab inhibition of non-small cell lung cancer tumor growth in vivo. Mol Cancer. 2010;9(1):139.

[217] Baselga J. The EGFR as a target for anticancer therapy-focus on cetuximab. Eur J Cancer. 2001;37:S16–22.

[218] Baselga BJ, Pfister D, Cooper MR, Cohen R, Burtness B, Bos M, et al. Phase I Studies of Anti – Epidermal Growth Factor Receptor Chimeric Antibody C225 Alone and in Combination With Cisplatin. J Clin Oncol. 2000;18(4):904–14.

[219] López-Dávila V, Seifalian AM, Loizidou M. Organic nanocarriers for cancer drug delivery. Curr Opin Pharmacol. 2012 Aug;12(4):414–9.

[220] Hatzivassiliou G, Song K, Yen I, Brandhuber BJ, Anderson DJ, Alvarado R, et al. RAF inhibitors prime wild-type RAF to activate the MAPK pathway and enhance growth. Nature. 2010;464(7287):431–5.

[221] Laurent-Puig P, Cayre A, Manceau G, Buc E, Bachet J-B, Lecomte T, et al. Analysis of PTEN, BRAF, and EGFR status in determining benefit from cetuximab therapy in wild-type KRAS metastatic colon cancer. J Clin Oncol. 2009 Dec 10;27(35):5924–30.

[222] Xu H, Yu Y, Marciniak D, Rishi AK, Sarkar FH, Kucuk O, et al. Epidermal growth factor receptor (EGFR)-related protein inhibits multiple members of the EGFR family in colon and breast cancer cells. Mol Cancer Ther. 2005;4:435–42.

[223] Du L, Wang H, He L, Zhang J, Ni B, Wang X, et al. CD44 is of Functional Importance for Colorectal Cancer Stem Cells. Clin Cancer Res. 2008;14(21):6751–60.

[224] Cho SH, Park YS, Kim HJ, Kim CH, Lim SW, Huh JW, et al. CD44 enhances the epithelial-mesenchymal transition in association with colon cancer invasion. Int J Oncol. 2012 Jul;41(1):211–8.

[225] La Fleur L, Johansson A-C, Roberg K. A CD44high/EGFRlow subpopulation within head and neck cancer cell lines shows an epithelial-mesenchymal transition phenotype and resistance to treatment. PLoS One. 2012;7(9):e44071.

Appendix

Original Article

The efficacy of cetuximab in a tissue-engineered three-dimensional in vitro model of colorectal cancer

Journal of Tissue Engineering
Volume 5: 1–9

DOI: 10.1177/2041731414544183
tej.sagepub.com
SAGE

Tarig Magdeldin[1,2], Víctor López-Dávila[1], Cecile Villemant[3], Grant Cameron[3], Rosemary Drake[3], Umber Cheema[2] and Marilena Loizidou[1]

Abstract

The preclinical development process of chemotherapeutic drugs is often carried out in two-dimensional monolayer cultures. However, a considerable amount of evidence demonstrates that two-dimensional cell culture does not accurately reflect the three-dimensional in vivo tumour microenvironment, specifically with regard to gene expression profiles, oxygen and nutrient gradients and pharmacokinetics. With this objective in mind, we have developed and established a physiologically relevant three-dimensional in vitro model of colorectal cancer based on the removal of interstitial fluid from collagen type I hydrogels. We employed the RAFT™ (Real Architecture For 3D Tissue) system for producing three-dimensional cultures to create a controlled reproducible, multiwell testing platform. Using the HT29 and HCT116 cell lines to model epidermal growth factor receptor expressing colorectal cancers, we characterized three-dimensional cell growth and morphology in addition to the anti-proliferative effects of the anti–epidermal growth factor receptor chemotherapeutic agent cetuximab in comparison to two-dimensional monolayer cultures. Cells proliferated well for 14 days in three-dimensional culture and formed well-defined cellular aggregates within the concentrated collagen matrix. Epidermal growth factor receptor expression levels revealed a twofold and threefold increase in three-dimensional cultures for both HT29 and HCT116 cells in comparison to two-dimensional monolayers, respectively ($p < 0.05$; $p < 0.01$). Cetuximab efficacy was significantly lower in HT29 three-dimensional cultures in comparison to two-dimensional monolayers, whereas HCT116 cells in both two-dimension and three-dimension were non-responsive to treatment in agreement with their *KRAS* mutant status. In summary, these results confirm the use of a three-dimensional in vitro cancer model as a suitable drug-screening platform for in vitro pharmacological testing.

Keywords

Collagen, plastic compression, three-dimensional culture, cetuximab, drug discovery, colorectal cancer, epidermal growth factor receptor

Received: 18 April 2014; accepted: 20 June 2014

Introduction

Cancer is one of the leading causes of death worldwide with an estimated 12.6 million people diagnosed in 2008, accounting for approximately 7.6 million deaths globally.[1] Cancer prognosis would improve with better therapeutic regimens, particularly when tumours cannot be managed by surgical resection alone and require subsequent chemo- or radiotherapy. The majority of current models for therapeutic and pharmacological investigations are carried out in either two-dimensional (2D) reductionist in vitro cell culture or severe combined

[1]Cancer Nanotechnology Group, UCL Division of Surgery and Interventional Science, London, UK
[2]Tissue Repair and Engineering Centre, Institute of Orthopaedics and Musculoskeletal Sciences, UCL Division of Surgery and Interventional Science, Stanmore, UK
[3]TAP Biosystems, Royston, UK

Corresponding author:
Marilena Loizidou, Cancer Nanotechnology Group, UCL Division of Surgery and Interventional Science, Royal Free Campus, London, NW3 2QG, UK.
Email: m.loizidou@ucl.ac.uk

immunodeficient (SCID) animal models. It is, however, becoming increasingly apparent that microenvironmental factors play an important role in controlling both the progression of cancer and the chemotherapeutic response to treatment.[2] Although highly useful, 2D in vitro cell models lack the sophistication of cellular orientation and cell–matrix interactions, while animal models often overlook host factors that are typically involved in disease progression such as the immune system.[3] Both types of investigations are routinely used by pharmaceutical companies, but efficiency of drug discovery and clinical translation remain suboptimal. For example, this holds true for the family of Endothelin A receptor antagonists, for example, atrasentan. Despite encouraging preclinical data, the agents failed to demonstrate a benefit in clinical trials and therefore have not progressed to the clinic.[4] To address the gap between 2D culture systems and in vivo models, three-dimensional (3D) cell culture systems such as multicellular tumour spheroids and scaffold-based approaches have been used as a bridge to further our understanding of cancer biology, particularly how the cells may respond to treatment in a 3D environment. Of the available 3D in vitro models, spheroid assays are widely used for therapeutic testing;[5] however, they are inherently limited by their size (400–600 μm) resulting from nutrient and O_2 deficiency. Spheroids develop a necrotic core surrounded by a rim of viable cells (100–300 μm) in the periphery.[6] Due to the absence of a matrix, cancer cells have restricted mobility, a key parameter in the development of micrometastases in vivo. More recent approaches have utilized natural or synthetic scaffolds. Natural scaffolds include extracellular matrix (ECM) proteins such as collagen, laminin or hyaluronic acid.[7,8] They are largely malleable by cell behaviour, typically as a result of ECM degrading proteins such as matrix-metalloproteinases (MMPs). This is remarkably helpful for modelling the complex dynamic nature of tumours. Natural scaffolds are also appealing due to their biocompatibility and orientation that allows cell surface receptors such as integrins and discoidin domain receptors to interact with natural matrix proteins. Hyperhydrated gel systems such as collagen consist of cross-linked macromolecular networks of hydrophilic polymers.[9] However, this hyperhydration (~99% water) is not physiologically representative of any tissue in the in vivo environment, and ultimately, more biomimetic models are needed to model tumours accurately. Synthetic scaffolds such as polyethylene glycol (PEG) and polyglycolic acid (PGA) are biodegradable scaffolds that function to mimic the macromolecular structures of the ECM.[10,11] Compared to natural scaffolds, they are mechanically stiffer and therefore suitable for modelling the dense tumour microenvironment. However, they are not without their disadvantages, often having to undergo surface modifications to improve cell attachment, migration and scaffold degradation.[12]

In this article, we describe for the first time the creation and use of a 3D collagen-based multiwell platform for therapeutic validation into colorectal cancer. Tissue-engineered 3D cultures are generated by the RAFT™ (Real Architecture For 3D Tissue) technology, a process based on the removal of water from hyperhydrated collagen hydrogels.[13] This controlled removal of water provides a structurally and physiologically relevant matrix. We chose colorectal as the demonstrator cancer and used the HT29 and HCT116 cancer cell lines to create 3D cultures and monitored growth, morphology and response to targeted treatment. The cell lines were chosen for their *KRAS* mutant status – HCT116 mutant and HT29 wild-type.[14] The expression of the epidermal growth factor receptor (EGFR) was investigated as a biomarker and compared to 2D monolayer expression levels. EGFR was targeted for treatment using cetuximab, the monoclonal antibody raised against the EGFR receptor. These preclinical data demonstrate the use of our 3D cultures as a simple, fast and consistent model for drug testing. We propose this as a suitable in vitro model to help bridge the gap between conventional 2D monolayer studies and complex in vivo animal models.

Materials and methods

Cell maintenance

The HT29 human colorectal adenocarcinoma cell line and the HCT116 human colorectal carcinoma cell lines (both from the European Collection of Cell Cultures, Sigma–Aldrich, Dorset, UK) were used. HT29 and HCT116 cells were routinely cultured in 2D monolayers in Dulbecco's modified Eagle's medium (DMEM) supplemented with 1 g/L glucose, 10% fetal bovine serum (FBS), 100 units/mL penicillin and 100 μg/mL streptomycin (all from Invitrogen, Paisley, UK) at 37°C in standard cell culture conditions (5% CO_2/air and 95% humidity).

Preparation of 3D cultures

The 3D cultures were prepared using the RAFT™ 3D cell culture system in 96-well plates as detailed by the manufacturer's instructions (TAP Biosystems, Royston, UK). In brief, 2.8 mL of Minimal Essential Medium (MEM 10×) was added to 22.4 mL of rat-tail collagen type I. This solution was neutralized by 1.6 mL of the neutralizing solution provided, before 1.2 mL of the cell suspension was added (1.96×10^6 cells/mL). The collagen–MEM–cell solution was mixed gently and aliquoted into the 96-well plate (240 μL per well) and placed on a plate heater (37°C) for 15 min, initiating collagen fibrillogenesis to produce a cell-populated collagen hydrogel. While still on the heater, biocompatible hydrophilic RAFT™ absorbers were placed on the hydrogels and left for 15 min (Figure 1). This process

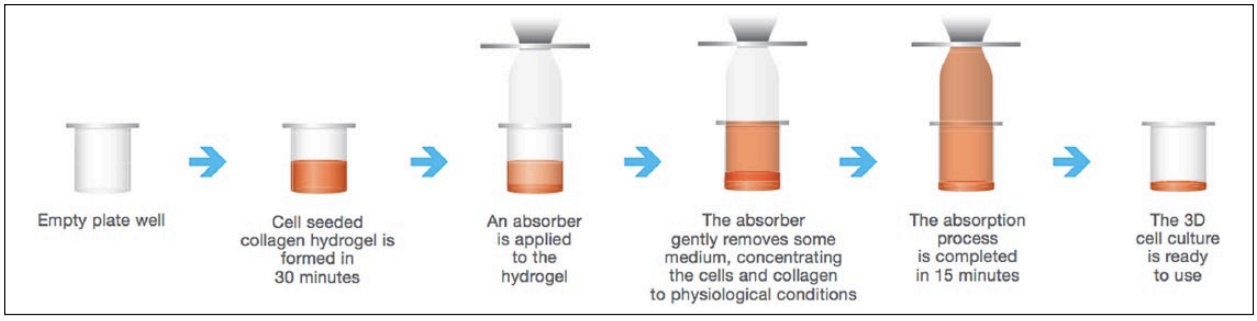

Figure 1. A schematic diagram of how 3D cultures are created.
3D: three-dimensional.

removes some interstitial fluid while preserving cell viability and creates a more physiological matrix (9.59% ± 0.64% collagen as measured by freeze drying to determine the wet and dry weight). Fully supplemented medium was added to each well, and the plates were placed in the incubator, under standard culture conditions.

Cell proliferation and morphology

HT29 and HCT116 cultured in 3D were seeded at a density of 1.96 × 10^6 cells/mL per 3D culture. Preliminary cell density studies indicated that this was the optimum cell density for growth and ease of imaging (data not shown). Metabolic activity was assessed over 14 days using the alamarBlue® assay according to the manufacturers' protocol (Invitrogen). AlamarBlue measures the chemical reduction of resazurin to resorufin by mitochondrial activity and provides an indicator of metabolic activity. DMEM without phenol red (Invitrogen) was used to minimize saturation of the fluorescent dye. In brief, 100 µL of alamarBlue solution (10% solution in fully supplemented DMEM) was added to each well. The samples were incubated for 4 h at 37°C and the solution transferred to a black-bottom 96-well plate to obtain a fluorescent reading at excitation of 530 nm and emission 620 nm. Cell morphology was also monitored in real time by live-cell phase-contrast imaging using a Nikon, Eclipse TE300 microscope.

Immunofluorescence

Cell morphology was confirmed by immunofluorescence. The 3D cultures were fixed in 4% paraformaldehyde for 30 min and washed thoroughly in phosphate-buffered saline (PBS) (three washes for 5 min each). The cultures were permeabilized with 1% Triton X-100 (TX-100) for 15 min and again washed thoroughly with PBS. This was followed by incubation with an anti-tubulin primary antibody solution (Abcam, Cambridge, UK; at 1:200 in a blocking solution of PBS containing 1% bovine serum albumin (BSA) and 0.2% TX-100) overnight at 4°C. The samples were then washed three times in PBS for 5 min each and incubated with a Cy3 conjugated secondary antibody (Jackson ImmunoResearch, West Grove, PA, USA; 1:200), Alexa Fluor 488 conjugated Phalloidin (Invitrogen; 1:40) and 4′,6-diamidino-2-phenylindole (DAPI) diluted in the blocking solution for 2.5 h at room temperature. The cultures were then washed three times with PBS for 5 min each and imaged using an Olympus IX71 Inverted Fluorescent Microscope fitted with a Prior z-focus drive.

Gene expression analysis

Gene expression levels of EGFR were measured with one-step quantitative reverse transcription polymerase chain reaction (qRT-PCR) using a LightCycler® system (Roche, Hertfordshire, UK). Cells were collected from 3D collagen gels by digestion in 100 units/mL collagenase (from *Clostridium histolyticum*) in Tris buffer (Sigma–Aldrich) for 2 h. RNA was extracted from cells in either 2D or 3D after 3 days in culture using the RNeasy Mini Kit (Qiagen, Crawley, UK) according to the manufacturer's instructions. Total RNA was quantified using a nanodrop spectrophotometer measuring at 260/280 nm. All experiments were performed in triplicate.

Drug treatment in 2D and 3D

For 2D monolayer experiments, HT29 cells and HCT116 cells were seeded at a density of 18,000 and 17,000 cells/cm^2, respectively. Cells were allowed to grow overnight before being serum-starved for 24 h in serum-free DMEM. The 3D cultures were seeded at a density of 20,000 cells (1.96 × 10^6 cells/mL) for both cell lines. The 3D cultures were maintained for 6 days before being serum-starved for 24 h prior to treatment. This was carried out to give the cells time to acclimatize to the new environment and for cellular aggregates to form. Cellular aggregates in this context are defined by the migration and adhesion of cancer cells to each other to form cell clusters. Cetuximab (Merck, Darmstadt, Germany) was diluted in serum-free DMEM over a range of concentrations immediately prior

to treatment and incubated for 48 h (2D monolayers) or 72 h (3D cultures). Controls were treated with serum-free DMEM only. Metabolic activity was measured using the alamarBlue assay and was considered an indicator of cell viability.

Evaluation of cell aggregate size

The surface area of 3D cellular aggregates (n = 10) was quantified using measurements based on their circumference using the ImageJ software (version 1.46v). The line tool was used to trace around the cellular aggregates, and the area was calculated using a predetermined scale that was set in ImageJ.

Statistical analysis

Data were presented as means and standard deviations of each group. Statistical analysis was carried out using a one-way analysis of variance (ANOVA) with post hoc Dunnett's test. Significance was accepted at and below 0.05. Results were shown on occasion as percentages for ease of presentation. However, all statistical analyses were carried out on the original data.

Results

Cancer cell proliferation and morphology

To assess the metabolic activity of HT29 and HCT116 cells in 3D culture, the alamarBlue assay was used. Since the assay is non-toxic, multiple readings over a timescale were measured for each well. Increases in metabolic activity, taken as an indicator of cell proliferation, and therefore increases in cell number were determined over 14 days for both cell lines (Figure 2(a)). HT29 cells displayed a steady increase in cell number that appeared to plateau at day 14. Morphologically, the cellular aggregates appeared to grow in size consistently over the 14-day period, in line with the proliferation measurements. On the other hand, although HCT116 cultures exhibited an overall growth pattern over 14 days, there was a significant drop in the proliferation readings at day 7 indicating a quiescent state. However, phase-contrast images of HCT116 cellular aggregates showed no reduction or a slower rate of apparent growth between day 3 and day 7 (Figure 2(b)); therefore, any state of biochemical quiescence did not result in a concomitant morphological change.

The morphology of cellular aggregates was further determined by immunofluorescent analysis of the cytoskeletal proteins tubulin and F-actin. Tubulin is involved in regulating microtubule dynamics during cell division, while the actin filaments are involved in many processes including cell motility and the maintenance of cell junctions.[15] Figure 3 demonstrates the different morphological phenotypes of cellular aggregates of the two cancer cell lines in 3D culture. HT29 cells formed irregularly shaped aggregates of cells with a defined expression of F-actin visible at cell–cell junctions. HCT116 cell aggregates demonstrated a more 'grape-like' phenotype with the cells apparently forming loose clusters with poor cell–cell adhesion in comparison to HT29 cells.[16] Semi-quantitative analysis of the phalloidin stain demonstrated a twofold increase in fluorescent intensity of HT29 cells in comparison to HCT116 cells (data not shown). Expression of tubulin was limited to the outer edges of HT29 aggregates, while HCT116 expression was localized to the spindle fibres of dividing cells throughout the aggregate.

Over-expression of EGFR in 3D compared to 2D monolayer cultures

To determine gene expression levels, total EGFR messenger RNA (mRNA) expression was assessed in HT29 and HCT116 cells cultured in 2D and in 3D by qRT-PCR. EGFR mRNA copy number was standardized to 50,000 copies of G6PDH to ensure that possible differences in cell number did not interfere with expression levels. Analysis of EGFR mRNA levels on cells cultured in 2D showed that HCT116 cells expressed double the EGFR level of the HT29 cells (Figure 4). This difference was illustrated further in 3D cultures cultured for 3 days, as EGFR expression was significantly upregulated in comparison to 2D monolayers. HT29 3D cultures expressed roughly twice the levels of EGFR in comparison to their monolayer counterparts ($p < 0.05$). Similarly, EGFR gene expression in HCT116 3D cultures was also increased approximately threefold in comparison to 2D ($p < 0.01$).

Inhibitory effect of cetuximab on 2D monolayer and 3D cultures

To determine the cytotoxicity of cetuximab, HT29 and HCT116 cells cultured in 2D and in 3D were treated for 48 and 72 h, respectively, and growth inhibition was assessed by the alamarBlue assay. In 2D monolayers, a concentration of 0.34 nM of cetuximab in HT29 cells resulted in a 60% reduction in proliferation in comparison to untreated controls ($p < 0.001$), while HCT116 cells appeared to be non-responsive (Figure 5(a)). Interestingly, at higher concentrations, cetuximab appeared to stimulate the growth of HCT116 cells; however, this was not statistically significant. Cetuximab was less effective in 3D cultures demonstrating a 40% reduction in HT29 proliferation at 3.4 nM; while again, HCT116 cultures were non-responsive (Figure 5(b)) at all concentrations. As a secondary measure of response to drug treatment, the size of cellular aggregates was measured after treatment and compared to untreated controls (Figure 5(c)). A dose-dependent decrease in the size of cellular aggregates broadly correlated with cetuximab treatment efficacy as

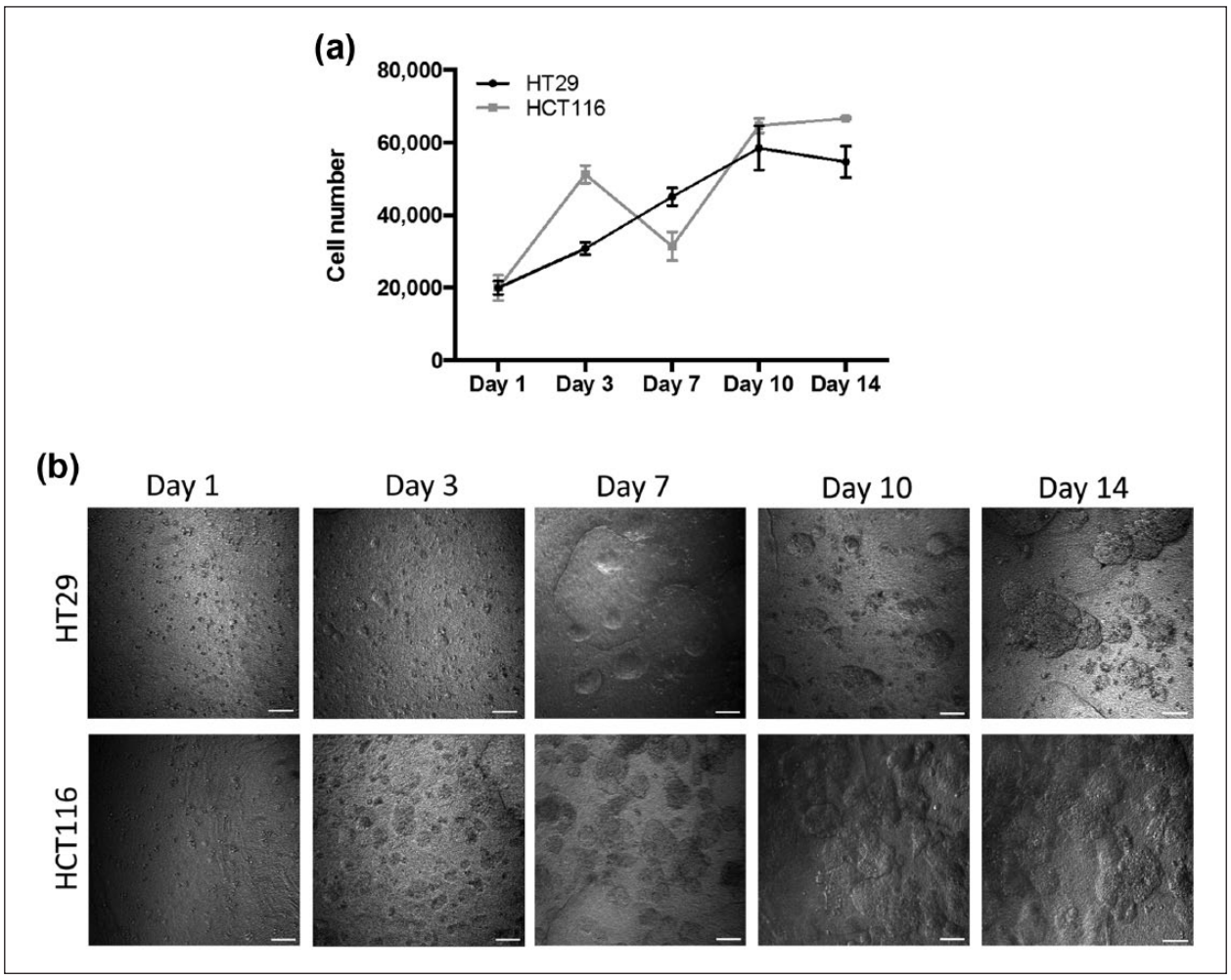

Figure 2. Growth kinetics of HT29 and HCT116 cells in 3D culture. (a) The proliferation profile of HT29 and HCT116 colorectal cancer cells cultured in 3D over a 14-day period measured by the alamarBlue assay and (b) morphological analysis of HT29 and HCT116 3D cultures over a 14-day period. Single cells are seeded and migrate together over time to form cellular aggregates (scale bar – 50 µm).
3D: three-dimensional.

measured by alamarBlue. The size of HT29 cellular aggregates reduced by up to 35% in size ($p < 0.05$) when treated with 3.4 nM cetuximab compared to untreated controls, while the size of HCT116 cellular aggregates remained largely unaffected by treatment at any concentration.

Discussion

Classical 2D monolayer culture provides us with a medium to explore basic mechanistic investigations into cancer cell behaviour in vitro. However, the simplicity of this system does not recapitulate cell–cell and cell–matrix interactions found within the tumour architecture that regulates key tumourigenic pathways.[17] The emergence of 3D in vitro cancer models aims to address these issues by providing a more biomimetic environment for cancer cells. To create our 3D model, we chose collagen type I as our basic matrix component. Collagen type I hydrogels are particularly useful because they are highly biocompatible, malleable by cell behaviour and mimic

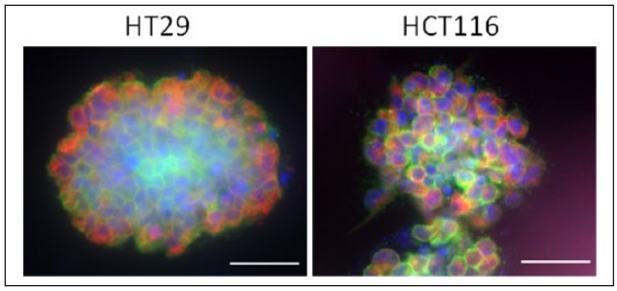

Figure 3. Immunofluorescent analysis of cytoskeletal proteins on colorectal cancer cultures. HT29 and HCT116 cells in 3D cultures were maintained for 14 days, fixed and stained for tubulin (red) and F-actin (green – phalloidin). Nuclei were stained with DAPI (blue) (scale bar – 50 µm).
3D: three-dimensional; DAPI: 4′,6-diamidino-2-phenylindole.

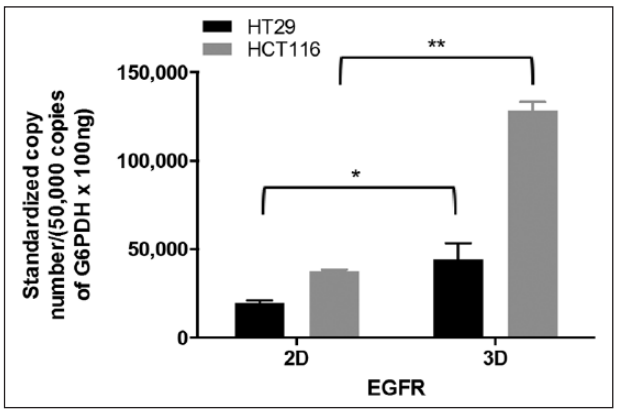

Figure 4. Quantitative RT-PCR analysis of EGFR mRNA levels in colorectal cancer cells. HT29 and HCT116 cells were cultured for 3 days in either 2D or 3D cultures. RNA was extracted and quantified and qPCR was performed using G6PDH as a housekeeping gene. Data are presented as the mean ± SD.
RT-PCR: reverse transcription polymerase chain reaction; EGFR: epidermal growth factor receptor; mRNA: messenger RNA; 2D: two-dimensional; 3D: three-dimensional; qPCR: quantitative polymerase chain reaction; SD: standard deviation.
*$p < 0.05$; **$p < 0.01$.

the basic ECM composition of the natural tumour microenvironment.[18,19] Our previous work reported the development and characterization of a model of colorectal cancer based on plastic compression of collagen hydrogels.[20] The model was created with distinct compartments: a plastically compressed collagen gel populated by cancer cells which was nested in uncompressed collagen populated with fibroblasts and endothelial cells. This manipulation of collagen density for mimicking the dense nature of solid tumours was the first use of this technique for culturing cancer cells in 3D. The aim of this study was to produce and characterize the use of a consistent, scaled down 3D model with physiological levels of collagen as a potential drug-screening platform using two colorectal cancer cell lines and their response to EGFR inhibition.

Prior to drug testing, we characterized the growth characteristics of the two chosen colorectal cancer cell lines in 3D culture. The growth rates of HT29 and HCT116 cultures, as measured by metabolic activity, varied slightly. HT29 cultures exhibited a gradual increase in proliferation and appeared to plateau between days 10 and 14. Morphologically, the cells did not stop increasing in size or number between these time points, implying an inability of alamarBlue to penetrate into the tight cellular aggregates. This problem of transferring 2D end-point assays to 3D cell culture has been highlighted before in detail, and cell morphology was investigated as a secondary assay of growth.[21] Equally, HCT116 cultures proliferated well over the 14-day period; however, at day 7, the proliferation profile appeared to drop transiently (Figure 2(a)). There was no concomitant reduction in the size of cellular aggregates, suggesting that the biochemical changes (reflected in the alamarBlue readings) may describe a short phase of quiescence, which did not affect gross cellular behaviour. HT29 and HCT116 cultures formed morphologically distinct cellular aggregates. Immunofluorescent staining of tubulin and F-actin demonstrated different expression levels for both cytoskeletal proteins. HT29 cultures exhibited a slightly lower, more heterogeneous level of expression of tubulin; however, this may have been an inability of the antibody to penetrate into the cellular aggregates (with HT29 appearing to form more tightly packed aggregates than HCT116). The penetration of antibodies and large molecules has always presented a significant issue in both in situ tumours and in vitro tissue-like substitutes. Xiang et al.[22] treated a spheroid model of mesothelioma with a fluorescently labelled SS1P immunotoxin antibody and monitored penetration over 16 h. The authors reported that the penetration of SS1P was limited to the outer periphery of the spheroids following 4 h of treatment indicating inadequate penetration to the core of the spheroid. The 'grape-like' morphology of HCT116 has been observed before in a panel of breast cancer cell lines cultured in 3D.[16] The authors found that eight out of nine cells that formed a grape-like phenotype were isolated from tumour metastases indicating an acquired ability of these cells to metastasize over the course of their evolution. This supports the reported invasive behaviour of HCT116 cells in comparison to HT29 cultures.[23] Furthermore, the immunofluorescent images in Figure 3 show the loosely bound morphology of HCT116 cells in addition to the cellular protrusions that are typically involved in cell motility.[24] These migratory fronts are classically driven by chemoattractants that stimulate intracellular pathways such as the EGFR pathway. A recent study by Patsialou et al.[25] demonstrated that macrophage-dependent invasion of breast tumour cells in a mouse model was driven by an epidermal growth factor (EGF)/colony-stimulating factor-1 (CSF-1) paracrine loop between host tumour cells and macrophages.[25] The implication of these protrusions in our 3D model may indicate an autocrine signalling pathway involved in the motility of HCT116 cells in physiologically relevant collagen gels.

The expression of EGFR has always been taken as a prerequisite for cetuximab therapy. HT29 and HCT116 (low and high expressing cell lines, respectively) expressions of EGFR were compared and shown to be greatly enhanced in 3D culture in comparison to 2D. The analysis of cetuximab therapy in our 3D model has demonstrated that EGFR expression levels do not necessarily correlate with cetuximab efficacy in vitro. This is consistent with findings in the literature.[26] Wild et al. measured the EGFR expression levels in 11 human carcinoma xenografts and their responses to cetuximab therapy. They revealed a very low correlation profile between EGFR expression in xenografts and response to cetuximab. However, in recent years, it has

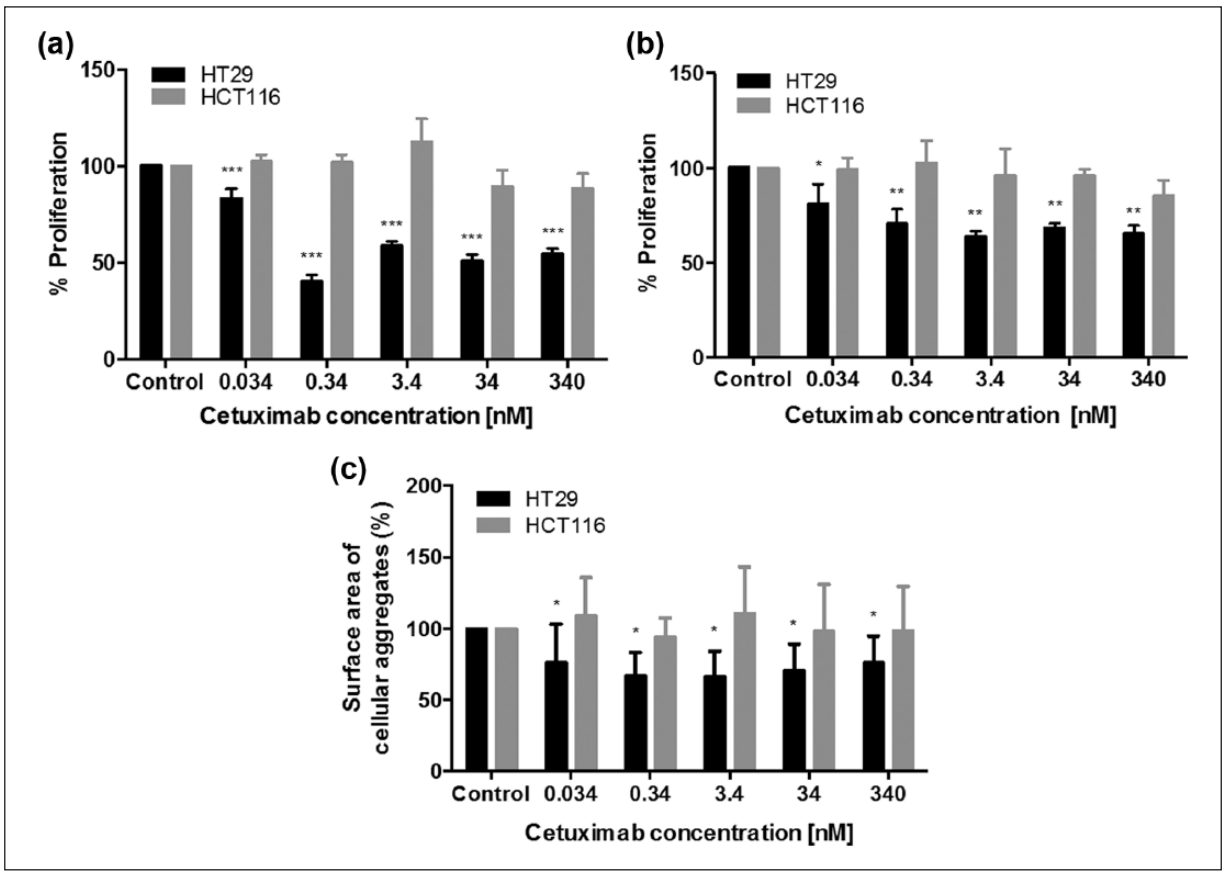

Figure 5. The inhibitory effect of cetuximab on colorectal cancer cells cultured in 2D and 3D. (a) HT29 and HCT116 cells were cultured in 2D and treated for 48 h with cetuximab. (b) HT29 and HCT116 3D cultures were cultured for 7 days and treated for 72 h with increasing concentrations of cetuximab. Cetuximab-treated 3D cultures were then fixed and the (c) surface area of 10 random cellular aggregates was measured using the ImageJ software and calculated as a percentage of the control (n = 4). Data are presented as the mean ± SD.
2D: two-dimensional; 3D: three-dimensional; SD: standard deviation.
*p < 0.05; **p < 0.01; ***p < 0.001.

emerged that *KRAS* mutant status is a much more effective indicator of response to anti-EGFR therapy.[27] The HT29 cell line was chosen for cetuximab treatment in this case for its positive EGFR status and wild-type *KRAS* status and the HCT116 cell line for its *KRAS* mutant status. Although cetuximab was effective on HT29 cells in both 2D and 3D, its inhibitory effect was limited at high concentrations. This could be due to several reasons. First, HT29 cells are a *BRAF* mutant cell line which has been shown previously to lack a sufficient clinical response to cetuximab treatment in a small cohort of patients.[28] Although the precise mechanisms are not fully understood, it is believed that *BRAF* and *KRAS* mutant status should be taken together as indicators of cetuximab efficacy. Second, it has been suggested that immune-dependent mechanisms may contribute to an increase in the efficacy of cetuximab.[29] However, reduced efficacy in vitro may also be attributed to the lack of an immune component in our current 3D model. Hsu et al. demonstrated for the first time in a xenograft model of non-small cell lung cancer that increased cetuximab-mediated toxicity was driven by an immune-dependent mechanism. Complement activation leads to complement-dependent cytotoxicity which releases anaphylatoxins, such as C5a, that increase the recruitment and activation of effector cells. Furthermore, the differences between drug response in HT29 cells in 2D and 3D can also be attributed to drug pharmacokinetics. Similar to the in vivo scenario, our 3D model has displayed a level of 'resistance' or non-responsiveness to chemotherapeutic treatment in comparison to 2D cultures. The formation of cellular structures over time can function to hinder the penetration of large molecules such as cetuximab to the cells in the core, mimicking the in vivo drug barrier in tissues. Hence, improving the penetration of large molecules and drugs will be vital to maximizing the therapeutic potential of these agents. Finally, HCT116 cells either in 2D or 3D were resistant to cetuximab treatment, in line with their *KRAS* mutant status. Interestingly, exposure to cetuximab appeared to promote HCT116 growth by modest, not significant amounts. This increase is not sufficient to lead us to investigate whether

this is an example of paradoxical activation of the mitogen-activated protein kinase/extracellular signal-regulated kinase (MAPK/ERK) pathway. However, it is interesting that no such pattern was observed in 2D HCT116 cultures, highlighting potential differences and usefulness of 3D models.

The work described here is the first to investigate the use of a 3D model of cancer with physiological concentrations of collagen for pharmacological testing. To date, the preclinical drug development process has focused mainly on the use of monolayer cell culture systems while disregarding microenvironmental cues that affect cell behaviour, gene expression and drug diffusion. Although use of spheroid cultures can address drug diffusion, further incorporation of ECM components such as collagen can help direct signals that facilitate intracellular cascade events between intracellular and extracellular spaces that may influence drug distribution. This model can be further improved by incorporating other components of the ECM and cell types that are localized to the tumour stroma such as endothelial cells or fibroblasts.

Conclusion

In this study, we have established the use of our simple and consistent tissue-engineered 3D model as a suitable drug-screening platform. Cells behave similar to the in vivo scenario, forming tumour-like cellular aggregates with visible cell–cell junctions in vitro. Furthermore, we have established that cetuximab efficacy is significantly lower in 3D cultures in comparison to 2D monolayers, independent of EGFR expression levels. This signifies the increasingly important role of matrix density and cellular architecture on drug uptake and distribution. This model could be used to further elucidate the biological mechanisms and physical limitations of drug penetration into in situ tumours.

Declaration of conflicting interests

The authors declare that there is no conflict of interest.

Funding

Umber Cheema is a David Phillips BBSRC fellow and Tarig Magdeldin is funded by the UCL Impact Studentship and TAP Biosystems.

References

1. Ferlay J, Shin HR, Bray F, et al. *GLOBOCAN 2008 v2.0, cancer incidence and mortality worldwide* (IARC Cancer Base No. 10). Lyon: International Agency for Research on Cancer, 2010, http://globocan.iarc.fr
2. Trédan O, Galmarini CM, Patel K, et al. Drug resistance and the solid tumor microenvironment. *J Natl Cancer Inst* 2007; 99(19): 1441–1454.
3. Crompton JG, Clever D, Vizcardo R, et al. Reprogramming antitumor immunity. *Trends Immunol* 2014; 35: 178–185.
4. Pinto A, Merino M, Zamora P, et al. Targeting the endothelin axis in prostate carcinoma. *Tumour Biol* 2012; 33(2): 421–426.
5. Friedrich J, Ebner R and Kunz-Schughart LA. Experimental anti-tumor therapy in 3-D: spheroids–old hat or new challenge? *Int J Radiat Biol* 2007; 83(11–12): 849–871.
6. Kunz-Schughart LA, Kreutz M and Knuechel R. Multicellular spheroids: a three-dimensional in vitro culture system to study tumour biology. *Int J Exp Pathol* 1998; 79(1): 1–23.
7. Holliday DL, Brouilette KT, Markert A, et al. Novel multicellular organotypic models of normal and malignant breast: tools for dissecting the role of the microenvironment in breast cancer progression. *Breast Cancer Res* 2009; 11(1): R3.
8. Suri S and Schmidt CE. Cell-laden hydrogel constructs of hyaluronic acid, collagen, and laminin for neural tissue engineering. *Tissue Eng Part A* 2010; 16(5): 1703–1716.
9. Peppas NA, Hilt JZ, Khademhosseini A, et al. Hydrogels in biology and medicine: from molecular principles to bionanotechnology. *Adv Mater* 2006; 18(11): 1345–1360.
10. Nicodemus GD and Bryant SJ. The role of hydrogel structure and dynamic loading on chondrocyte gene expression and matrix formation. *J Biomech* 2008; 41(7): 1528–1536.
11. Mooney DJ, Mazzoni CL, Breuer C, et al. Stabilized polyglycolic acid fibre-based tubes for tissue engineering. *Biomaterials* 1996; 17(2): 115–124.
12. Place ES, George JH, Williams CK, et al. Synthetic polymer scaffolds for tissue engineering. *Chem Soc Rev* 2009; 38(4): 1139–1151.
13. Brown RA, Wiseman M, Chuo C-B, et al. Ultrarapid engineering of biomimetic materials and tissues: fabrication of nano- and microstructures by plastic compression. *Adv Funct Mater* 2005; 15(11): 1762–1770.
14. Dunn EF, Iida M, Myers RA, et al. Dasatinib sensitizes KRAS mutant colorectal tumors to cetuximab. *Oncogene* 2011; 30(5): 561–574.
15. Fourest-Lieuvin A, Peris L, Gache V, et al. Microtubule regulation in mitosis: tubulin phosphorylation by the cyclin-dependent kinase Cdk1. *Mol Biol Cell* 2006; 17: 1041–1050.
16. Kenny PA, Lee GY, Myers CA, et al. The morphologies of breast cancer cell lines in three-dimensional assays correlate with their profiles of gene expression. *Mol Oncol* 2007; 1(1): 84–96.
17. Yamada KM and Cukierman E. Modeling tissue morphogenesis and cancer in 3D. *Cell* 2007; 130(4): 601–610.
18. Parenteau-Bareil R, Gauvin R and Berthod F. Collagen-based biomaterials for tissue engineering applications. *Materials (Basel)* 2010; 3(3): 1863–1887.
19. Coulson-Thomas VJ, Coulson-Thomas YM, Gesteira TF, et al. Colorectal cancer desmoplastic reaction up-regulates collagen synthesis and restricts cancer cell invasion. *Cell Tissue Res* 2011; 346(2): 223–236.
20. Nyga A, Loizidou M, Emberton M, et al. A novel tissue engineered three-dimensional in vitro colorectal cancer model. *Acta Biomater* 2013; 9(8): 7917–7926.
21. Burdett E and Kasper F. Engineering tumors: a tissue engineering perspective in cancer biology. *Tissue Eng Part B Rev* 2010; 16(3): 351–359.

22. Xiang X, Phung Y, Feng M, et al. The development and characterization of a human mesothelioma in vitro 3D model to investigate immunotoxin therapy. *PLoS One* 2011; 6(1): e14640.
23. Chowdhury S, Ongchin M, Sharratt E, et al. Intra-tumoral heterogeneity in metastatic potential and survival signaling between iso-clonal HCT116 and HCT116b human colon carcinoma cell lines. *PLoS One* 2013; 8(4): e60299.
24. Yamaguchi H and Condeelis J. Regulation of the actin cytoskeleton in cancer cell migration and invasion. *Biochim Biophys Acta* 2007; 1773(5): 642–652.
25. Patsialou A, Wyckoff J and Wang Y. Invasion of human breast cancer cells in vivo requires both paracrine and autocrine loops involving the colony-stimulating factor-1 receptor. *Cancer Res* 2009; 69(24): 9498–9506.
26. Wild R, Fager K, Flefleh C, et al. Cetuximab preclinical antitumor activity (monotherapy and combination based) is not predicted by relative total or activated epidermal growth factor receptor tumor expression levels. *Mol Cancer Ther* 2006; 5(1): 104–113.
27. Lièvre A, Bachet J-B, Le Corre D, et al. KRAS mutation status is predictive of response to cetuximab therapy in colorectal cancer. *Cancer Res* 2006; 66(8): 3992–3995.
28. Laurent-Puig P, Cayre A, Manceau G, et al. Analysis of PTEN, BRAF, and EGFR status in determining benefit from cetuximab therapy in wild-type KRAS metastatic colon cancer. *J Clin Oncol* 2009; 27(35): 5924–5930.
29. Hsu Y-F, Ajona D, Corrales L, et al. Complement activation mediates cetuximab inhibition of non-small cell lung cancer tumor growth in vivo. *Mol Cancer* 2010; 9(1): 139.

A 3D In Vitro Cancer Model as a Platform for Nanoparticle Uptake and Imaging Investigations

Kate P. M. Ricketts, Umber Cheema, Agata Nyga, Andrea Castoldi, Chiara Guazzoni, Tarig Magdeldin, Mark Emberton, Adam P. Gibson, Gary J. Royle, and Marilena Loizidou*

In order to maximize the potential of nanoparticles (NPs) in cancer imaging and therapy, their mechanisms of interaction with host tissue need to be fully understood. NP uptake is known to be dramatically influenced by the tumor microenvironment, and an imaging platform that could replicate in vivo cellular conditions would make big strides in NP uptake studies. Here, a novel NP uptake platform consisting of a tissue-engineered 3D in vitro cancer model (tumoroid), which mimics the microarchitecture of a solid cancer mass and stroma, is presented. As the tumoroid exhibits fundamental characteristics of solid cancer tissue and its cellular and biochemical parameters are controllable, it provides a real alternative to animal models. Furthermore, an X-ray fluorescence imaging system is developed to demonstrate 3D imaging of GNPs and to determine uptake efficiency within the tumoroid. This platform has implications for optimizing the targeted delivery of NPs to cells to benefit cancer diagnostics and therapy.

Dr. K. P. M. Ricketts, Dr. U. Cheema, A. Nyga, T. Magdeldin, Prof. M. Emberton, Dr. M. Loizidou
Division of Surgery and Interventional Science
University College London
9th Floor Royal Free Campus
Rowland Hill Street
NW3 2PF, London, UK
E-mail: k.ricketts@ucl.ac.uk

Dr. K. P. M. Ricketts, Dr. A. P. Gibson, Prof. G. J. Royle
Department of Medical Physics and Bioengineering
University College London
Malet Place Engineering Building
WC1E 6BT, London, UK

Prof. A. Castoldi, Dr. C. Guazzoni
Dipartimento di Elettronica e Informazione
Politecnico di Milano, Edificio 33
via Rimembranze di Lambrate 14
20133 Milano, Italy and Instituto Nazionale di Fisica Nucleare
Sezione di Milano, Italy

DOI: 10.1002/smll.201400194

1. Introduction

Solid cancers (malignant tumors) are composed of cancer foci within a reactive stroma, which is populated by non-cancer cells such as fibroblasts and endothelial cells. The relative constituents vary, resulting in the architectural heterogeneity typical of cancer. This cancer-stromal relationship is easy to observe histopathologically in the tissues. It is less easy to depict when imaging in vivo, either in patients or in animal models, as most imaging modalities (computerized tomography, magnetic resonance and positive emission tomography) do not have the necessary resolution at the micrometer scale. Non-invasive imaging of the tumor microarchitecture and detection of small disseminated disease foci away from the cancer mass boundaries would provide invaluable information that can directly inform treatment choices.

Nanoparticles (NPs) have the potential to act as tumor-specific markers to enhance the resolution of current imaging platforms. Given their relative biologically inert qualities and stability, and unique physicochemical properties, GNPs are good contenders for enhancing imaging sensitivity. They are a reliable contrast medium for use with X-rays due to the

NANO MICRO small

high atomic number (Z).[1–3] This same attribute can be used to enhance the effects of X-ray radiotherapy[4–7] and proton radiotherapy.[8] Moreover, GNPs have a modifiable surface that can be used to increase solubility (to travel through the bloodstream) and enhance cell-specific uptake.[9] Additional coating with polyethylene glycol (PEG), sodium citrate or heparin mitigates any toxicity, prevents initiation of blood coagulation and assists in evading the host immune system.[10] Further functionalization with cancer specific antibodies can enhance targeting and detection as reported using in vivo models with typical concentrations of the order of 0.01 mgNP/mL taken up by tumors—ten-fold greater compared to concentrations in the surrounding tissue.[11–14] In order to maximize their potential in cancer imaging, NP uptake mechanisms and impact of tumor environmental conditions must be understood.

The cancer-stromal relationship influences how cancer cells uptake exogenous agents such as NPs. The majority of the research on biomarker imaging and NP uptake has been carried out in animal models. Although serving as a useful first step, animal work does not always allow the delineation of the relevant mechanisms at the cellular level and has translated poorly to humans. The emergence of 3D in vitro cancer models[15] may provide a more direct and reliable method to test novel forms of biomarker-coupled imaging. In this paper we describe novel application of a 3D in vitro cancer model (tumoroid) capable of incorporating GNPs at typical concentrations achieved in vivo. The platform is based on a cancer model we have developed; previous molecular biology studies of the model have been presented to demonstrate biomimicry in terms of tumor growth and progression properties.[16] Here we present parallel work that demonstrates application of the model as a platform for NP uptake investigations, and as an imaging phantom with ability to inform development of NP imaging technology. It mimics tumor micro-composition, in terms of cell types and spatial positioning to allow specific investigations of NP uptake by cell types found within solid tumors. As a model, it has exciting potential for investigating cancer targeted imaging and therapy and can replace a considerable proportion of work carried out in vivo.

Alongside the cellular model, a technique to measure GNP concentration and distribution is required for uptake investigations. The current gold standard technique for measuring GNP concentration is inductively coupled plasma atomic emission spectroscopy (ICP-AES). However, ICP-AES is not an imaging technique, and digests cells in nitric acid at 110 °C which precludes further analysis.[17] As well as a clinical need for non-destructive measurement methods, there is also a requirement for a GNP imaging technology that is sensitive to sufficiently low concentrations. Current imaging technologies are lacking in this respect, with the lowest measurable concentration of 0.05 mgAu/mL using micro-computed tomography.[12] We have developed a novel non-destructive X-ray fluorescence (XRF) technique that can be used to improve on NP imaging capabilities lacking in current systems. This technique achieves sensitivity more than an order of magnitude greater than other reported techniques down to GNP concentrations of 0.005 mgAu/mL.[18] XRF enables a greater penetration depth than optical techniques (being a higher energy modality) and offers potential for simultaneous imaging of multiple NP compositions. Our approach shows potential in both quantification of and sensitivity to NP concentrations typically found in tumors.[18]

2. Results

2.1. GNP Uptake

The first step of tumoroid production was to initiate GNP uptake within cell lines of each tumoroid component (artificial cancer mass: HT29 colorectal cancer cells, stromal component: 3T3 murine fibroblasts). Uptake of GNPs of diameter 1.9 nm was achieved by both cell lines (incubation time 24 h) as demonstrated by TEM (**Figure 1**), and appeared to be through endocytosis (captured in **Figure 2**). An incubation time of 24 h was found to give optimum GNP uptake in order to maximize GNP imaging signal per cell. It was observed that incubation times greater than 24 h were associated with signs of cell stress and apoptosis (up to 10% cell death at incubation time 48 h). X-ray microanalysis confirmed gold presence within the cells; this involved a TEM technique that bombarded the sample with electrons and detected the emitted X-rays (the energy of emission being characteristic to elemental composition).

2.2. GNP Uptake Measurement using X-Ray Fluorescence

Before complex tumoroids were constructed, uncompressed 3D constructs were manufactured in order to test GNP uptake over a range of incubation doses. The following results enabled relation of GNP incubation dose with uptake concentrations for each cell line; this data was subsequently used to inform controlled engineering of GNP concentration within each tumoroid component (ACM and stroma).

2.2.1. Measured XRF Spectra

To confirm sensitivity to gold the XRF system was used to obtain emission spectra for two 3D uncompressed HT29

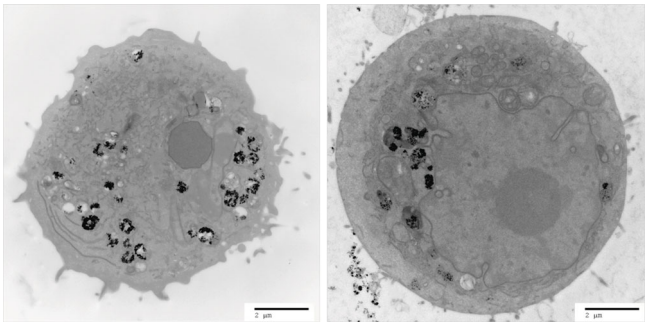

Figure 1. TEM image of a 3T3 fibroblast (left) and an HT29 cancer cell (right) incubated with 1.9 nm GNPs (incubation time 24 h). The cells appear viable; the dark appearance of the cytoplasm indicates presence of ground substances and a healthy state; organelles required for healthy cell functioning are present (such as the nucleus, endoplasmic reticulum and mitochondria). GNPs (black round spheres) appear either dispersed or as aggregates, mostly encapsulated in cytoplasmic vesicles.

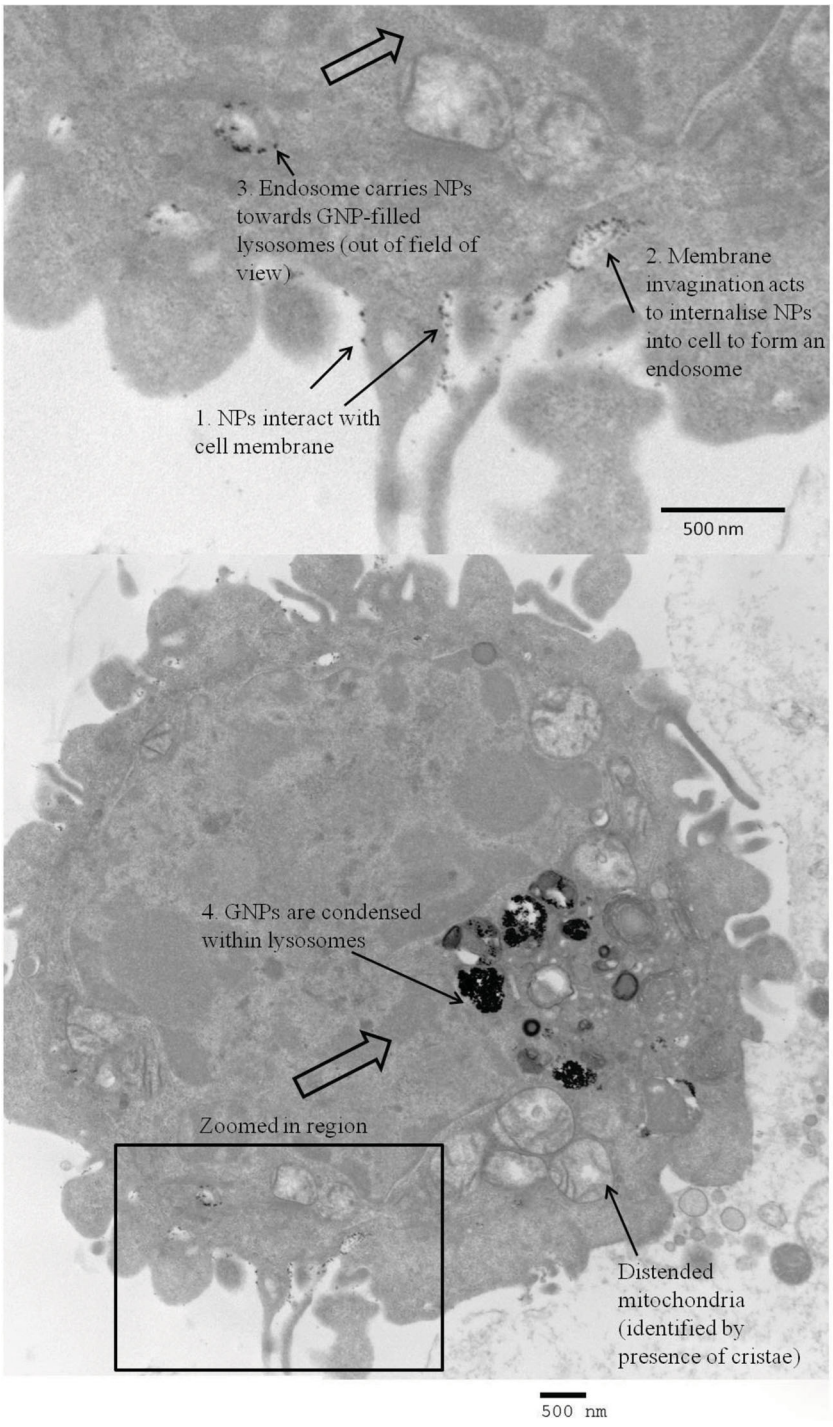

Figure 2. TEM image of the cell membrane surface of an HT29 cancer cell incubated with 1.9 nm GNPs (incubation time 24 h). The image has captured each step of endocytosis: 1) GNP-membrane interaction, 2) membrane invagination to take up GNPs in to the cell, and 3) resulting endosome transports GNPs towards the lysosomes (4).

2.2.2. Calibration Curve

XRF analysis was performed on a range of known GNP concentration solutions in order to determine the actual GNP concentration present in the 3D constructs. The resulting calibration curve ranged from 0.005 mgAu/mL to 0.03 mgAu/mL (Figure 3b).

2.2.3. Gold Concentration per Sample

Figure 3c displays the measured GNP concentration found for the 3T3 and HT29 3D uncompressed constructs. Repeats at the incubation dose 4 mgAu/mL gave the same final GNP concentration within measurement error. The XRF signal from the sample incubated with 4 mgAu/mL was four times greater than that incubated at 1 mgAu/mL (Figure 3c). TEM images qualitatively corroborated the XRF technique's findings that uptake was proportional to initial GNP dose. Attaining a known GNP uptake was shown to be repeatable and reproducible well within the standard errors of measurement. Percentage uptake of initial incubation GNP dose per million cells as measured by a non-destructive XRF technique was found to range between 0.3–0.5% and 0.1–0.3% for the 3T3 and HT29 cell constructs respectively. An order of magnitude estimate of the number of GNPs taken up per cell was undertaken for the highest measured GNP uptake (the 3T3 sample given an incubation dose of 4 mgAu/mL) as follows. The mass of gold per cell was estimated: A GNP concentration of ≈0.015 mgAu/mL was measured for this sample using XRF analysis (Figure 3c); cell number was normalized to 1 million cells per mL. This corresponds to 0.015 ngAu per cell. The mass of one 1.9 nm GNP was estimated: Each NP was assumed to be a solid sphere of gold of calculated volume 4.2 nm^3. The volume was multiplied by the density of gold (19.32 g/cm^3) to give an estimated mass of 7×10^{-11} ng per NP. For this sample we inferred from XRF emissions that $\approx 2 \times 10^8$ GNPs were present per 3T3 cell.

cellular constructs (incubated with 4 mgAu/mL and 0 mgAu/mL (control); **Figure 3**a). Typical measurement times ranged from 40 min for high concentration samples to 400 min for the lowest concentration. The cell samples incubated with gold present a spectrum with the characteristic gold fluorescence lines, compared with the control samples which showed no gold present.

2.3. Tumoroid Production

We implemented a 3D in vitro tissue-engineering technique to create a 3D model that incorporates NP cellular uptake: where the basic premise was to create a dense artificial cancer mass (ACM) comprised of HT29 colorectal cancer cells set within a dense collagen scaffold, surrounded by

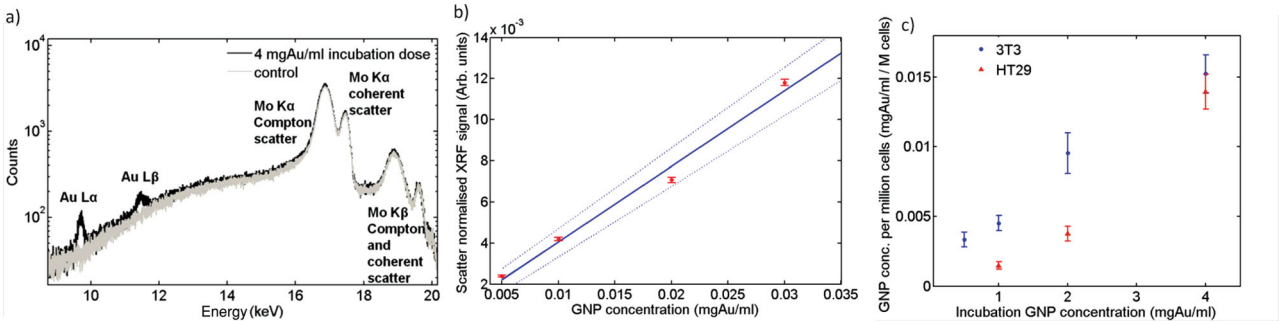

Figure 3. Quantitative XRF measurement of GNP concentration within 3D constructs. a) Measured spectra of 4 mgAu/mL GNP incubation dose uncompressed HT29 cellular construct and 0 mgAu/mL (control) acquired over 40 mins; b) Calibration curve relating XRF signal to GNP concentration. The XRF signal has been normalized to the Compton peak and acquisition time.[20] A weighted linear fit (solid line) and boundary levels (dashed lines) are shown. The boundary levels were fit to fully include 95% of the data points and their error bars; the latter calculated using Poisson statistics. Measurements were made over a range of known GNP concentration solutions; c) GNP concentrations measured in 3T3 and HT29 3D uncompressed cell-populated collagen gel constructs over a range of initial incubation doses. The boundary levels of (b) were used to determine the error on each sample GNP concentration measurement, which was then added in quadrature to the error in the XRF measurement resulting from statistical fluctuations.

uncompressed collagen populated by non-cancer cells, in this case fibroblasts to mimic cancer stroma.[19]

Successful manufacture of a 3D tumoroid (full construct dimensions 8 mm diameter, 18 mm height; ACM diameter 4 mm) was demonstrated with 0.7×10^6 HT29 cells pre-incubated with 5 mgAu/mL for 24 h (compressed ACM) and 6.3×10^6 3T3 fibroblasts pre-incubated with 2 mgAu/mL for 24 h (uncompressed stromal component). The incubation doses were chosen to engineer an ACM GNP concentration of 0.02 mgAu/mL and GNP concentration ratios of 5:1 between the ACM and surrounding stroma to resemble conditions achieved in vivo. The engineered GNP-loaded tumoroid is displayed in **Figure 4**.

2.4. 3D XRF Imaging of Tumoroid

3D XRF imaging was performed of several image slices of the tumoroid, with a partial reconstruction displayed in **Figure 5**. All component details were clearly visible with a delineated ACM emitting at five times more than the surrounding cellular stroma. The image presented in Figure 5 was taken at the Diamond synchrotron source, UK. The log scale amplified recognition of the tumor region (red corresponding to highest gold concentration), the surrounding background (green corresponding to a lower gold concentration) and the plastic container (blue corresponding to absence of gold) in which the tumoroid was set. A control sample with no GNP incubation yielded no gold signal and so the ACM could not be distinguished from the surround.

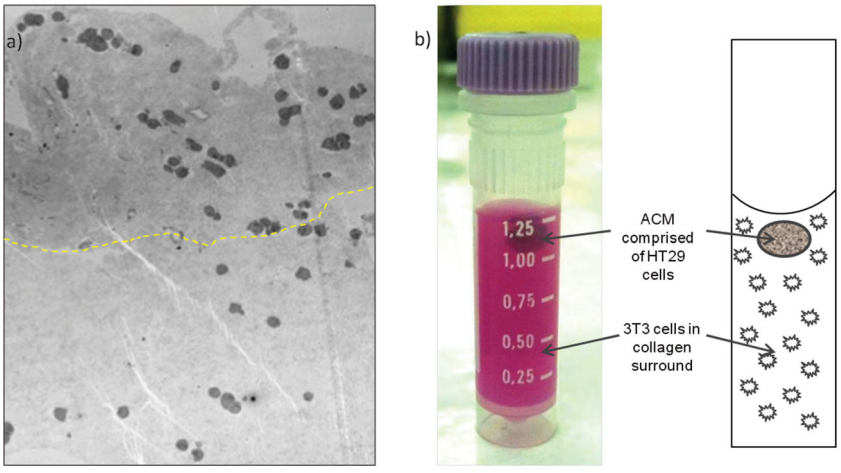

Figure 4. Tumoroid consisting of an artificial cancer mass (ACM):stromal surrounding GNP concentration ratio 5:1, the ACM of approximate concentration 0.02 mgAu/mL. a) Microscopic appearance (TEM) of tumoroid photographed in (b). The boundary between ACM and stroma is evident as a difference in collagen density, the greatest difference in collagen greyscale mapped as a dashed line to estimate the cancer/stromal boundary; collagen is more dense within the ACM (above dashed line) and stromal collagen less dense (below dashed line). GNP containing vesicles are visible within the cells.

3. Discussion

3.1. Summary of Results

We have presented a 3D in vitro cancer model (tumoroid) that was successfully used as a platform to image GNP uptake and distribution at concentrations achieved in human tissue. The tumoroid was engineered to have distinct tumor and stromal compartments mimicking the microarchitecture of solid cancers and developed as a more controllable replacement to small-animal models in order to assess NP delivery to tissue under controlled conditions.

The uptake of 1.9 nm GNPs into the cells used for the uncompressed single cell type 3D constructs and the more complex tumoroids was passive and largely related to the cell surface area, with 3T3 cells being larger than HT29 cells (data not shown). It is likely that this passive uptake was facilitated by protein adsorption on to the GNP surface resulting in a protein corona from serum proteins found in the growth medium, which brings them in prolonged contact with the cell membrane and promotes

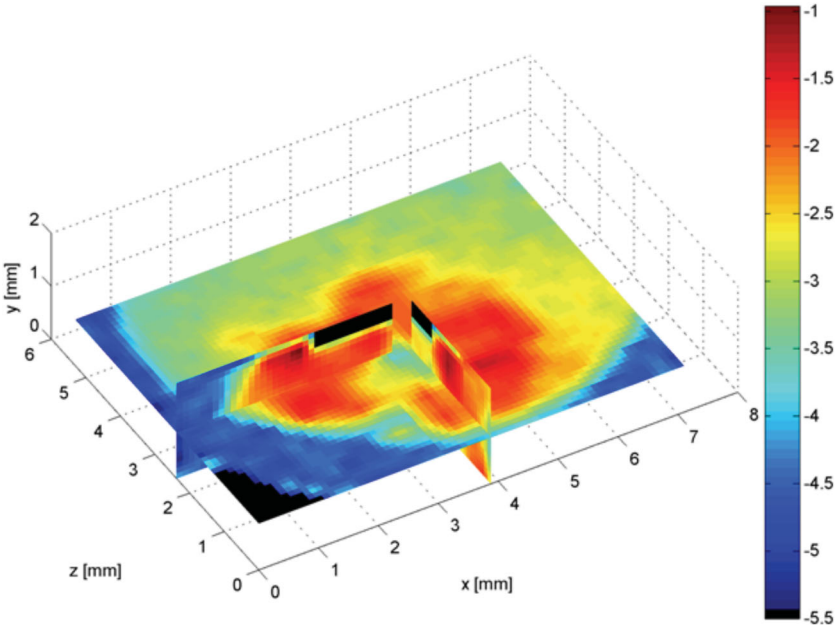

Figure 5. XRF image of three different cross sections of a tumoroid composed of an ACM and surrounding 3T3-embedded collagen gel with a challenging GNP concentration ratio 5:1 between the ACM and surrounding. The blue-to-red colour scale presents gold concentration (red representing the highest gold concentration).

endocytosis.[20] There is huge potential for active targeting through conjugation of the NPs to antibodies that target tumor biomarkers and provide functional information as to the cellular characteristics of the tumor; for example for use in mapping hypoxia.

Dose dependent uptake was demonstrated at incubation times of 24 h. Signs of cytotoxicity were observed for longer incubation time. However, evidence for the cytotoxicity of GNPs is equivocal and requires further study.[11,21,22]

To our knowledge, no other tissue engineered in vitro alternative exists as an imaging platform for research in to imaging biomarkers. Our construct is biomimetic in terms of cell composition and spatial orientation (cancer mass surrounded by collagen matrix and stromal cells). In particular, by using plastic compression, we have increased the density of cell-seeded collagen type I hydrogels to ≈7% (w/v), which aims to approach densities found in vivo (generally accepted as >10%). Cell viability was retained in cells embedded in the scaffold during compression (results not shown); a previous study showed that the standard compression method results in only a 10% reduction in cell viability.[23] Using a tissue engineering approach allows a high degree of modulation and reproducibility which is needed to probe how NP uptake is influenced by controlled introduction of further cell types and incorporation of different matrix components according to designed spatial positioning within specific local matrix densities. To the authors' knowledge, the latter and its importance in cell uptake behavior within tissues is not addressed by any other existing in vitro cancer model.

Furthermore we have presented a novel quantitative imaging module (XRF) that is sensitive to GNP concentration and distribution and can perform non-destructive imaging of bulk 3D samples, the latter imperative for NP uptake studies. To summarise the important novel characteristics of our imager, achieved through it being purpose designed and custom built, we can now meet the needs of NP-imaging that are required by the community and yet to be met in the literature: i) sensitivity to low NP concentrations typically found in vivo (our system is an order of magnitude more sensitive to others reported, with a detection limit of 0.005 mgAu/mL), ii) ability to quantify NP concentration over a 3D matrix: our high energy technique can measure bulk 3D volumes at depth (1–2 cm) currently unachievable by NP imaging techniques, iii) contains 3D positional information of NPs (with spatial resolution better than other technologies due to implementation of polycapillary optics), iv) does not require destruction of the sample unlike gold standard TEM and ICP-AES. In addition the module has potential for multiparametric imaging (simultaneous measurement of multiple NP types). We used both XRF imaging and the reference standard of TEM to observe GNP uptake and distribution in our 3D tumoroids. The use of GNPs as a contrast agent enabled micrometer scale tumor detail to be imaged as can be observed in Figure 5. This result demonstrates clinical potential of GNP-XRF imaging; tumors are not homogeneous, regularly shaped tissues and as such require an imaging technique to fully characterise the cell types and distributions within them to fully inform therapy regimens.

Our XRF technique was used to perform an order of magnitude estimate of the number of GNPs taken up per cell. At the highest given GNP dose of 4 mgAu/mL we estimated that ≈2×10^8 GNPs were present per 3T3 cell. This number of NPs per cell is in keeping with previous reports; one study quantified NP uptake per cell at a rate that was four orders of magnitude lower than our own (3000 per cell) for HeLa cells given an incubation dose four orders of magnitude lower (0.14 μgAu/mL) with 14 nm GNPs.[20] A different NP size, and GNP stabilized with sodium citrate and different cell lines renders the results not directly comparable, but indicates that our estimates of number of GNPs per cell is appropriate and accurate.

3.2. Clinical Implications

We have demonstrated the ability of imaging micrometer scale tumor detail using GNPs as a contrast agent and an XRF technique sensitive to GNP concentration and distribution. This holds great potential in the development of platform technology, which relates to: i) testing active targeting of GNPs to tumors for a range of tumor characteristics under controlled conditions using our model as a platform; NP XRF can be used to determine microstructural and functional signals of a range of biomarkers within the tumoroids,

NANO MICRO small

ii) harvesting and growth of cancer cells from a patient within our tumoroids, we can test the tumor characteristics, signalling and response to therapies on a patient-by-patient basis, delivering potential for true personalized medicine, iii) the development of a higher energy XRF system for potential to work towards GNP XRF in vivo imaging of tumors to guide therapy; the possibility of clinical translation from synchrotron to bench-top source has been demonstrated previously,[18] iv) the ability to map specific tumor characteristics such as hypoxia can be used to inform cancer therapy regimens, for example, radiotherapy dose escalation to hypoxic regions, and v) NP XRF imaging enables capability to detect small clusters of infiltrating cancer cells commonly missed by current imaging modalities.

GNPs were selected in this study to demonstrate the concept of our platform for nanoparticle uptake and imaging studies as they are widely used within the community due to their clinical viability and are heavily reported within the literature; however our uptake and imaging platform is not limited solely to gold and will be used in future studies for uptake investigation of a range of clinically relevant metallic nanoparticles.

3.3. Future Research

This work provides the basic protocol for assessing biofunctionalized NP uptake in 3D in vitro models through the development of tumoroids; we shall extend the current work, which involved NP uptake in monolayer cultures to investigate the cellular uptake of NPs in 3D cultures to represent more realistic in vivo conditions representative of the clinical situation. We also aim to make the model more sophisticated in terms of adding flow components to simulate lymphatic drainage and vasculature leakage.

The tumoroids provide a more controllable replacement to small animal models in order to assess imaging and treatment regimes under modifiable tumor and stromal conditions. For example, investigations of the dose enhancing power of GNPs in radiotherapy will be undertaken using the models. Tumoroid technology has the potential to escalate progress in NP applications in cancer imaging and provision of personalized cancer therapy, providing a platform to inform targeted drug delivery and uptake, and to assess the effectiveness of therapy at the cellular level. We have been developing in parallel a model for investigations in to tumor growth and progression and for therapeutic screening.[16] This model has demonstrated the formation of a hypoxic core at the centre of the ACM and expression of vascular endothelial growth factor (VEGF) by cancer cells at the stromal boundary. The level of hypoxia is controllable and dependent on the cell and extracellular matrix (ECM) density. We aim to implement such tissue engineering strategies to investigate the effectiveness of NPs targeted for hypoxia. We will also use the tumoroids to investigate multi-biomarker imaging where different molecular targeting biomarkers can be tagged to different element NPs each of which will give a specific XRF signal and allow the sophisticated mapping of disease or response to treatment.

4. Conclusions

A 3D in vitro colorectal tumoroid, which mimics the microarchitecture of solid cancers incorporating GNPs at typical concentrations achieved in vivo, was developed in order to provide a nanoparticle uptake platform in order to develop nanoparticle imaging and therapy studies under controlled, variable tumor and stromal conditions.

Production of the tumoroids involved two stages during their development: i) effecting GNP uptake in cells, and ii) embedding the cells in a 3D scaffold. The former stage was successfully achieved with relative ease, thought to be passively facilitated by protein adsorption on to the GNP surface of serum proteins found in the growth media. Future work will look at different culture media to see if different protein corona on the surface of GNPs has an influence on cell uptake and warrants further investigation. Percentage uptake of initial incubation GNP dose per million cells was found to range between 0.3–0.5% and 0.1–0.3% for the 3T3 and HT29 cell constructs respectively. In an in vivo situation tumor cells will take up more GNPs than healthy cells due to leaky tumor vasculature and poor lymphatic drainage at tumor sites. The differential uptake of GNPs between cancer and stromal cells may be improved through functionalisation using specific antibodies, growth factors, and targeting peptides to meet the overall eventual aim of this project in using GNPs as contrast agents to image the distribution of bio-parameters of a tumor. TEM images qualitatively corroborated the XRF technique's findings that uptake was proportional to initial GNP dose, and captured the nanoparticle internalisation process of endocytosis.

3D-XRF imaging successfully measured a challenging GNP concentration ratio of 5:1 between the ACM and stroma of the tumoroid and all component details could clearly be seen. The current model will be extended in the future from GNP incubation in 2D culture towards 3D culture incubation techniques. Here our aim is to mimic the tumor microenvironment through platform technology to determine how cell-cell communication, cell-ECM interactions, ECM and cell density, and outside physical and mechanical forces found under physiological conditions such as shear stress and fluid flow, will affect and influence the uptake of nanoparticles in cells, making use of the non-destructive XRF imaging technique to map the time course of GNP distributions within the model, which will have direct implications in personalized medicine and patient healthcare.

5. Experimental Section

Gold Nanoparticles: GNPs with a 1.9 nm gold core and water-soluble organic shell (Aurovist, Nanoprobes Inc., USA) were suspended in phosphate buffered saline (PBS) and/or cell culture media to form 10 mgAu/mL stock solution. GNP size quantification of these commercially available GNPs was previously measured through TEM analysis and found to have a mean particle diameter of 2.2 ± 0.2 nm (≈70% of particles ranged between 1.5 nm and 2.5 nm).[24]

Cell Culture and GNP Incubation: The human colon adenocarcinoma cell line HT29 (passages [p]:30-42) and the mouse embryonic fibroblast cell line 3T3 (p:28-32) (ECACC, Sigma-Aldrich, Dorset, UK) were cultured routinely under aseptic humidified conditions at 37 °C in 5% CO_2/95% air, in Hepes buffered Dulbecco's Modified Eagle Medium (DMEM plus 1000 mg glucose/L and l-glutamine, Sigma-Aldrich); and supplemented with foetal calf serum (10% FCS, 5129, First Link UK Ltd, Birmingham UK) and penicillin/streptomycin (1% P/S, GIBCO, Invitrogen, Paisley UK). For GNP experiments, cells were grown in 25 cm^2 flasks to 75% confluence and incubated with GNPs (0.5–5 mgAu/mL) in order to i) relate GNP incubation concentration with cellular uptake concentration for each cell line, and ii) to inform engineering of tumoroids to allow control of GNP concentration in each component (ACM and stroma). Incubation was performed under a range of incubation times up to 48 h, under routine conditions, to ascertain an incubation time for optimized GNP uptake within the limits of cell viability. After incubation, a strict protocol was followed to ensure reproducibility and maximum cell harvesting. The cells were washed with PBS (2×3 min), PBS-EDTA (1×2 min) and enzymatically detached using 0.5 mL of 1 mg/mL Trypsin in PBS-EDTA (1 min). Cells were resuspended in 5 mL media, 50 µL were removed for counting (haemocytometer) and the remaining were centrifuged (400*g*, 5 min). Cells were resuspended in a final 0.1 mL or 0.4 mL of media, as appropriate to be used for manufacturing of 3D in vitro constructs.

Manufacture of 3D Uncompressed Cellular Constructs: 3D tissue culture constructs were engineered using HT29 cancer cells and 3T3 fibroblasts. All cells had taken up GNPs. The formation of collagen type 1 lattices involves fibrillogenesis—a thermodynamically driven fibril aggregation following neutralization of native collagen solution. Resultant collagen hydrogels consist mainly (>99%) of water and are therefore of a much lower collagen density than that found in vivo. We mixed collagen type I (rat-tail collagen type I, protein concentration 2.035 mg/mL in 0.6% acetic acid, First Link UK Ltd.) and minimum essential medium (MEM, 10X with Earle's Salts, without l-glutamine, sodium bicarbonate, GIBCO 21430, Invitrogen) and adjusted the pH to 7-7.7 (NaOH: 1 m, 5 m), as judged by indicator colour change. GNP-containing cells (either HT29 or 3T3) were immediately added and the mixture micro-pipetted to ensure even cell dispersion. Collagen:medium:cell volume ratios were 8:1:1. The mixture (1 mL) was transferred to a polypropylene container (inner/outer diameter 8/9 mm, height 45 mm, 1.5 mL volume, Nunc), and the gel allowed to set in a humidified incubator, 5% CO2/95% air at 37 °C for a minimum of 30 min.

Manufacture of Tumoroid: A 3D in vitro tissue-engineering technique was implemented to create a 3D model that enables NP cellular uptake: where the basic premise was to create a dense artificial cancer mass (ACM), surrounded by uncompressed collagen populated by non-cancer cells, in this case fibroblasts to mimic cancer stroma.[19] Briefly, for the ACM, collagen type I and minimum essential medium (MEM) were mixed and the pH adjusted to 7-7.7 (described above). GNP-containing HT29 cells were immediately added to the mixture using a micro-pipette, and poured into a cuboidal mould resting on a nylon mesh which was in turn placed on top of a 165 µm stainless steel mesh and absorbent paper and allowed to set into a gel at room temperature for 30 mins.[19] The gel was compacted using a standard plastic compression protocol modified from[18] (compression under a 73.55 g load, for 5 mins). The gel was turned over and the process repeated to reduce cell concentration gradients resulting from directional fluid flow. This compression results in approximately a 16–fold increase in collagen density compared to uncompressed gels giving a final collagen density for the ACM of 6.7% (w/v).[25] Collagen:MEM:cell volume ratios were 8:1:1 with an overall, pre-compression volume of 4 mL. The dense ACM cuboid gel was divided in to ≈4 mm segments and each segment nested into a 1 mL uncompressed collagen gel populated with GNP-containing 3T3 fibroblasts (prepared as above) before placing in the incubator and allowed to set. Full construct dimensions were 8 mm in diameter, 18 mm in height, and an ACM diameter of 4 mm. The construct was incubated for at least 30 mins before fixation with 10% gluteraldehyde (in PBS) for 24 h at room temperature. The 30 minute incubation times were not sufficient for cell-mediated gel contraction, which habitually starts within a few hours of incubation and can continue to over a week.[26]

Transmission Electron Microscopy (TEM): Fixed 3D culture constructs were dissected using a scalpel blade in to cubes < 2 mm in thickness, washed in PBS and postfixed using 1% osmium tetroxide/1.5% potassium ferricyanide (BDH, Leicester, UK) for 1.5 h; washed in distilled water and dehydrated through a degrading ethanol series (30% to 100%). They were then placed in 50% alcohol/50% Lemix epoxy resin (TAAB Laboratories Equipment Ltd, Reading, UK) mixture overnight (18 h), and the following day infiltrated with 100% Lemix resin for 2 d and finally embedded in fresh Lemix resin and polymerized at 70°C overnight (18 h). Ultrathin sections were cut using a diamond knife (Diatome) and collected on 300HS, 3.05 mm copper grids (Gilder). Sections were stained with saturated uranyl acetate in 50% ethanol (TAAB) for four minutes followed by Reynold's lead citrate for 5 min (BDH). Sections were viewed using a Philips CM120 TEM and photographed with an AMT Digital Camera (Deben UK).

X-Ray Fluorescence Technique: A technique based on inducing X-ray fluorescence (XRF) in GNPs was developed to enable non-destructive quantitative assessment of the GNPs incorporated into the 3D constructs.[18] Here we have extended this 1D measurement technique to enable step and shoot 3D imaging of bulk samples.[27] The system comprised a laminar incident excitation X-ray beam to excite the GNPs to fluoresce, in conjunction with an energy-resolving 10 mm^2 silicon drift detector (SDD) coupled to a slightly focusing polycapillary optic which allowed collection and 3D mapping of fluorescence emissions.[28,29] The magnitude of the XRF signal characteristic to gold was proportional to the concentration of GNPs in the measurement volume. To calibrate, 1 mL GNP solutions were used at 0.005–0.04 mgAu/mL; the concentration range covered the range of GNP concentrations retained by the cell preparations.

GNP Uptake Measurement using X-Ray Fluorescence: Cell cultures (HT29, 3T3) were incubated with GNPs (0.5–4 mgAu/mL) for 24 h and used for manufacture of 1 mL 3D uncompressed cellular constructs (as above). A maximum of 5×10^6 cells/mL were embedded into the collagen gel. XRF measurement using a clinically available bench-top molybdenum X-ray tube was used to determine the internalized GNP uptake efficiency over a range of concentrations.

XRF Imaging of Tumoroid: Measurements were made at the Diamond Light Source, Oxford, UK. The incident energy was

NANO MICRO small

optimized for gold XRF excitation, set to 15 keV (above the edge for gold L-fluorescence of 11.9 keV and 13.7 keV for Lα / Lβ_2 and Lβ_1 fluorescence respectively), a compromise between optimum excitation and minimization of the impact of the Compton shoulder background on the gold fluorescence line. The beam, sample centre and SDD-optic module were aligned. A CCD camera located behind the sample was used to monitor the beam-sample alignment. An ionization chamber was used to monitor beam intensity in order to normalize the data. The sample was then scanned in both the *x*-, *y*-, and *z*-directions to build up a pixellated image. The full energy spectrum was obtained at each point. GNP images were reconstructed off-line by computing the integral counts under the gold *L*α and *L*β fluorescence peaks.

Acknowledgments

U.C. has been supported by a BBSRC fellowship. The authors are indebted to Maria Menikou and Hazel Welch from the Division of Surgery and Interventional Science (DSIS), UCL, UK for their cell culture support, and Jackie Lewin from the Royal Free Hospital, London, UK for her time in producing TEM images. The authors would like to extend thanks to Brian Cousins (DSIS) for his advice and to Bala Ramesh (DSIS), both for their nanoparticle expertise. The authors are grateful to Beppe Montemurri and Pietro Zambon from the Dipartimento di Elettronica e Informazione, Politecnico di Milano, Italy for assisting with acquiring the data during XRF imaging, and for the staff at the Diamond synchrotron for their support during beamline measurement.

[1] Q. Chen, K. Li, S. Wen, H. Liu, C. Peng, H. Cai, M. Shen, G. Zhang, X. Shi, *Biomaterials* **2013**, *34*, 5200–5209.
[2] J. F. Hainfeld, H. M. Smilowitz, M. J. O'Connor, F. A. Dilmanian, D. N. Slatkin, *Nanomedicine* **2013**, *8*, 1601–1609.
[3] Y. Kuang, G. Pratx, M. Bazalova, B. Meng, J. Qian, L. Xing, *IEEE Trans. Med. Imaging* **2013**, *32*, 262–267.
[4] X.-D. Zhang, M.-L. Guo, H.-Y. Wu, Y.-M. Sun, Y.-Q. Ding, X. Feng, L.-A. Zhang, *Int. J. Nanomed.* **2009**, *4*, 165–173.
[5] J. F. Hainfeld, F. A. Dilmanian, Z. Zhong, D. N. Slatkin, J. A. Kalef-Ezra, H. M. Smilowitz, *Phys. Med. Biol.* **2010**, *55*, 3045–3059.
[6] S. Jain, J. A. Coulter, A. R. Hounsell, K. T. Butterworth, S. J. McMahon, W. B. Hyland, M. F. Muir, G. R. Dickson, K. M. Prise, F. J. Currell, J. M. O'Sullivan, D. G. Hirst, *Int. J. Radiat. Oncol. Biol. Phys.* **2011**, *79*, 531–539.
[7] S. J. McMahon, K. M. Prise, F. J. Currell, *Phys. Med. Biol.* **2012**, *57*, 287–290.
[8] J.-K. Kim, S.-J. Seo, K.-H. Kim, T.-J. Kim, M.-H. Chung, K.-R. Kim, T.-K. Yang, *Nanotechnology* **2010**, *21*, 425102.
[9] D. a Giljohann, D. S. Seferos, W. L. Daniel, M. D. Massich, P. C. Patel, C. A. Mirkin, *Angew. Chem. Int. Ed.* **2010**, *49*, 3280–3294.
[10] M. M. Kemp, R. J. Linhardt, *Heparin-based Nanopart.* **2010**, *1*, 77–87.
[11] N. Khlebtsov, L. Dykman, *Chem. Soc. Rev.* **2011**, *40*, 1647–71.
[12] J. F. Hainfeld, M. J. O'Connor, F. A. Dilmanian, D. N. Slatkin, D. J. Adams, H. M. Smilowitz, *Brit. J. Radiol.* **2011**, *84*, 526–533.
[13] K. Sokolov, M. Follen, J. Aaron, I. Pavlova, A. Malpica, R. Lotan, R. Richards-Kortum, *Cancer* **2004**, *63*, 1999–2004.
[14] J. R. Mccarthy, R. Weissleder, *Adv. Drug. Delivery Rev.* **2009**, *60*, 1241–1251.
[15] A. Nyga, U. Cheema, M. Loizidou, *J. Cell Commun. Signal.* **2011**, *5*, 239–248.
[16] A. Nyga, M. Loizidou, M. Emberton, U. Cheema, *Acta Biomater.* **2013**, *9*, 7917–7926.
[17] T. S. Hauck, A. A. Ghazani, W. C. W. Chan, *Small* **2008**, *4*, 153–159.
[18] K. Ricketts, A. Castoldi, C. Guazzoni, C. Ozkan, C. Christodoulou, A. P. Gibson, G. J. Royle, *Phys. Med. Biol.* **2012**, *57*, 5543–5555.
[19] U. Cheema, C.-B. Chuo, P. Sarathchandra, S. N. Nazhat, R. A. Brown, *Adv. Funct. Mater.* **2007**, *17*, 2426–2431.
[20] B. D. Chithrani, A. A. Ghazani, W. C. W. Chan, *Nano Lett.* **2006**, *6*, 662–668.
[21] J. J. Li, D. Hartono, C.-N. Ong, B.-H. Bay, L.-Y. L. Yung, *Biomaterials* **2010**, *31*, 5996–6003.
[22] T. S. Hauck, A. A. Ghazani, W. C. W. Chan, *Small* **2008**, *4*, 153–159.
[23] R. A. Brown, M. Wiseman, C.-B. Chuo, U. Cheema, S. N. Nazhat, *Adv. Funct. Mater.* **2005**, *15*, 1762–1770.
[24] J. Coulter, S. Jain, K. T. Butterworth, L. E. Taggart, G. R. Dickson, S. J. McMahon, W. B. Hyland, M. F. Muir, C. Trainor, A. R. Hounsell, J. M. O'Sullivan, G. Schettino, F. J. Currell, D. G. Hirst, K. M. Prise, *Int. J. Nanomed.* **2012**, 7, 2673–2685
[25] A. Nyga, MSc Thesis, University College London, London, UK **2011**.
[26] M. Eastwood, R. Porter, U. Khan, G. McGrouther, R. Brown, *J. Cell. Physiol.* **1996**, 166, 33–42.
[27] K. Ricketts, A. Castoldi, C. C. Guazzoni, A. P. Gibson, G. J. Royle, *Phys. Med. Biol.* **2013**, *58*, 7841–7855.
[28] E. Gatti, P. Rehak, *Nucl. Instruments Methods Phys. Res.* **1984**, *225*, 608–614.
[29] P. Lechner, C. Fiorini, R. Hartmann, P. Leutenegger, A. Longoni, U. Werber, *Nucl. Instruments Methods Phys. Res., Sect. A* **2001**, *458*, 281–287.

Received: January 22, 2014
Revised: April 22, 2014
Published online: July 2, 2014

